SEMI-ANNUAL STATUS REPORT #1

TO THE NATIONAL AERONAUTICS AND SPACE ADMINISTRATION

CRUSTAL DYNAMICS PROJECT

NASA GRANT NAG 5-814

"The Interpretation of Crustal Dynamics Data in Terms of Plate Motions and Regional Deformation Near Plate Boundaries"

for the period

22 September 1986 - 21 March 1987

Principal Investigator: Prof. Sean C. Solomon
Department of Earth, Atmospheric, and Planetary Sciences
Massachusetts Institute of Technology
Cambridge, MA 02139

15 June 1987

TABLE OF CONTENTS

This is a Semi-annual Status Report on research conducted between 22 September 1986 and 21 March 1987 under NASA Grant NAG 5-814, entitled "The Interpretation of Crustal Dynamics Data in Terms of Plate Motions and Regional Deformation near Plate Boundaries." This grant supports the research of two Investigators (S. C. Solomon and M. N. Toksöz), two Research Staff (E. A. Bergman and R. Reilinger), and two Ph.D. students (J. A. Goff and J. M. Sauber) on behalf of the NASA Geodynamics and Crustal Dynamics Programs.

The focus of the research has been in two broad areas during this initial 6-month period: (1) the nature and dynamics of time-dependent deformation along major seismic zones, including the influence of irregularities in fault geometry on the earthquake cycle, and (2) the processes contributing to the state of stress and rates of strain in plate interior regions. The principal findings of our research to date are described in the accompanying appendices. The first three are abstracts of oral presentations of work supported by this grant during the reporting period. The remaining apendices are preprints of papers submitted for publication during the same period.

APPENDIX 1

Oceanic Transform Fault Jogs: Relation to Seismicity, Maximum Earthquake Size, and Anomalous Mechanisms

SEAN C. SOLOMON and ERIC A. BERGMAN

It is well known that small offsets or curvature in continental strike-slip faults can exert a considerable influence on the loci of rupture initiation and arrrest during major earthquakes. A number of oceanic transform faults have now been surveyed with mapping and imaging techniques (GLORIA, Deep Tow, Sea Beam, Sea MARC) of sufficient resolution to define in detail the trace at the seafloor surface of the transform fault zone (TFZ) or, in some cases, the principal transform displacement zone (PTDZ). We have compared the geometry of the TFZ or PTDZ, as inferred from other investigators, with the location, size, and mechanism of large tranform earthquakes on the Gibbs, Kane, Vema, Romanche, and Clipperton transforms. On the basis of these comparisons, we suggest that the following generalizations serve as working hypotheses: Most TFZ's consist of two or more nearly linear, en echelon fault segments offset by short jogs. These jogs are most commonly dilatational in geometry, in the sense described by *Sibson* [1986]. Rupture during each large transform earthquake appears generally to be confined to a single fault segment. A notable exception to these rules is the eastern half of the Vema transform, where an anti-dilatational jog occurs in the vicinity of the Vema

Mound [*Macdonald et al.*, 1986]. This jog was the site of the largest earthquake known to have occurred on an Atlantic transform (October 1925, M = 7.5), as well as of a more recent large earthquake (25 August 1979, M_S = 6.6) distinguished by a small precursor having a thrust mechanism. The Vema transform has displayed a higher rate of seismic moment release during this century than other Atlantic transforms, when scaled for transform length and the probable depth extent of seismic behavior. The rate is greater than that predicted by simple models of plate slip, which implies an unusually long recurrence time for the largest earthquakes. These characteristics may all be the consequence of the fault zone geometry.

Paper presented at Spring AGU Meeting, Baltimore, Md., 18-21 May 1987.

Abstract published in *Eos Trans. AGU, 68*, 408, 1987.

APPENDIX 2

Strike-slip Fault Geometry and Earthquake Activity In Turkey

A. BARKA and K. KADINSKY-CADE

A comprehensive examination has been made of strike-slip fault geometry in Turkey. The influence of fault geometry on the behavior of large earthquakes has been compared with that for well-studied strike-slip earthquakes in California and Asia. The two main elements comprising the geometric patterns are stepovers and bends. There are many observed combinations of these two elements. Each combination can be associated with a particular fault behavior. The most commonly encountered patterns are (1) the double bend and (2) the restraining bend with adjacent releasing stepover. Fault segmentation is closely related to fault geometry. The geometric patterns are seen to influence the distribution of maximum dislocation and intensity during large earthquakes. Fault geometry is also a critical factor in providing sites for localized strain accumulation, preferred epicenter locations and aftershock sites. The most important fault geometry parameters are: stepover width (less than about 10 km for a through-going rupture) bend angle α (less than about 30° for a through-going rupture), the length L_2 of the restraining fault segment and the angle b between the direction of block motion and the strike of the main fault. In the case of single and double restraining bends

it is observed that log (αL_2) is roughly proportional to earthquake magnitude, and that the epicenter rarely occurs on L_2. Aftershocks and swarms of smaller earthquakes cluster in releasing stepover areas. In a few cases foreshocks can be associated with releasing features located adjacent to or within restraining areas.

Paper presented at Spring AGU Meeting, Baltimore, Md., 18-21 May 1987.

Abstract published in *Eos Trans. AGU, 68*, 362, 1987.

APPENDIX 3

Geodetic Observations of Crustal Deformation: Implications for Paleoseismology

Robert Reilinger
Earth Resources Laboratory
Department of Earth Atmospheric and Planetary Sciences
Massachusetts Institute of Technology
Cambridge, MA 02139

Geodetic measurements in seismically active areas have provided information on the entire range of deformations associated with the "earthquake deformation cycle" including preseismic, coseismic, postseismic and interseismic movements. The most clearly defined of these movements are the coseismic and postseismic deformations which are often large and, in the case of postseismic movements, occur in a known time and place. In contrast, while some possible preseismic movements have been reported, in none of the cases is the evidence unequivocal. Interseismic deformation (i.e., strain accumulation) is difficult to monitor because of the often small amplitude of these movements; however, important information on this phase of the cycle has been obtained through long term monitoring along the San Andreas fault (e.g., Savage, 1983) and near other active plate boundaries.

An important element of the earthquake deformation cycle is the permanent deformation that accumulates as a result of many earthquakes. This deformation takes the form of mountains and basins in dip-slip fault environments, transverse offsets along strike-slip faults (as well as topographic relief in areas of compression or extension) and folding of the rocks adjacent to the faults. For the most part, these permanent deformations occur over too long a time period to be directly investigated with geodetic techniques and require geologic studies. However, in many cases there is a clear relationship between the geodetically measured, short term deformation associated with particular earthquakes and longer term deformation indicated by geologic and topographic structure. These relationships suggest that the geodetic observations

Paper presented at U.S.G.S. Workshop on Paleoseismology, Albuquerque, N.M., 22-25 April 1987.

can provide direct, quantitative information on the mountain building process. Furthermore, as has been emphasised by Thatcher (1984), understanding the contribution of permanent deformation to the earthquake cycle is necessary to effectively use geodetic observations to estimate earthquake repeat times.

In this presentation I attempt to draw some generalizations and identify some unresolved problems concerning the relationship between earthquake deformation and deformation indicated by geologic/topographic structure. The primary information comes from a number of earthquakes with which I am most familiar. These earthquakes occur in a variety of contrasting tectonic settings and include an intraplate thrust event in the Precordillera of western Argentina (Reilinger and Kadinsky-Cade, 1985); a normal fault event in the Basin and Range of the western U.S. for which there is a long history of postseismic deformation measurements (Reilinger, 1986); and a series of predominantly strike-slip earthquakes along the southernmost segment of the San Andreas fault system in the Imperial Valley, California (Reilinger, 1984; Reilinger and Larsen, 1986). Other examples from the literature are used to a limited extent to further examine possible relationships between short and long term deformation (Thatcher, 1980; King and Stein, 1983; Stein and Barrientos, 1985).

This presentation emphasizes the following points:

(1) The earthquake deformation cycle provides a useful framework for investigating geodetically measured surface movements as well as deformation indicated by geologic and topographic structure in seismically active areas.

(2) While there is often a clear relationship between coseismic deformation and long term deformation, the differences between the spatial patterns of deformation over these time scales require large (i.e., similar amplitude to coseismic) postseismic and/or interseismic movements. Comparison of the

coseismic and long term deformation patterns provides direct information on the character of these inter-earthquake movements.

(3) Geodetic observations near two intraplate, dip-slip earthquakes suggest that postseismic viscoelastic relaxation in the asthenosphere is an important mechanism responsible for at least a part of the observed inter-earthquake deformation. These intraplate examples are free from much of the ambiguity associated with postseismic deformation for interplate thrust events in that observations have been made on both sides of the earthquake fault and the wavelengths associated with viscoelastic relaxation and fault creep differ significantly.

(4) The established relationship between earthquake deformation and relatively subtle topographic relief, even in predominantly strike-slip environments, indicates that topography can reflect detailed fault behavior.

While problems concerning errors and non-tectonic influences in geodetic measurements continue, there is no doubt that these data have provided critical information for earthquake research. The progress made in estimating and reducing possible errors in historic measurements, the development and deployment of new and improved geodetic techniques, and ongoing efforts to monitor deformation in areas of past and possible future earthquake activity promise to maintain these measurements as an important element of future investigations into the nature of the earthquake process.

References

King, G., and R.S. Stein, Surface folding, river terrace deformation rate and earthquake repeat time in a reverse faulting environment: The Coalinga, California earthquake of May 1983, in J.H. Bennett and R.W. Sherburne, eds., *Calif. Div. Mines and Geol. Spec. Publ. 66*, Sacramento,

Calif., 261-274, 1983.

Reilinger, R., Coseismic and postseismic vertical movements associated with the 1940 M=7.1 Imperial Valley, California earthquake, *J. Geophys. Res.*, *89*, 4531-4537, 1984.

Reilinger. R., Evidence for postseismic viscoelastic relaxation following the 1959, M=7.5 Hebgen Lake, Montana earthquake, *J. Geophys. Res.*, *91*, 9488-9494, 1986.

Reilinger, R., and K. Kadinsky-Cade, Earthquake deformation cycle in the Andean back-arc, western Argentina, *J. Geophys. Res.*, *90*, 12,701-12,712, 1985.

Reilinger, R., and S. Larsen, Vertical crustal deformation associated with the 1979, M=6.6 Imperial Valley, California earthquake: Implications for fault behavior, *J. Geophys. Res.*, *91*, 14,044-14.056, 1986.

Savage, J.C., Strain accumulation in the western United States, *Ann. Rev. Earth and Planet. Sci.*, *11*, 11-43, 1983.

Stein, R.S., and S.E. Barrientos, Planar high-angle faulting in the Basin and Range: Geodetic analysis of the 1983 Borah Peak, Idaho, earthquake, *J. Geophys. Res.*, *90*, 11,355-11,366, 1985.

Thatcher, W., The earthquake deformation cycle, recurrence, and the time predictable model, *J. Geophys. Res.*, *89*, 5674-5680, 1984.

Thatcher, W., T. Matsuda, T. Kato, and J. Rundle, Lithospheric loading by the 1896 Riku-u earthquake, northern Japan: Implications for plate flexure and asthenospheric rheology, *J. Geophys. Res.*, *85*, 6429-6435, 1980.

APPENDIX 4

SECULAR COOLING OF THE EARTH AS A SOURCE OF INTRAPLATE STRESS

Sean C. Solomon

Department of Earth, Atmospheric, and Planetary Sciences

Massachusetts Institute of Technology

Cambridge, MA 02139 (U.S.A.)

Submitted to Earth and Planetary Science Letters

September 1986

Revised December 1987

Abstract

As a result of secular cooling and contraction of the Earth, an increasingly extensional horizontal stress is imposed on the central portions of the plates. While the rate of increase of this stress is small in most situations, it is enhanced for large plates and during any episodes of accelerated global cooling. This source of stress may have contributed to the rifting and breakup of long-lived supercontinental plates.

1. Introduction

The once-popular idea that changes in planetary volume play an important role in terrestrial orogeny and tectonics [1,2] was generally discarded with the acceptance of plate tectonics. It is likely, however, that the Earth has been steadily cooling over the last 3-4 billion years [3-6], and the global contraction that accompanied that cooling would have led to a secular decrease in the radius of curvature of the plates. In this note we explore the implications of global cooling and contraction for the intraplate stress field.

Because lithospheric stress is episodically relieved at plate boundaries, plate edges may be taken to be free boundaries for the purpose of calculating the response to a slow change in global volume. Under this approximation, the effect of global contraction is to impose an increasingly extensional horizontal stress in the central portions of individual plates [7,8]. The rate of increase of this stress depends on the dimensions and elastic properties of each plate as well as the rate of change of global volume. We consider below the conditions under which secular cooling of the Earth might have contributed significantly to the development of intraplate rifts within the interiors of large continental plates.

2. Formulation

We make use of the analysis of *Turcotte* [7] and *McKinnon* [8] for stress in a thin, circular, elastic plate or cap on an expanding or contracting planetary body. A spherical coordinate system with the pole at the center of the plate (Figure 1) is adopted. The state of stress resulting from a global volume change is derived from the assumptions that plate curvature is changed and that the radial or polar ($\sigma_{\theta\theta}$) horizontal stress is zero at the plate boundary. For a fractional change in radius $\Delta R/R$, the change in membrane stress in a cap of half polar angle θ_o is given by [7,8]

$$\sigma_{\theta\theta} = \frac{4}{3} E \frac{\Delta R}{R} \left[1 - \frac{F(\theta)}{F(\theta_o)}\right]$$
$$\sigma_{\phi\phi} = \frac{4}{3} E \frac{\Delta R}{R} \left[1 + \frac{G(\theta)}{F(\theta_o)}\right] \quad (1)$$

where E is Young's modulus and the functions F and G are given by

$$F(\theta) = (2 + \csc^2 \frac{\theta}{2}) K(\sin^2 \frac{\theta}{2}) - 4 (1 + \csc^2\theta) E (\sin^2 \frac{\theta}{2})$$
$$G(\theta) = (\csc^2 \frac{\theta}{2} - 3) K(\sin^2 \frac{\theta}{2}) + 2 (3 - 2 \csc^2\theta) E (\sin^2 \frac{\theta}{2}) \quad (2)$$

where $K(m)$ and $E(m)$ are complete elliptic integrals of the first and second kind, respectively. Stress in (1) is positive in extension.

The principal stresses resulting from global contraction ($\Delta R < 0$) are shown as functions of polar angle in Figure 2. The quantities $\sigma_{\theta\theta}$ and $\sigma_{\phi\phi}$ are equal and extensional (positive) at the center of the plate ($\theta = 0$). Both stress components decrease smoothly and monotonically with θ; the radial stress $\sigma_{\theta\theta}$ equals zero at $\theta = 0$, while the azimuthal stress $\sigma_{\phi\phi}$ passes through zero at $\theta \approx 0.5\,\theta_0$ and is compressional in the outer portions of the plate. The magnitude of the maximum extensional stress at the plate center may be approximated by [8]

$$\sigma_0 = - \frac{E}{4} \frac{\Delta R}{R} (1 - \cos\theta_0) \quad (3)$$

to an accuracy of a few percent for $\theta_0 \leq 70^\circ$ (Figure 3).

For an Earth contracting at a rate $\dot{R}$, the time rate of accumulation of extensional stress at the center of the plate, from (3), is approximately

$$\dot{\sigma} = - \frac{E}{4R} \dot{R} (1 - \cos\theta_0) \quad (4)$$

and is thus linearly proportional to the solid angle subtended by the plate, $2\pi\ (1 - \cos\theta_o)$, and to the rate of global contraction. It is important to note that this formulation for intraplate stress is a purely elastic solution and neglects the effects of brittle or ductile processes which act to reduce stress. In this sense, the quantity $\dot{\sigma}$ given by equation (4) should be regarded as a maximum rate of change of stress for a given $\dot{R}$ and plate area. It is useful to consider the equivalent rate of extensional strain

$$\dot{\varepsilon} = - \frac{(1-\nu)}{4R} \dot{R} (1 - \cos\theta_o) \qquad (5)$$

where ν is Poisson's ratio, as this quantity may be approximately preserved even under inelastic intraplate deformation. The Earth's plates, of course, are subject to many other sources of stress and strain, but (4) and (5) are in a form where we may make approximate comparisons with the predictions of competing processes. We consider the relative importance of several other long-term secular sources of intraplate stress and strain in a later section.

3. Rate of global contraction

The rate of global contraction $\dot{R}$ may be estimated from a thermal history model for the Earth and an estimate of the radial dependence of the coefficient of volumetric thermal expansion, α :

$$\dot{R} = \frac{1}{R^2} \int_0^R r^2\, \alpha(r)\, \dot{T}(r)\, dr \qquad (6)$$

This expression neglects the contributions of radial migration of phase boundaries involving changes in specific volume, which we consider separately below. It is common in global thermal history models to parameterize the heat transport and thermal state of convecting regions by a small number of quantities including a characteristic temperature [e.g., 3-5,9,10]. To the extent that a single characteristic or

potential temperature T can represent global cooling and that variations in α with depth may be neglected, equation (6) simplifies to

$$\dot{R} \approx \frac{R\alpha}{3} \dot{T} \qquad (7)$$

The latter assumption may be questioned considering the expected dependence of α on temperature, pressure, and phase, but recent measurements of the zero-pressure thermal expansion coefficient of $(Mg_{0.9},Fe_{0.1})\ SiO_3$ perovskite [11] yield values comparable to those of the principal upper mantle phases [12,13].

The rate of secular cooling $\dot{T}$ in (7) may be estimated in two ways. *Green* [14] and *Sleep* [3] have argued that the differences between the eruption temperatures of Archaean komatiites and modern tholeiites give a direct measure of $\dot{T}$ of about -100 K/b.y., with an uncertainty of perhaps 30%. Alternatively, $\dot{T}$ may be estimated from the difference between the global heat flux q in a thermal history model and the flux q_s that would be produced under steady-state conditions (if heat loss equaled heat production)

$$q - q_s \cong \frac{4}{3} \pi R^3 \rho C_p \dot{T} \qquad (8)$$

where ρ and C_p are representative values of density and specific heat, respectively. Thermal history models for the Earth differ considerably in how mantle convective heat transport is parameterized, principally in whether whole-mantle or layered convection systems are assumed [15] and in how strongly heat flux and characteristic temperature are coupled [16]. These differences yield variations in q/q_s, sometimes called the "Urey ratio" [17], ranging from about 1.2 to 2.7 [18], with values toward the upper end of this range yielding estimates for $\dot{T}$ most consistent with those derived from the eruption temperatures of mantle-derived magmas [3,14] and independent estimates of the Urey ratio from geochemical arguments [17,19]. With $\dot{T} = -100$ K/b.y. and $\alpha = 3 \times 10^{-5}\ K^{-1}$, equation (7) gives $\dot{R}/R = -10^{-3}$/b.y. or $\dot{R} = -6$ km/b.y. (Table 1).

4. Effects of phase boundary migrations

As the mantle cools, temperature dependent phase boundaries will move radially outward or inward, depending on whether the Clapeyron slope dP/dT of the reaction is respectively positive or negative. The resulting change in the volume of mantle undergoing phase transformation contributes to a change in R. We show in Table 1 estimates for contributions to $\dot{R}$ from the migration of the $(Mg,Fe)_2SiO_4$ olivine–ß phase boundary, the $(Mg,Fe)_2SiO_4$ ß–γ (spinel) phase boundary, and the reaction γ–$(Mg,Fe)_2SiO_4 \rightarrow (Mg,Fe)SiO_3$ (perovskite) + (Mg,Fe)O induced by global cooling at a rate $\dot{T} = -100$ K/b.y. The phase boundaries are assumed to occur at 370, 400, and 670 km, respectively, and for the purposes of this estimate the upper mantle is assumed to consist only of $(Mg,Fe)_2SiO_4$ with the molar ratio Fe/(Fe+Mg) = 0.12 [20]. As a result of this last assumption, the contribution of each phase change to global contraction will be overestimated because of the presence of uninvolved minerals at each transition depth, but this should be approximately offset by the contributions of other phase transitions not considered here. The specific volumes of the respective phases are from *Lees et al.* [20], and the Clapeyron slopes are taken to be 3.5 MPa/K [21], 5.5 MPa/K [21] and –2.0 MPa/K [22], respectively.

The effect on global contraction of each of the migrating phase transformations considered is an order of magnitude smaller than for whole-Earth cooling (Table 1). Further, the contributions of these phase transformations partially cancel each other because of the mix of signs of the Clapeyron slopes.

Also shown in Table 1 is an estimate of the contribution to $\dot{R}$ from inner core solidification, under the assumption that solid Fe at inner core pressures is in the ε phase [23] and that the rate of increase in the volume of the inner core has been constant for 4 b.y. The specific volume of ε-Fe and the change in specific volume at melting are taken to be 4.2 [24] and 0.6 cm^3/mole [23], respectively. The effect on $\dot{R}$ of

steady growth of the inner core (Table 1) is much smaller than the other contributions treated and is not considered further.

5. Rates of intraplate stress and strain

The overall rate of global contraction indicated in Table 1 is about –7 km/b.y. As a result of such steady contraction, equations (4) and (5) with E and ν assigned typical crustal values (100 GPa and 0.25, respectively) indicate that a circular plate of radius R would experience a secular increase in the rate of extensional membrane stress and strain in the central plate interior of 12 MPa/b.y. and 3×10^{-21} s^{-1}, respectively. Neither one of these quantities is sufficiently large to exert an influence in intraplate regions undergoing deformation in response to other processes. The typical magnitude of intraplate stresses arising from plate tectonic forces is likely in the range 10-100 MPa [25], and rates of strain in tectonically active plate interior regions can exceed 10^{-16} s^{-1} [26,27]. It is nonetheless of interest to consider whether there are conditions under which global cooling might have been an important source of stress in stable plate interiors. As a first step in that discussion, we first consider other long-term sources of steady change in plate membrane stress.

One additional source of membrane stress is the change in the ellipticity e of the Earth's figure accompanying tidal despinning. From first-order hydrostatic theory, $\dot{e}/e = 2\dot{\Omega}/\Omega$, where Ω is the spin rate. From the paleontological record of growth in corals and bivalves, *Lambeck* [28] gives $\dot{\Omega} = -5 \times 10^{-22}$ s^{-2} since the mid-Paleozoic, which yields $\dot{e} = -1.4 \times 10^{-3}$ /b.y. This rate of change in ellipciticity may be converted to a change in the mean radius of curvature r at colatitude θ by use of the expression [7]

$$\dot{r}(\theta) = R\,\dot{e}\,(2\cos^2\theta - 1) \qquad (9)$$

which yields $\dot{r} = -9$ km/b.y. at the poles and +9 km/b.y. at the equator. The rate of change of radius of curvature of a large plate due to the change in spin rate is thus

comparable to that due to global cooling. The two effects will add constructively at high latitudes and tend to cancel each other near the equator.

Membrane stress also accumulates as plates change latitude on an ellipsoidal Earth [7]. For a circular plate with radius R moving from the pole to the equator at 10 mm/yr latitudinal velocity, the mean radius of curvature at the plate center changes at the rate $\dot{r} = -43$ km/b.y. and the central plate interior is subjected to increasing extensional stress at the rate 70 MPa/b.y. [7]. This effect can thus be locally larger than the stress due to global contraction or despinning, but only if the poleward component of plate motions are rapid or are sustained for a long interval of geological time.

6. Assessment of global cooling as a source of intraplate stress

The average rates of increase of intraplate stress and strain due to secular cooling of the Earth are too low to be of importance for most plates. Oceanic plates are too young to have accumulated much stress by this process, and all of the present plates have appreciably altered their geometry on time scales shorter than 10^9 yr.

Several effects, however, might increase the importance of global cooling and contraction for the intraplate stress field in some situations. The stress level increases with the area of a plate and with its longevity, and thus would be maximum for a long-lived "supercontinent" plate. The rate of stress build-up would also be increased during any periods of accelerated global cooling; such periods have been suggested on the basis of intervals of rapid seafloor spreading [29] and time-dependent convection calculations [30,31].

Extended time intervals during which a large fraction of continental lithosphere was assembled into a single supercontinent have been postulated at several periods in Earth history. During the Phanerozoic, the Pangaea supercontinent persisted for at least 50-70 m.y., and Gondawanaland was intact for approximately 450 m.y. [32]. Evidence for the breakup of of a supercontinent about 600 m.y. ago has been

documented from tectonic subsidence curves by *Bond et al.* [33]. Episodes of assembly, stasis, breakup, and dispersal of supercontinents extending back to the late Archean have been recognized by *Worsley et al.* [34]; they suggest that these episodes are cyclic with a period of about 0.5 b.y.

The supercontinent breakup phase is marked by pervasive intracontinental rifting and volcanism. The formation of the midcontinent rift system of North America [35], for instance, may have been the last in a series of extensional episodes marked by widespread emplacement of igneous terranes in the midcontinental region [36]. *Burke and Wilson* [37] have described the relationship between rifting events and mantle hot spots beneath continental lithosphere, and *Anderson* [38] has postulated that a supercontinent can insulate the upper mantle and lead to the formation of the hot spots.

As described above, a long-lived supercontinental plate would be subjected, by the secular cooling of the Earth, to extensional horizontal stresses in the plate interior even in the absence of mantle hot spots. Because of the relative magnitude and sign of the secular changes in stress contributed by despininning and latitudinal plate motion, this effect would be enhanced for a high latitude plate with a poleward component of absolute plate motion. While global cooling alone did not produce an intraplate stress field sufficient to initiate widespread extensional faulting, it may nonetheless have been an important contributor to the rifting and breakup of the supercontinents.

Acknowledgements

I thank Paul Hoffman and Norman Sleep for helpful discussions, Linda Meinke for assistance with the figures, and Jan Nattier-Barbaro and Mark Carlson for help with manuscript preparation. This research was supported by the National Aeronautics and Space Administration under grants NSG-7297 and NAG5-814 and contract NAS5-27339.

REFERENCES

1 H. Jeffreys, The Earth, 2nd ed., pp. 278-294, Cambridge University Press, Cambridge, 1929.

2 J.T. Wilson, The development and structure of the crust, in: The Earth as a Planet, The Solar System, vol. 2, G.P. Kuiper, ed., pp. 138-214, Univ. of Chicago Press, Chicago, Ill., 1954.

3 N.H. Sleep, Thermal history and degassing of the Earth: Some simple calculations, J. Geol. 87, 671-686, 1979.

4 D.L. Turcotte, On the thermal evolution of the Earth, Earth Planet. Sci. Lett. 48, 53-58, 1980.

5 F.D. Stacey, The cooling Earth: a reappraisal, Phys. Earth Planet. Inter. 22, 89-96, 1980.

6 F.M. Richter, Models for the Archean thermal regime, Earth Planet. Sci. Lett. 73, 350-360, 1985.

7 D.L. Turcotte, Membrane tectonics, Geophys. J. Roy. Astron. Soc. 36, 33-42, 1974.

8 W.B. McKinnon, Tectonic deformation of Galileo Regio and limits to the planetary expansion of Ganymede, Proc. Lunar Planet. Sci. 12B, 1585-1597, 1981.

9 D.P. McKenzie and N.O. Weiss, Speculations on the thermal and tectonic history of the Earth, Geophys. J. Roy. Astron. Soc. 42, 131-174, 1975.

10 H.N. Sharpe and W.R. Peltier, A thermal history model for the Earth with parameterized convection, Geophys. J. Roy. Astron, Soc. 59, 171-203, 1979.

11 E. Knittle, R. Jeanloz and G.L. Smith, Thermal expansion of silicate perovskite and stratification of the Earth's mantle, Nature 319, 214-216, 1986.

12 B.J. Skinner, Thermal expansion of ten minerals, U.S. Geol. Surv. Prof. Paper 450D, 109-112, 1962.

13 I. Suzuki, E. Ohtani and M. Kumazawa, Thermal expansion of γ–Mg_2SiO_4, J. Phys. Earth 27, 53-62, 1979.

14 D.H. Green, Genesis of Archean periodotitic magmas and constraints on Archean geothermal gradients and tectonics, Geology 3, 15-18, 1975.

15 D. McKenzie and F.M. Richter, Parameterized thermal convection in a layered region and the thermal history of the Earth, J. Geophys. Res. 86, 11667-11680, 1981.

16 U.R. Christensen, Thermal evolution models for the Earth, J. Geophys. Res. 90, 2995-3007, 1985.

17 A. Zindler and S. Hart, Chemical geodynamics, Ann. Rev. Earth Planet. Sci. 14, 493-571, 1986.

18 N.H. Sleep and R.T. Langan, Thermal evolution of the Earth: some recent developments, Adv. Geophys. 23, 1-23, 1981.

19 R.K. O'Nions, S.R. Carter, N.M. Evensen and P.J. Hamilton, Upper mantle geochemistry, in: The Oceanic Lithosphere, The Sea, vol. 7, C. Emiliani, ed., pp. 49-72, Wiley Interscience, New York, N.Y., 1981.

20 A.C. Lees, M.S.T. Bukowinski and R. Jeanloz, Reflection properties of phase transition and compositional change models of the 670-km discontinuity, J. Geophys. Res. 88, 8145-8159, 1983.

21 K. Suito, Phase relations of pure Mg_2SiO_4 up to 200 kilobars, in: High Pressure Research, M.H. Manghnani and S. Akimoto, eds., pp. 255-266, Academic Press, New York, N.Y., 1977.

22 E. Ito and H. Yamada, Stability relations of silicate spinels, ilmenites, and perovskite, in: High-Pressure Research in Geophysics, S. Akimoto and M.H. Manghnani, eds., pp. 405-419, Center for Academic Publication Japan/D. Reidel, Tokyo/Dordrecht, 1982.

23 L. Liu, On the (γ,ε,l) triple point of iron and the Earth's core, Geophys. J. Roy. Astron. Soc. 43, 697-705, 1975.

24 D.J. Andrews, Equation of state of the alpha and epsilon phases of iron, J. Phys. Chem. Solids 34, 825-840, 1973.

25 S.C. Solomon, R.M. Richardson and E. A. Bergman, Tectonic stress: models and magnitudes, J. Geophys. Res. 85, 6086-6092, 1980.

26 G.P. Eaton, The Basin and Range province: origin and tectonic significance, Ann. Rev. Earth Planet. Sci. 10, 409-440, 1982.

27 J.K. Weissel, R.N. Anderson and C.A. Geller, Deformation of the Indo-Australian plate, Nature 287, 284-291, 1980.

28 K. Lambeck, The Earth's Variable Rotation: Geophysical Causes and Consequences, pp. 360-400, Cambridge University Press, Cambridge, 1980.

29 D.L. Turcotte and K. Burke, Global sea-level changes and the thermal structure of the Earth, Earth Planet. Sci. Lett. 41, 341-346, 1978.

30 G.T. Jarvis, Time-dependent convection in the Earth's mantle, Phys. Earth Planet. Inter. 36, 305-327, 1984.

31 A.P. Boss and I.S. Sacks, Time-dependent models of single- and double-layer mantle convection, Nature 308, 533-535, 1984.

32 B.F. Windley, The Evolving Continents, 385 pp., John Wiley, New York, N.Y., 1977.

33 G.C. Bond, P.A. Nickerson, and M.A. Kominz, Breakup of a supercontinent between 625 Ma and 555 Ma: new evidence and implications for continental histories, Earth Planet. Sci. Lett. 70, 325-345, 1984.

34 T.R. Worsley, R.D. Nance and J.B. Moody, Tectonic cycles and the history of the Earth's biogeochemical and paleoceanographic record, Paleoceanography 1, 233-263, 1986.

35 W.R. Van Schmus and W.J. Hinze, The midcontinent rift system, Ann. Rev. Earth Planet. Sci. 13, 345-383, 1985.

36 M.E. Bickford, W.R. Van Schmus and I. Zeitz, Proterozoic history of the midcontinent region of North America, Geology 14, 492-496, 1986.

37 K.C. Burke and J.T. Wison, Hot spots on the earth's surface, Sci. Am. 235 (2), 46-57, 1976.

38 D.L. Anderson, Hotspots, polar wander, Mesozoic convection, and the geoid, Nature 297, 391-393, 1982.

Table 1. Contributions to global contraction

Whole-Earth cooling	
$\dot{T} = -100$ K/b.y.	$\dot{R} \approx -6$ km/b.y.
Mantle phase changes	
$\alpha \rightarrow \beta$ - $(Mg, Fe)_2SiO_4$	$\dot{R} \approx -0.6$ km/b.y.
$\beta \rightarrow \gamma$ - $(Mg, Fe)_2SiO_4$	$\dot{R} \approx -0.3$ km/b.y.
$\gamma \rightarrow$ pv + mw	$\dot{R} \approx 0.4$ km/b.y.
Inner core solidification	$\dot{R} \approx -0.05$ km/b.y.

FIGURE CAPTIONS

Figure 1. Geometry of the problem, after *McKinnon* [8]. A circular plate of half polar angle θ_0 sits on a spherical Earth. Global contraction leads to extensional stress in the center of the plate and azimuthal compression near the plate edges.

Figure 2. Normalized principal membrane stresses in a circular plate of half polar angle $\theta_0 = 50^\circ$ on a contracting Earth.

Figure 3. Maximum extensional stress in a circular plate of half polar angle θ_0 after a decrease ΔR in global radius R. The stress is normalized by σ_0.

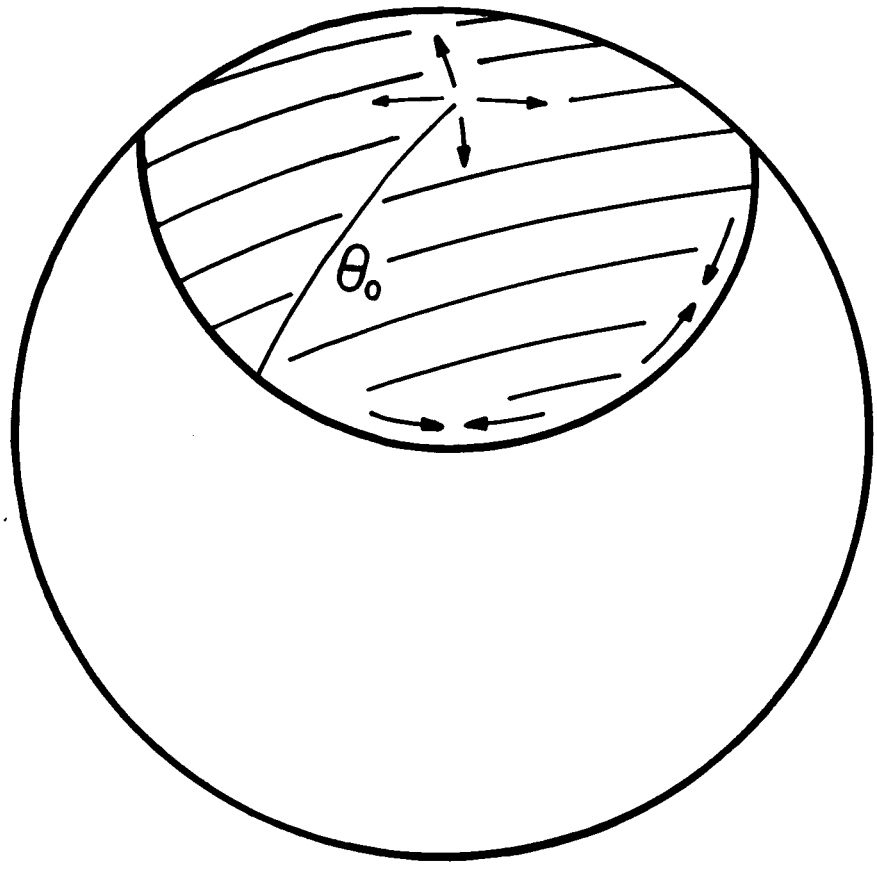

Figure 1

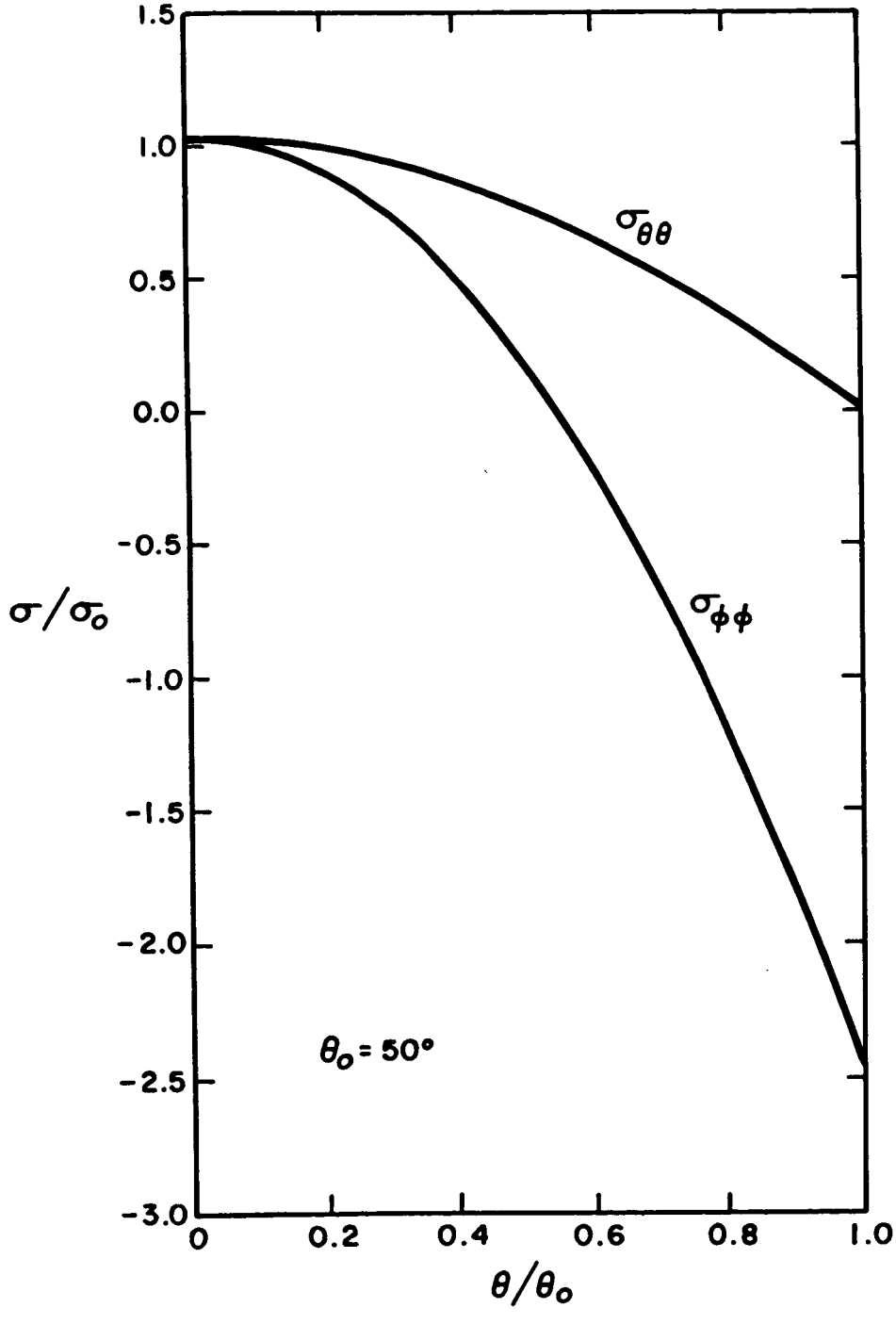

Figure 2

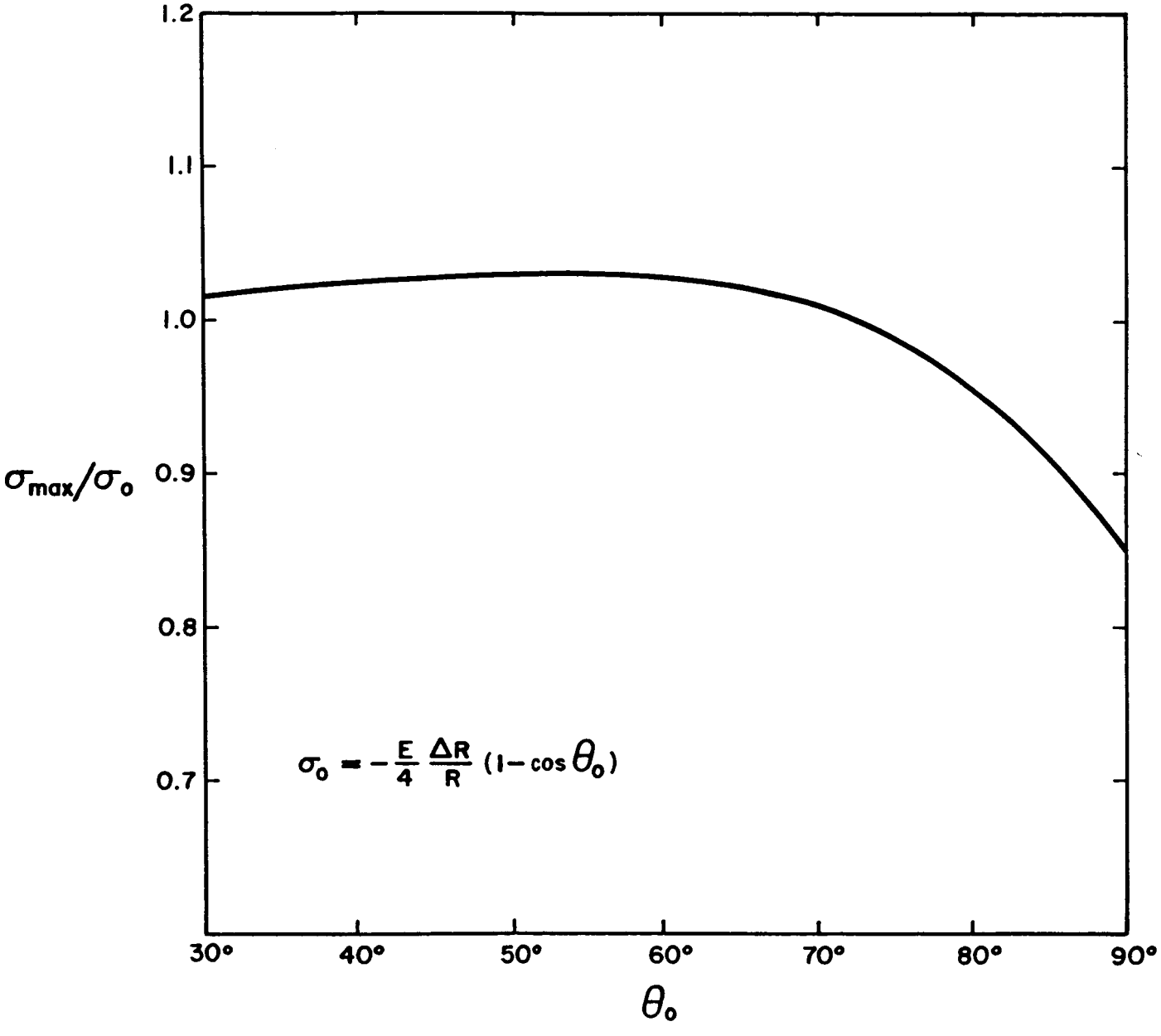
1.2
1.1
1.0
0.9
0.8
0.7
σ_{max}/σ_o
$\sigma_o = -\frac{E}{4}\frac{\Delta R}{R}(1-\cos\theta_o)$
30°
40°
50°
60°
70°
80°
90°
θ_o

Figure 3

APPENDIX 5

(J. Geophys. Res., in press, 1987)

Comment on "Saugus-Palmdale, California, Field Test for Refraction Error in Historical Leveling Surveys" by Ross S. Stein, Charles T. Whalen, Sanford R. Holdahl, William E. Strange, and Wayne Thatcher

Robert Reilinger

Earth Resources Laboratory

Department of Earth, Atmospheric and Planetary Sciences

Massachusetts Institute of Technology

Cambridge, MA 02139

Stein *et al.* (1986) report on the results of field tests designed to determine the effects of atmospheric refraction on historic leveling surveys in Southern California. They use these results to test refraction error models and to correct historical leveling between Saugus and Palmdale for the effects of atmospheric refraction. Stein *et al.* (1986) conclude that the corrected uplift near Palmdale reached 65 ± 16 mm with respect to Saugus during the period 1955-1965, about 30% of the uplift obtained before application of refraction corrections. They further state that "nontectonic subsidence at Saugus is unlikely to have exceeded 9 ± 3 mm, so the tectonic uplift at Palmdale was 56 ± 16 mm".

In this comment I present evidence which strongly suggests that uplift of Palmdale relative to Saugus results entirely from nontectonic subsidence near Saugus. This subsidence together with the refraction corrections derived by Stein *et al.* (1986) in effect eliminates the evidence (at least from the 1955 to 1965 Saugus to Palmdale levelings) for the existence of tectonic uplift near Palmdale. Many of the arguments presented here reiterate results published by Reilinger (1980).

In particular, I will show that:

(1) In addition to the Saugus-Palmdale route, two other leveling routes from Saugus indicate subsidence of Saugus relative to the periphery of the Saugus basin during the period 1953 to 1964.

(2) Observed elevation changes in the Saugus area correlate spatially with aquifer geometry and temporally with the history of the inferred decline in the potentiometric surface[1] within the aquifer.

(3) Subsidence of individual benchmarks above the Saugus aquifer is roughly proportional to the product of aquifer thickness and inferred decline of the potentiometric surface (relation predicted by compaction theory).

(4) The compressibility of the sediments derived from (3) is quite comparable with those reported for other confined aquifers in Southern California.

Figure 1 shows contours of the thickness of the confined Saugus aquifer (Robson, 1972) with leveling lines and benchmarks superimposed. Profiles of elevation change, aquifer thickness and estimated change in potentiometric surface along the survey routes are shown in Figures 2A and B. Elevation changes are derived from observed elevations uncorrected for atmospheric refraction. The absence of refraction corrections does not substantially affect elevation changes within the basin because of the generally low relief in the basin itself (e.g., Strange, 1981, Figures 6, 8, 10). The elevation change profile from north of Castaic through Saugus is plotted assuming stability for benchmark X370 immediately adjacent to the aquifer. This benchmark is chosen as a reference since it lies outside of the aquifer and appears generally stable relative to benchmarks further north. The elevation change profile from Saugus to Lang (portion of Saugus to Palmdale profile) is plotted assuming stability near Lang since the benchmarks immediately adjacent to the Saugus

1. The potentiometric surface of an artesian aquifer is an imaginary surface which coincides with the hydrostatic pressure level of the water in the aquifer.

aquifer occur within the alluvial aquifer of the Santa Clara river and appear to have subsided themselves. Elevation changes along this section of the Saugus-Palmdale route are for the period 1955 to 1961 as these data were used by Reilinger (1980) and were immediately available to me when preparing this comment. Stein *et al.* (1988) report changes along this route for the period 1955 to 1965. However, the arguments made here on the basis of the 1955-1961 data apply to the 1955-1965 profile as well, because of the very similar pattern of deformation for these time periods (Figure 3).

The elevation changes shown in Figures 2 and 3 clearly indicate that the central region of the Saugus basin subsided relative to benchmarks to the south, north, and east during the period 1953 to 1965. This result is independent of any interpretation as to the cause of these movements. In addition, as indicated by Figure 3, by far the largest relative movements along the Saugus to Palmdale profile occur within the Saugus basin. While leveling observations can only provide information on relative movements, certainly the simplest interpretation of the observed elevation changes involves relatively localized subsidence near Saugus rather than broad tectonic uplift of the surrounding regions.

The change in the potentiometric surface shown in Figures 2A and B represents the calculated decline up to 1963 relative to the steady state level estimated to have existed around 1945 (Robson, 1972). This decline was due to pumping from the Saugus aquifer as well as overlying alluvial aquifers, and to an extended drought (Robson, 1972, pp. 8, 40). Because the potentiometric surface was already below the steady state at the time of the first leveling survey (1953), the declines shown in Figures 2A and B are somewhat larger than the actual changes between leveling surveys. However, the important point is that the potentiometric surface continued to decline up to 1963 (Robson, 1972).

Figures 2A and B indicate a reasonable spatial correlation between subsidence, aquifer thickness and change in the potentiometric surface. In addition, the potentiometric surface within the Saugus aquifer stabilized after 1963 and began to recover around 1968 (Robson, 1972). Examination of post-1964 elevation changes across the northern part of the basin indicate a general absence of subsidence of the basin (Figure 4) (also see Strange, 1981, Figure 8 and Reilinger and Brown, 1981, Figure 15). Thus, the observed elevation changes correlate spatially with aquifer geometry and temporally with the history of potentiometric surface decline.

In the ideal case, the amount of compression (subsidence) of a sediment layer is proportional to the thickness of the layer and the increase in effective pressure (grain to grain pressure) on the sediments (Terzaghi and Peck, 1967, p. 278). Lowering the potentiometric surface produces a proportional reduction in the water pressure between grains and hence causes an increase in the effective pressure on the underlying sediments (Terzaghi and Peck, 1967, p. 584). Assuming uniform sediment characteristics throughout the aquifer (constant compressibility), to a first approximation the amount of compaction (subsidence) at a particular location will be roughly proportional to the product of potentiometric surface decline and aquifer thickness. Figure 5 gives a plot of relative subsidence versus the product of the change in potentiometric surface and aquifer thickness for benchmarks in and immediately adjacent to the Saugus aquifer. Considering the uncertainties in aquifer parameters and probable spatial variations in aquifer compressibility, the observations fit the simple linear relationship quite well (correlation coefficient = 0.79). The slope of the regression line in Figure 5 is an estimate of the average compressibility of the Saugus aquifer. Although the compressibility can vary through at least two orders of magnitude depending on sediment type, stress level, and stress history, the value obtained from Figure 5 ($\approx 4 \times 10^{-6} cm^{-1}$) is quite comparable to

those reported for other confined aquifers in California (Lofgren, 1979, p. 35).

Stein *et al.* (1986) allude to results presented by Stein (1981) to argue against subsidence due to compaction of the deep Saugus aquifer. The primary arguments made by Stein (1981) are: 1) from 1953 to 1966 90% of the water was pumped from the unconfined alluvial aquifer, 2) although ground water withdrawal greatly exceeded recharge from 1945 to 1967, the records for the two wells that tap the deep Saugus aquifer do not display the long term head decline that occurred in the overlying alluvial aquifer, and 3) subsidence from 1926 to 1953/55, a period which includes the beginning of ground water level declines, was small relative to the water level declines. He goes on to estimate maximum subsidence of 9 ± 3 mm due to compaction of the alluvial aquifer and discounts subsidence of the underlying deep aquifer.

Thier are a number of problems with the arguments presented by Stein (1981). In regard to the observation that 90 % of the ground water was withdrawn from the alluvial aquifer, Robson (1972) points out (pg. 40) that the decline of the potentiometric surface in the deep confined Saugus aquifer is tied directly to drawdown in the overlying alluvial aquifer. Furthermore, even if we accept that the two deep wells are representative of water levels throughout the Saugus aquifer (a result rejected by Robson, 1972 pg. 39 and apparently contradicted by the general agreement between subsidence and the estimated decline in the potentiometric surface), thier are many examples reported in the literature where subsidence occurs without a long term head decline. Because compaction is in large part anelastic, compaction which occurs during periods of head decline is not recovered when the head rises. For example, Lofgren (1979) presents results from Pixley, California where well over 600 mm of subsidence occurred with no long term decline in water level (Lofgren, 1979; Figure 5).

A further problem with Stein's (1981) estimate of 9 mm as the upper bound for subsidence near Saugus concerns the aquifer compressibility used in his calculations (5×10^{-2} Nm^{-2}). He states that "a compressibility of an order of magnitude higher would be required to account for the observed" subsidence (again assuming that subsidence occurs only in the alluvial aquifer). The compressibility used by Stein (1981) was obtained "from the hysterisis loops of in situ vertical extensometers." This procedure, however, gives the compressibility for elastic aquifer deformation (Riley, 1969). The compressibility for permanent compaction, the cause of land subsidence, is typically an order of magnitude higher (Helm, 1978, Holzer, 1981). Thus, the proper upper bound estimated by Stein's (1981) method (i.e., compaction only in the alluvial aquifer) is greater than the observed subsidence.

Stein's (1981) other argument (subsidence from 1926 to 1953/55 was small relative to water level declines) is actually more supportive than negative. Aquifers commonly have preconsolidation stresses that cause them to be relatively incompressible during the first stages of water level decline (Holzer, 1981). Permanent deformation begins only after this threshold is exceeded.

In conclusion, there is, at the very least, strong circumstantial evidence that the residual "uplift" of Palmdale relative to Saugus for the period 1955 to 1965 is due to nontectonic subsidence at Saugus. This contrasts with the lack of supportive evidence for broad scale tectonic uplift of the Palmdale region during this time period. Subsidence together with refraction corrections in effect eliminates the evidence for tectonic uplift of Palmdale relative to Saugus from this particular data set (Figure 3). In spite of this apparently negative result, it is important to realize that observed subsidence represents real surface movements and in this sense this example further demonstrates the potential importance of historic leveling for monitoring relatively subtle deformation. However, the effectiveness of historic leveling for tectonic studies

in Southern California will continue to be undermined until the influence of nontectonic movements is more clearly recognized by those involved with interpretation of these data.

ACKNOWLEDGMENTS

I am grateful to the National Geodetic Survey for providing the leveling data used in this study. I am also indebted to Tom Holzer for a thoughtful review which substantially improved the manuscript. This research was supported in part by NASA Grant NAG5-814 and NSF Grant 8410366-EAR.

REFERENCES

Helm, D.C., Field verification of a one-dimensional model for transient compaction and extension of a confined aquifer system, in, *Proceedings of the ASCE Specialty Conference on Verification of Mathematical and Physical Models in Hydraulic Engineering*, 189-196, 1978.

Holzer, T.L., Preconsolidation stress of aquifer systems in areas of induced land subsidence, *Water Resources Research, 17*, 693-704, 1981.

Lofgren, B.E., Changes in aquifer-system properties with ground-water depletion, (in) ed., S.K. Saxena, *Evaluation and Prediction of Subsidence*, American Society of Civil Engineers, New York, New York, 26-46, 1979.

Reilinger, R.E., Elevation changes near the San Gabrial fault, Southern California, *Geophys. Res. Ltrs., 11*, 1017-1019, 1980.

Reilinger, R.E. and L.D. Brown, Neotectonic deformation, near-surface movements and systematic errors in U.S. releveling measurements: Implications for earthquake prediction, (in) eds., D.W. Simpson and P.G. Richards, *Earthquake Prediction: An International Review*, Maurice Ewing Ser., v.4, American Geophysical Union, Washington, D.C., 422-440, 1981.

Riley, F.S., Analysis of borehole extensometer data from central California, in, *Land Subsidence, Int. Assoc. Sci. Hydrol. Publ., 89*, 423-431, 1969.

Robson, S.C., Water resources investigation using analog model techniques in the Saugus-Newhall area, Los Angeles County, California, *U.S.G.S. Open*

File Report 5021-04, 58, 1972.

Stein, R., Discrimination of tectonic displacement from slope-dependent errors in geodetic leveling from Southern California, 1953-1979, (in) ed., D.W. Simpson and P.G. Richards, *Earthquake Prediction: An International Review*, Maurice Ewing Ser., v.4, American Geophysical Union, Washington, D.C., 441-455, 1981.

Stein, R.S., C.T. Whalen, S.R. Holdahl, W.E. Strange, and W. Thatcher, Saugus-Palmdale, California, field test for refraction error in historical leveling surveys, *J. Geophys. Res.*, *91*, 9031-9044, 1986.

Strange, W.E., The impact of refraction correction on leveling interpretations in Southern California, *J. Geophys Res.*, *86*, 2809-2824, 1981.

Terzaghi, K., and R.B. Peck, *Soil Mechanics in Engineering Practice*, John Wiley and Sons, New York, 729, 1967.

FIGURE CAPTIONS

Figure 1: Contours (meters) showing thickness of the Saugus aquifer (Robson, 1972). Leveling routes and Benchmarks (dots) crossing the basin are also shown. Dashed lines are faults. From Reilinger (1980).

Figure 2: A) Top: Movement of benchmarks along approximately north-south route plotted versus distance. BM X370 on northern periphery of aquifer assumed stable. Years of leveling surveys shown at top. Middle: Profile of thickness of Saugus aquifer along leveling route (from Robson, 1972). Bottom: Profile of decline in potentiometric surface up to 1963 relative to 1945 datum (from Robson, 1972). B) Profiles along route from north of Saugus to Lang (see Figure 1). Same format as A. From Reilinger (1980).

Figure 3: Comparison of elevation changes for the periods 1955-1965 and 1955-1961 (crosses) along portion of Saugus to Palmdale route. Dashed line shows estimated accumulation of random error. 1955-1965 profiles shown with and without refraction correction. Modified from Stein *et al.* (1986).

Figure 4: Profile of relative elevation change for period 1964 to 1969 along route from north of Castaic to Saugus. From Reilinger (1980).

Figure 5: Plot of subsidence versus change in potentiometric surface times aquifer thickness for benchmarks in and immediately adjacent to aquifer. Different symbols refer to different releveled segments: dots - north of Castaic to Saugus (1953-1964); squares - Saugus to south (1955-1964); triangles - Saugus to Lang (1955-1961). Modified from Reilinger (1980).

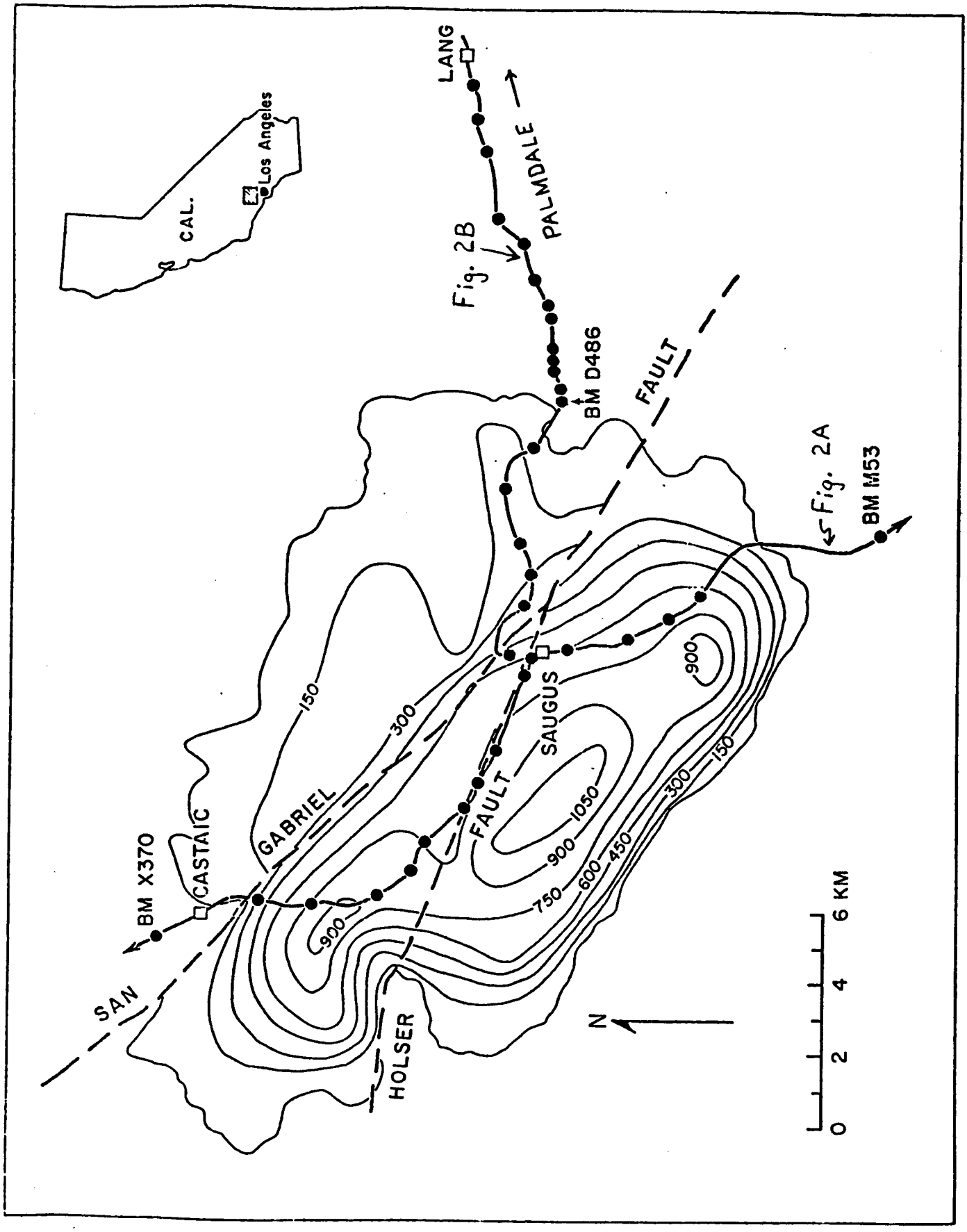
CAL.
Los Angeles
LANG
PALMDALE
Fig. 2B
BM D486
FAULT
Fig. 2A
BM M53
SAUGUS
FAULT
GABRIEL
SAN
HOLSER
CASTAIC
BM X370
150
300
900
1050
750
600
450
N
0 2 4 6 KM

Figure 1

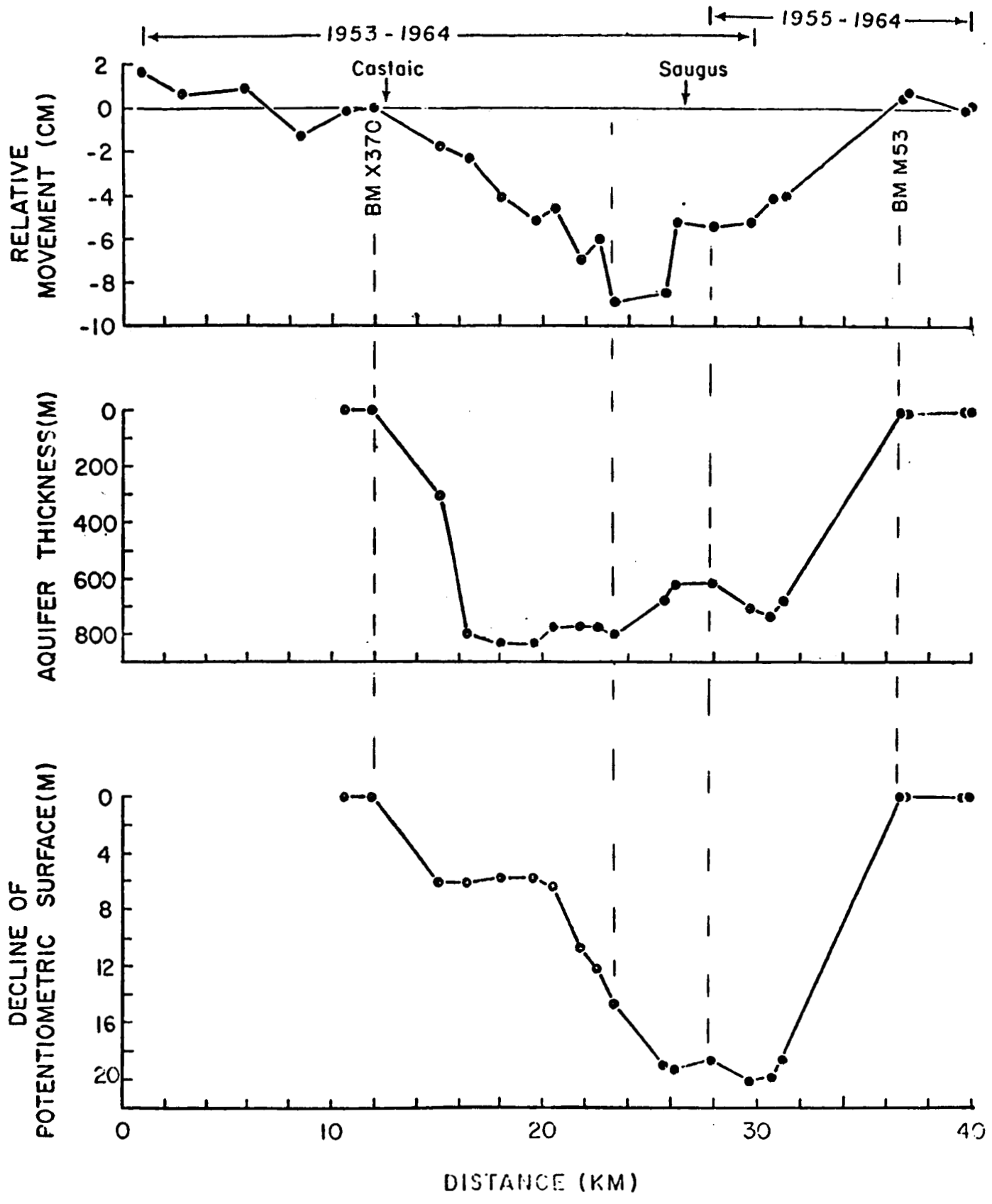
1953 - 1964
1955 - 1964
Castaic
Saugus
BM X370
BM M53
RELATIVE MOVEMENT (CM)
2
0
-2
-4
-6
-8
-10
AQUIFER THICKNESS(M)
0
200
400
600
800
DECLINE OF POTENTIOMETRIC SURFACE(M)
0
4
8
12
16
20
0
10
20
30
40
DISTANCE (KM)

Figure 2A

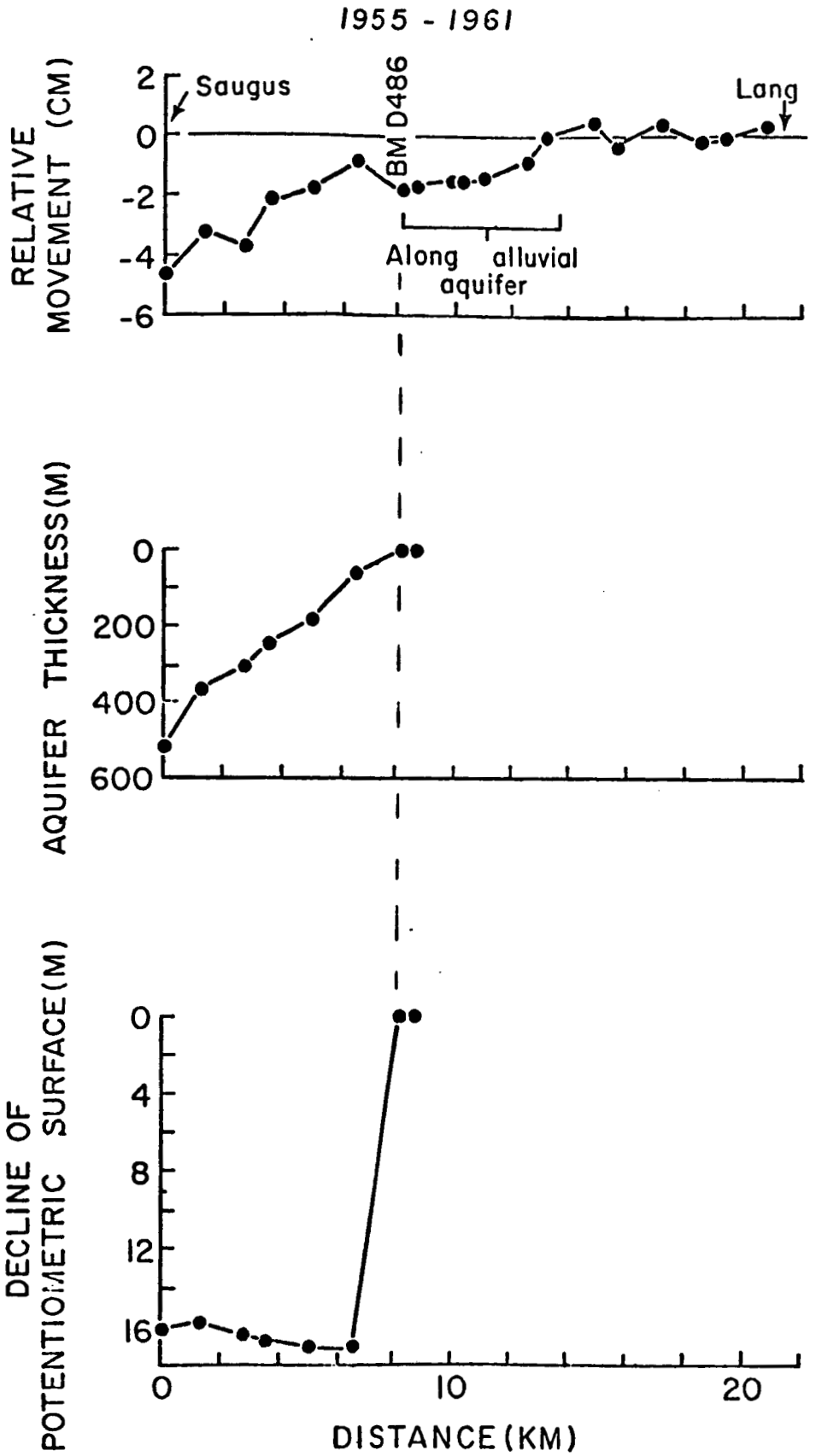
1955 - 1961
RELATIVE MOVEMENT (CM)
2
0
-2
-4
-6
Saugus
BM D486
Lang
Along alluvial aquifer
AQUIFER THICKNESS(M)
0
200
400
600
DECLINE OF POTENTIOMETRIC SURFACE(M)
0
4
8
12
16
0
10
20
DISTANCE (KM)

Figure 2B

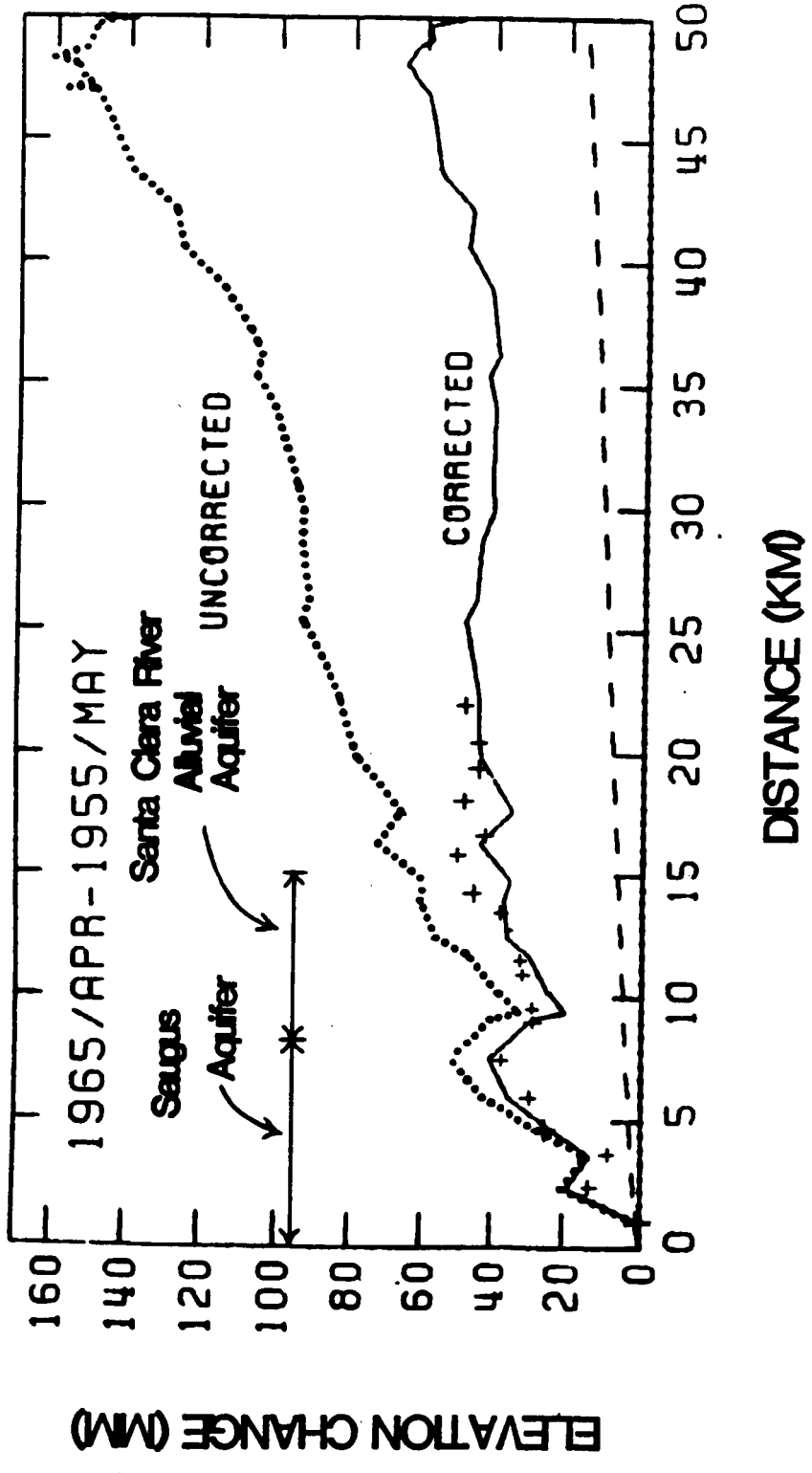
1965/APR-1955/MAY
Santa Clara River Alluvial Aquifer
Saugus Aquifer
UNCORRECTED
CORRECTED
ELEVATION CHANGE (MM)
DISTANCE (KM)
160
140
120
100
80
60
40
20
0
0
5
10
15
20
25
30
35
40
45
50

Figure 3

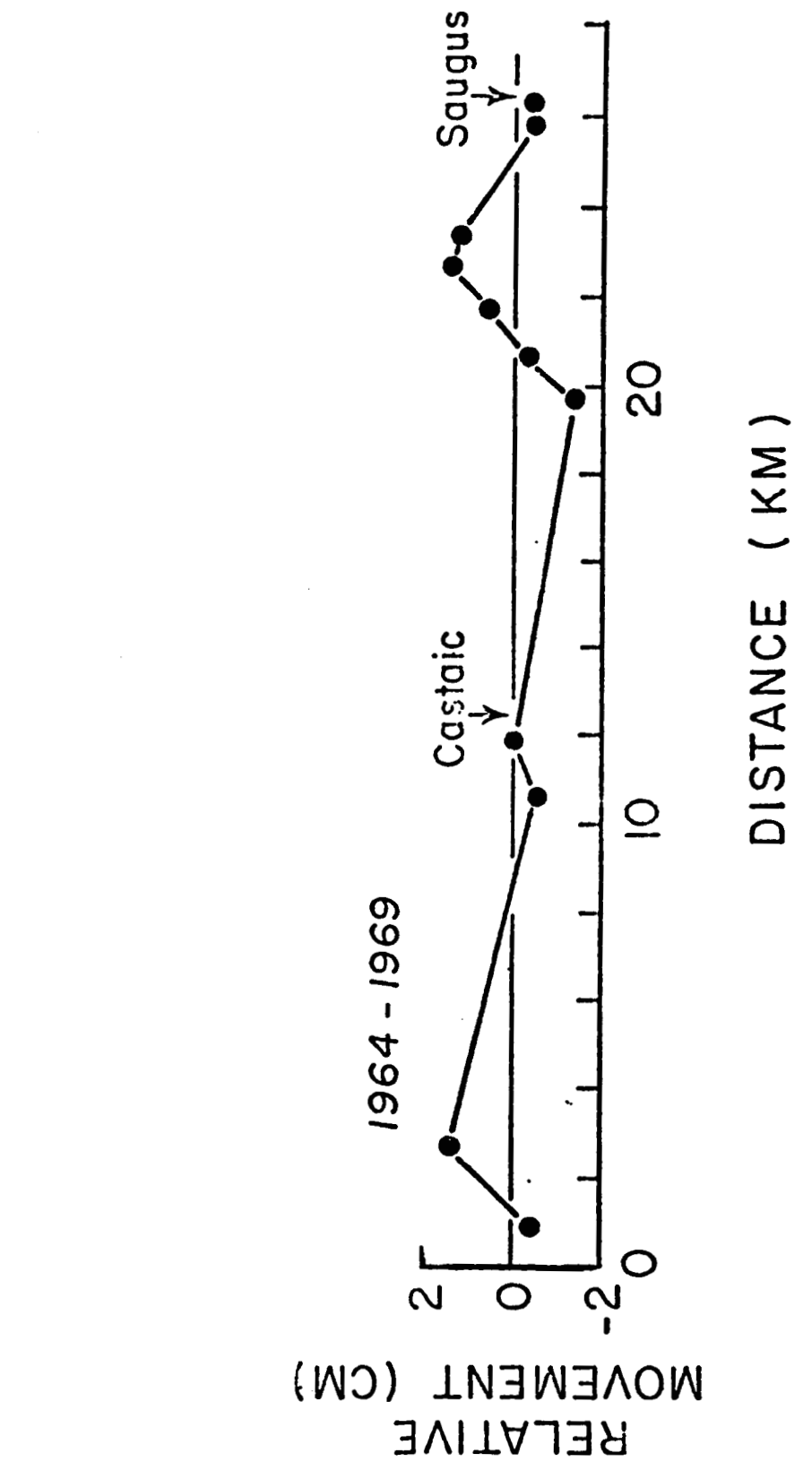
Saugus
Castaic
1964 - 1969
RELATIVE MOVEMENT (CM)
2
0
-2
0
10
20
DISTANCE (KM)

Figure 4

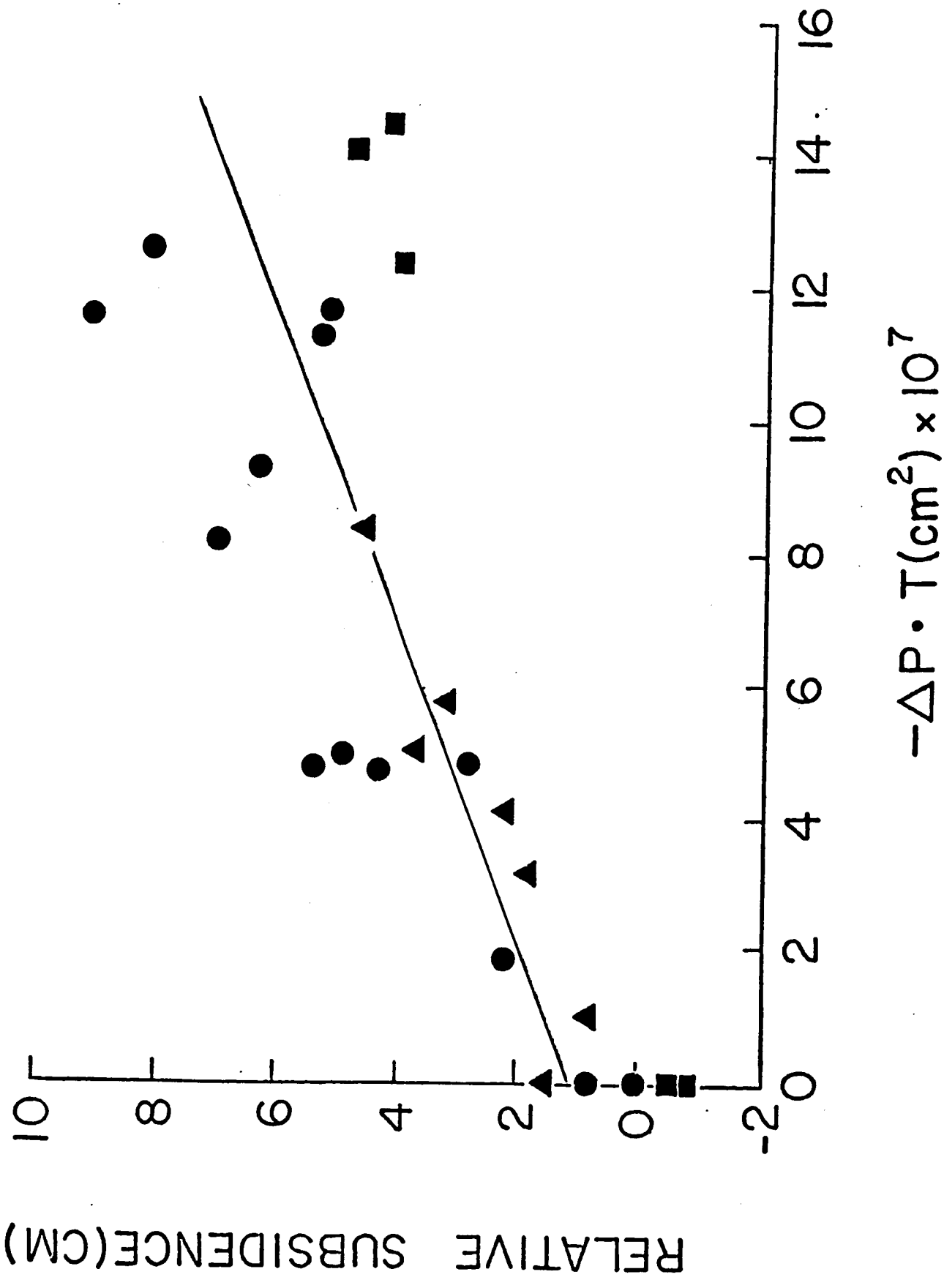
RELATIVE SUBSIDENCE(CM)
10
8
6
4
2
0
-2
-ΔP • T(cm²) x 10⁷
2
4
6
8
10
12
14
16

Figure 5

APPENDIX 6

EARTHQUAKE SOURCE MECHANISMS AND TRANSFORM FAULT TECTONICS IN THE GULF OF CALIFORNIA

John A. Goff,

Eric A. Bergman,

and Sean C. Solomon

Department of Earth, Atmospheric, and Planetary Sciences,

Massachusetts Institute of Technology, Cambridge

Submitted to Journal of Geophysical Research

December 1986

Revised May 1987

ABSTRACT

We have determined the source parameters of 19 earthquakes in the Gulf of California from an inversion of long-period P and SH waveforms. Sixteen of the earthquakes, on transforms between the Cerro Prieto Fault and the Tamayo Fracture Zone, are characterized by right-lateral strike-slip faulting, and all but one of these likely reflect the relative motion between the North American and Pacific plates. Slip vectors from these events constitute an improved data set for determination of North American - Pacific motion. Most centroid depths are poorly resolved because of trade-offs between depth and source time function. Both the ranges in acceptable centroid depths and the average fault width estimated from cumulative moment release during this century are compatible with the hypothesis that seismic slip does not extend below about 10 km depth, or the approximate depth of the nominal 800°C isotherm, along the principal oceanic transforms of the Gulf. Two normal faulting earthquakes during a swarm in the northern Gulf have centroid depths of 6 ± 3 and 3 ± 2 km, consistent with earthquake centroid depths in other settings (Arctic, northern Red Sea) where plate separation has carried continental rifting nearly to completion. A thrust faulting earthquake near the Tres Marias Escarpment has a centroid depth of 11 ± 2 km and probably reflects relative motion between the Rivera and North American plates. The transition from oceanic transform faulting to continental transform faulting in the northern Gulf is marked by a broadening of the zone of deformation and a 10° change in the strike of the principal fault accommodating plate motion. Fault kinematics in the transition zone may be understood in terms of an unstable FFF triple junction, with the Agua Blanca and San Miguel faults acting to transfer a portion of the plate motion to faults west of the San Andreas system and with the Delfin and Wagner basins forming as a direct result of slip on the three fault systems meeting in the junction region.

INTRODUCTION

The source characteristics of large earthquakes in the Gulf of California are of interest for several reasons. The azimuths of slip vectors of earthquakes along the predominantly transform plate boundary in the Gulf provide key constraints on the relative motion between the North American and Pacific plates [*Minster et al.*, 1974; *Chase*, 1978; *Minster and Jordan*, 1978]. The Gulf of California is also the focus of ongoing geodetic programs to determine the distribution of deformation across the plate boundary [*Kasser et al.*, 1987; *Tralli et al.*, 1987], and the history of seismic slip on faults in the Gulf will provide an important context within which the geodetic results can be interpreted. Finally, the region offers an opportunity to test generalizations about the depth extent of seismic slip on transform faults in young oceanic lithosphere [*Burr and Solomon*, 1978; *Engeln et al.*, 1986; *Bergman et al.*, 1986] and along a transition between oceanic and continental transform faulting [*Phillips*, 1964]. In this paper we determine the source mechanisms and centroid depths of 19 earthquakes in the Gulf of California from an inversion of long-period P and SH waveforms [*Nabelek*, 1984].

Several studies of the focal mechanisms of major earthquakes in the Gulf of California have been published [*Sykes*, 1970; *Thatcher and Brune*, 1971; *Molnar*, 1973; *Tatham and Savino*, 1974; *Reichle et al.*, 1976; *Sharman et al.*, 1976; *Mungia et al.*, 1977]. Most of these studies relied primarily on P-wave first motions. The azimuths of the slip vectors indicated by these fault plane solutions have a typical uncertainty of ±10° [*Sykes*, 1970; *Molnar*, 1973]. A forward modeling investigation of the El Golfo earthquake of August 7, 1966, by *Ebel et al.* [1978] represents the only previous use of long-period P and SH waveform data in a source study of an earthquake in the Gulf region. A number of investigations of earthquake aftershocks and swarms in the Gulf of California have also been

conducted with drifting sonobuoys [*Reid et al.*, 1973; *Reichle et al.*, 1976; *Reichle and Reid*, 1977; *Mungia et al.*, 1977].

After a brief introduction to the tectonics of the Gulf of California region in the next section, we summarize the waveform inversion procedure and the estimated precision of derived source parameters. Particular attention is devoted to source complexity, resolution of slip vector azimuth, and resolution of centroid depth. After a discussion of these earthquake source characteristics, we speculate on their implications for the tectonic evolution of the Gulf.

TECTONIC SETTING

The dominant mode of faulting in the Gulf of California (Figure 1) is right-lateral strike-slip motion on transform faults connecting short spreading centers [*Rusnak et al.*, 1964]. The spreading centers are well-developed ridge segments only in the southernmost Gulf; the rest are small pull-apart basins filled to varying degrees by terrigenous and pelagic sediments [*Moore*, 1973; *Lonsdale*, 1985]. Seismic refraction and gravity data indicate that the crustal structure beneath the portions of the Gulf deeper than about 2 km closely resembles that of typical oceanic crust [*Phillips*, 1964; *Harrison and Mathur*, 1964], although the crustal structure is likely to differ from that of normal oceanic crust in detail because of the high sedimentation rate and its potentially strong effect on the processes of shallow igneous intrusion and volcanism [*Moore*, 1973; *Nicolas*, 1985]. Measurements of heat flow [*Lawver and Williams*, 1979; *Williams et al.*, 1979], geomagnetic variation [*White*, 1973a, b], and water column temperature [*Lonsdale and Becker*, 1985] in the Gulf confirm that the basins are sites of active volcanic intrusion and hydrothermal venting. Mantle P-wave velocities to a depth of 350 km beneath the Gulf of California are slow relative to continental and island arc regions [*Walck*, 1984].

Well-documented magnetic anomalies occur only along the Mazatlan Ridge (Figure 2), the spreading center segment to the immediate north of the Tamayo Fracture Zone, and along the East Pacific Rise to the south [*Larson et al.*, 1968; *Larson*, 1972]. A full spreading rate of 58 mm/yr across the Mazatlan Ridge was obtained from two profiles [*Larson et al.*, 1968; *Atwater*, 1970]; a recent reinterpretation of these profiles [*DeMets et al.*, 1986] suggests a somewhat lower rate of 50 mm/yr. The lack of identified magnetic anomalies along other spreading center segments in the Gulf has been attributed by *Larson et al.* [1972] to an

inhibition of extrusive volcanism by the high sediment influx and a consequent reduction of the thermal remanent magnetization of the upper crust.

According to the recent synthesis of the tectonic evolution of the Gulf of California region by *Moore and Curray* [1982], lithospheric extension in the Gulf began 5.5 m.y. ago, when transform motion between the Pacific and North American plates jumped inland from its earlier position along the Tosco-Abreojos Fault zone offshore of what is now the Baja California Peninsula [*Spencer and Normark*, 1979] and movement was initiated on the San Andreas fault . For the next 2 m.y. extension across the Gulf was accomplished primarily by thinning of continental crust through block faulting and listric normal faulting. At about 3.5 m.y. ago, oceanic crust with clear magnetic anomalies began to form along the Mazatlan Ridge in the southern Gulf [*Larson et al.*, 1968; *Larson*, 1972]. A paleogeographic reconstruction derived by restoring 300 km of offset of Baja California [*Gastil and Krummenacher*, 1977] along the direction N124°E closes the Gulf with no remaining oceanic crust and little overlap of continental crustal material [*Moore and Curray*, 1982]. The northern Gulf is completely closed by this reconstruction, whereas the southern Gulf is closed to about the 1-km isobath; the difference may be the result of the large influx of Colorado River sediment in the northern Gulf [*Moore and Curray*, 1982].

EARTHQUAKE DATA SET

To select those earthquakes suitable for body waveform inversion, we searched the catalog of the International Seismological Centre (ISC) for earthquakes in the Gulf of California with body wave magnitude m_b larger than 5.3 during the period 1964 to 1984. We then examined long period seismograms from stations of the World Wide Standard Seismograph Network (WWSSN) for all such events, as well as several large earthquakes in 1963. Some events were omitted from the data set because of poor signal-to-noise ratio or inadequate station coverage. The 19 earthquakes selected for study occurred between 1963 and 1984 and are listed in Table 1. This time period includes an eight-year interval (1976-1984) during which no large ($m_b > 5.3$) earthquakes occurred in the Gulf region.

Because the Gulf of California is marked by variable bathymetry and crustal structure, accurate epicentral location is important to the conduct and interpretation of body waveform inversion studies. Epicenters determined by the ISC for events in the Gulf of California tend to be biased toward the north and east because of the concentration of seismic stations in North America. This effect is most clearly seen for those earthquakes for which detailed aftershock studies have been conducted with sonobuoys, including three of the events listed in Table 1: March 25, 1973, May 31, 1974, and July 8, 1975 [*Reichle et al.*, 1976; *Munguia et al.*, 1977]. For each of these three earthquakes, the centroid of the aftershock zone is about 40 km to the southwest of the ISC epicenter for the main shock. Water column reverberations (compressional waves multiply reflected within the water layer) in the P waveforms may also provide a clue to event mislocation for earthquakes having a significant component of dip-slip faulting. For example, the P waveforms from the August 17, 1969 (2013 UT), earthquake

exhibit prominent water column reverberations at a predominant period inconsistent with the water depth at the ISC location. A good fit can be obtained, however, if the epicenter is relocated to the southwest in the deeper water of the Pescadero Basin complex.

We have assumed that ISC epicenters for large earthquakes in the Gulf of California are mislocated to the northeast by several tens of kilometers. To estimate the water depth in the source region of each earthquake for waveform modelling, we projected the epicenters back to the plate boundary (as defined by bathymetry and mapped fault trends) along the azimuth N150°W, the average azimuth of the epicenter correction vector indicated by the aftershock zones of the three earthquakes noted above. Corrected in this manner, the epicenters of the 19 events of Table 1 are depicted in Figure 2.

WAVEFORM INVERSION

For each of the events listed in Table 1, we determined the parameters of the best-fitting double-couple point source, using a formal inversion of long period teleseismic P and SH waveforms [*Nabelek*, 1984]. In each inversion we solve for the best-fitting point source parameters, including focal mechanism, centroid depth, seismic moment, and source time function. The source time function is parameterized as a series of overlapping triangular elements of assigned number and duration. The relative amplitudes of the elements are determined by the inversion procedure, and the number of elements is chosen so that the end of the source time function approaches zero smoothly. The convention for describing a double-couple source mechanism is that of *Aki and Richards* [1980]. We specify the strike and dip of one nodal plane and the slip angle, which defines the motion of the hanging wall relative to the footwall measured counterclockwise from the strike direction on the footwall; the three angles are given in the order strike/dip/slip. Centroid depths are relative to the seafloor.

For some events a single point source proved inadequate to match the observed waveforms, and two point sources separated in space and time were assumed. In such cases, the timing and location of the second subevent relative to the first, as well as the source parameters of each subevent, were included as parameters in the inversion. For all such complex events, we employed a statistical test to establish the significance of the improvement in fit that resulted from using two point sources, given the increase in the number of free parameters. This test is described in Appendix A.

Seismic velocity structures assumed for the source regions are given in Table 2. For most of the events, the source model was a simple approximation to normal oceanic crustal structure, with a water layer of appropriate thickness and a

single-layer crust over a mantle halfspace. This same velocity structure has been used in our studies of mid-ocean ridge and oceanic intraplate earthquakes [*Bergman et al.*, 1984; *Bergman and Solomon*, 1984, 1985; *Huang et al.*, 1986; *Jemsek et al.*, 1986; *Huang and Solomon*, 1987]. Seismic reflection profiles reported by *Moore* [1973] and by *Niemitz and Bischoff* [1981] indicate that the thickness of sediment in the central part of the Gulf varies considerably but rarely exceeds 1 km. Because of our ignorance of the thickness of the sediment layer at any given epicenter, we included no sediment layer for inversions using the normal oceanic crustal structure. The most significant uncertainty introduced by this omission is in the determination of centroid depth. If the sediments are unconsolidated, so that the sediment-basement interface is a major reflector, then centroid depths will be underestimated by the depth of the sediment thickness. If, in contrast, the seafloor remains the major reflector, then depths will be overestimated by an amount somewhat less than the sediment thickness. As discussed below, the uncertainty in centroid depth for most events is considerably greater than the contribution from unmodeled sediment layers.

For the five northernmost earthquakes in the Gulf region (Figure 2), source models more appropriate to the local crustal structure were adopted. For the August 7, 1966, El Golfo earthquake and the March 20-21, 1969, swarm earthquakes, we adopted the structure assumed by *Ebel et al.* [1978] in their study of the El Golfo event. This crustal model (Table 2) is in agreement with travel times from the most northerly of the seismic refraction lines of *Phillips* [1964]. For the earthquakes of November 18, 1963, and July 8, 1975, we used the structure obtained by *Phillips* [1964] from a reversed refraction line in the Canal de Ballenas; shear wave velocity and density were estimated from V_p in a manner consistent with the model of *Ebel et al* [1978].

The double-couple orientations, centroid depths, and seismic moments of the 19 Gulf of California earthquakes studied are given in Table 1. The focal mechanisms are also displayed in map view in Figure 2. A detailed discussion of the waveform data and inversion results for each earthquake is given in Appendix B. For some events, noted in Appendix B, we have also estimated the length of the rupture zone from the point source solution under the assumption that the source time function may be approximated by the convolution of two boxcar functions, one representing rise time and a longer one representing rupture duration. Except where noted, a rupture velocity of 3.2 km/s has been assumed in order to convert rupture duration to fault length.

It is important to consider the uncertainties in the derived source parameters. For the double couple components, the formal error (2σ) is typically $\pm$ 1° in fault strike and $\pm$ 2° in the dip and slip angles. The formal error in seismic moment is typically $\pm$ 20% and in centroid depth generally $\pm$ 0.4 km. The true uncertainties in these parameters, however, exceed these formal errors. Numerical simulations of waveform inversions by *Nabelek* [1984] have shown that while 2σ is a good estimate of the uncertainty in the seismic moment, the true uncertainties in double couple orientation angles and in centroid depth are generally in the range 5σ – 10σ. These rules of thumb yield uncertainties of $\pm$ 3-5° for fault strike, $\pm$ 5-10° for fault dip and slip, $\pm$ 2 km for centroid depth, and $\pm$ 20% for seismic moment. For earthquakes which can be modeled adequately only with multiple sources, the uncertainties in all parameters are larger by amounts that depend on the particular case. Uncertainties in relative timing and location of multiple subevents and tradeoffs in mechanism parameters that are not reflected in the typical uncertainties are discussed in Appendix B for specific events. For several of the strike-slip earthquakes with little station coverage to the west, there is a tendency

for the northwest-striking nodal plane to dip to the southwest at an apparently significantly non-vertical angle (see Appendix B). This solution results from fitting both the clear P-wave polarity change at stations to the northeast and the relatively large P-wave amplitudes at Central and South American stations to the southeast. While these non-vertical dip angles may thus be real, the P waves at stations to the southeast may be anomalously large because of downward focusing by a narrow zone of low seismic velocities within the mantle beneath the axis of the Gulf [*Walck*, 1984].

Since one of the goals of this study is to obtain an improved set of slip vector azimuths to constrain plate motion models, and since the uncertainty in the slip vector azimuth for strike-slip earthquakes is dominated by the uncertainty in fault strike, we conducted additional tests of the resolution of fault strike. For each event, we fixed the strike at a succession of values distributed about the best fitting value and inverted for the remaining parameters. We then followed the method of *Huang et al.* [1986] to estimate the range of acceptable values for fault strike at a given confidence level. For large earthquakes with good station coverage, the fault strike for the larger subevent is resolved to within $\pm 3°$ at 90% confidence. The smallest strike-slip earthquake (Januray 19, 1971) with good station coverage and seismic moment in excess of 10^{25} dyn cm has an uncertainty in strike of $\pm 4°$ at that confidence. Uncertainties in dip and slip angles also contribute to the uncertainty in the slip vector, though they are much less important than the uncertainty in strike. Taking into consideration the conservatism of the significance test [*Huang et al.*, 1986], a reasonable estimate for the full uncertainty in slip vector azimuth for a Gulf of California strike-slip earthquake with $M_0 > 10^{25}$ dyn cm is $\pm 5°$.

We also examined in detail the resolution of centroid depth. Following

Huang et al. [1986], we fixed the depth at a succession of values distributed about the best fitting value and inverted for the remaining parameters. An example of the resulting curve for residual variance versus centroid depth is shown in Figure 3 for the earthquake of May 31, 1974. The relatively flat character of the residual variance curve between 0 and about 10 km depth indicates that centroid depths in this range cannot be distinguished. Small variations in the residual variance within this depth range are not significant, as they can be quite sensitive to changes in the assumed source parameterization (e.g., length of individual source time function elements) or source velocity structure. This type of residual variance curve is typical of the shallow strike-slip earthquakes of this study, even for events with good signal-to-noise ratio and station coverage.

The relatively flat portion of the residual variance curve in Figure 3 arises because of a nearly complete trade-off between centroid depth and the duration and shape of the source time function. The source time function has a longer duration at the shallowest depths and a shorter duration at greater depths. The trade-off is strong for a vertical strike-slip event, because the two major phases contributing to the P waveform, P and sP, are of like polarity. At the shallowest depths, P and sP add constructively and the shape of the P waveforms determines the shape of the source time function. At greater depth, the separation between P and sP permits a shorter time function. This trade-off is illustrated in Figure 4 by a comparison of observed and synthetic waveforms for several centroid depths for the earthquake of May 31, 1974. The source time functions for the best-fitting solution at each depth are also shown. At assumed centroid depths of 1, 5, and 9 km, the duration of the source time function is 13, 12, and 10 s, respectively. The misfit of synthetic and observed waveforms is nearly indistinguishable for these three solutions. Synthetic seismograms for a solution

at an assumed centroid depth of 16 km, in contrast, provide a poorer fit to the observed waveforms, particularly at KBS.

At very shallow depths, within 2 km of the seafloor, other parameters in the source mechanism also contribute to the trade-off with centroid depth. In particular, the dip angles of the nodal planes depart significantly from the vertical and the seismic moment is nearly doubled (Figure 4). The non-vertical dip angle changes the radiation pattern so that only the down-going or up-going phases contribute to the waveform of a given station, allowing the source time function to control completely the shape of the waveform. This behavior occurs for the other strike-slip events of this study as well. From the standpoint of residuals alone, these extremely shallow solutions cannot be rejected. Some of these solutions may be discounted, however, on the basis of implausible fault geometry or, for the largest events, on the basis of anomalously large implied values of fault slip or fault length.

Resolution of centroid depth for shallow dip-slip events is generally better than for strike-slip events, because P and pP (the most important surface-reflected phase) are typically of opposite polarity. An example of residual variance versus centroid depth for an earthquake with a dip-slip mechanism (February 9, 1976) is shown in Figure 5. A well-defined minimum is apparent at 11 km. A second solution has a centroid at 6 km depth and possesses a longer source time function. The large discontinuous jump in the residual variance at the base of the crust is an artifact of the simplified source velocity structure assumed; the solution at 6 km depth is degraded when a more gradual crust-mantle transition is assumed.

For all events we use the paired *t*-test as described by *Huang et al.* [1986] to estimate confidence limits on centroid depth. Except where noted these limits are

at the 90% confidence level, rounded to the nearest integral depth (in km) outside the formal limits. In cases where there are two or more solutions at different centroid depths or where there is a range of centroid depths over which the residual variance is indistinguishable, the *t*-test is applied only in the vicinity of the deepest and shallowest solutions to estimate the extremes of the confidence interval. Ranges in possible centroid depths are given for each event in Table 2 and are discussed more fully in Appendix B.

EARTHQUAKE COMPLEXITY

For seven of the events of this study, the waveforms contained signals which could not be well matched with a single point source in a horizontally layered structure, even with an extended or multi-peaked source time function. In each of these cases, a significant improvement to the waveforms could be obtained when we modeled these sources as two distinct subevents. Bathymetric variations in the epicentral region may also have contributed to waveform complexity [*Wiens,* 1986]. For three other events, complexity was indicated but the improvement in fit assuming two distinct subevents was not significant at high confidence (see Appendix A). These 10 earthquakes with some signature of complexity include all but two of the events of this study with seismic moment in excess of 2×10^{25} dyn cm. For eight of these ten events, however, the parameters of the second smaller subevent in the assumed two-source model were not well resolved.

The earthquake of July 8, 1975, is a good example of an event requiring a multiple-source solution. This earthquake was well recorded, and its epicentral location in the Canal de Ballenas (Figure 6) is accurately known from the aftershock study of *Munguia et al.* [1977]. The Canal de Ballenas is a region of rugged bathymetry [*Bischoff and Niemitz*, 1980]; considering the large rate of sedimentation in the area, the bathymetric relief suggests a high level of current tectonic activity. From P wave first motions, *Mungia et al.* [1977] obtained a fault plane solution indicating right-lateral strike-slip motion on a vertical fault striking at N130-135°E, and from the surface wave record at one station they estimated a seismic moment of 2×10^{25} dyn cm.

A comparison of the fit of the synthetic waveforms to selected P waves is shown for several source models in Figure 7. For the best fitting point source where the source time function was constrained to be a single pulse, the synthetic

waveforms match the early part of the P waves but do not match the significant arrival of energy about 15 s after initial motion; the variance reduction for the full data set is 58%. If we allow for an extended source time function of arbitrary shape, this misfit is reduced (72% variance reduction) and the source time function displays 2-3 distinct pulses. We next considered a model featuring a point source propagating horizontally at a uniform rupture velocity of 3 km/s. In this model, the source time function at each station has the same shape but is compressed or expanded in time according to a simple function of the rupture velocity, the ray parameter, and the relative azimuth of the rupture direction and the ray path [*Ben-Menahem*, 1962; *Nabelek*, 1985]. Some further improvement over the best point source is obtained for a source propagating to the northwest (76% variance reduction), e.g., in the amplitude and phase of the second cycle of motion at BHP. The duration of the source time function for this model corresponds to a fault about 35 km long, a value somewhat less than the 50-km length of the aftershock zone [*Munguia et al.*, 1977]. In the final model the source consists of two subevents separated in time and space.

The waveforms are best modeled (81% variance reduction) with the two source model (Figures 7 and 8). According to the inversion, the second subevent occurred 8 s later than the first and was located 23 km to the northwest along the strike of the presumed fault plane. The two subevents have nearly identical focal mechanisms (132/93/170 and 130/92/175, respectively) and comparable moments (5.9 and 4.2 x 10^{25} dyn cm, respectively). These mechanisms are similar to that of *Mungia et al.* [1977], but the total moment exceeds their estimate by a factor of 5. The improvement in the fit of the P and SH waveforms with two point sources is significant at the 99% confidence level over the best fitting point source and at 95% confidence over the propagating point source.

The preferred two-source solution is shown in map view and in cross section in Figure 6. The epicentral locations of the subevent centroids are somewhat uncertain and are taken so as to give the closest agreement with the most prominent clusters of aftershocks; the epicenter of the first subevent is near that obtained by *Mungia et al.* [1977] from arrival times at stations around the Gulf of California and in southern California. The fault strikes and relative positions of the two subevents shown in Figure 6 are those derived from the inversion and agree well with the trend of the aftershocks.

The cross-sectional view along the strike of the solution indicates the most significant difference in the source parameters of the two subevents: the centroid depth of the second subevent is at 10 km, 5 km deeper than that of the first subevent. At 90% confidence the centroid depth of the first subevent lies in the range 1-7 km and that of the second subevent lies in the range 9-12 km (Figure 9). The somewhat poorer resolution for the first subevent is the result of a trade-off between the duration of the source time function and centroid depth. A secondary minimum in the curve for residual versus depth for the second subevent also occurs at 2 km, but this solution can be rejected at 90% confidence. The comparatively good resolution of centroid depths for this event is due to good station coverage and signal-to-noise ratio and to the short duration (about 4s) of the principal components of the source time function for each subevent.

SLIP VECTORS AND PLATE MOTIONS

The azimuths of the slip vectors of the strike-slip earthquakes of this study constitute an improved data set for constraining the relative motion between the Pacific and North American plates. Slip vector azimuths for the earthquakes most likely to represent relative plate motion are listed in order of decreasing latitude in Table 3. The slip vector azimuths agree with the local azimuths of the major bathymetric trends of the transform faults [*Bischoff and Henyey,* 1974; *Bischoff and Niemitz*, 1980; *Niemitz and Bischoff*, 1981; *Kastens*, 1981] to within an rms misfit of only 2°. This is in contrast to the slip vectors reported by *Sykes* [1970] and *Molnar* [1973], which are oriented 5° to 10° more southerly than the azimuths of local bathymetric features.

Also shown in Table 3 are the azimuths of Pacific-North American plate motion predicted at the various epicenters by plate kinematic model RM2 [*Minster and Jordan,* 1978]. While the fit of predicted and observed azimuths is quite good, the RM2 azimuths on average exceed the slip vector azimuths by several degrees. J. B. Minster and T. H. Jordan [personal communication, 1986] have recalculated the RM2 angular velocity vectors after correcting and augmenting the data set for azimuths in the Gulf of California with the information in Table 3 and with updated fault trends [*Bischoff and Niemitz*, 1980; *Niemitz and Bischoff*, 1981]. In the resulting solution, denoted by RM2', the pole for North American-Pacific motion is at 50.25°N, 76.03°W, and the angular velocity is 0.837 deg/m.y. These quantities lie within the 95% confidence limits of the RM2 pole coordinates (48.77°N, 73.91°W) and rate (0.852 deg/m.y.) [*Minster and Jordan,* 1978]. The RM2' angular velocity vector reduces the mean squared misfit with the slip vector azimuth data in Table 3 by 50% from that of RM2. Slight but important differences in the azimuth of North American-Pacific plate motion are also predicted elsewhere

along the plate boundary. In particular, for RM2', unlike RM2, the orientation of the creeping portion of the San Andreas fault in central California is not statistically different from the predicted relative plate motion vector [*Minster and Jordan*, 1985]. It should be noted here that RM2' is not a global revision of RM2, but only an updated solution with an improved angular velocity vector for Pacific-North American plate motion [J. B. Minster and T. H. Jordan, personal communication, 1986].

As noted above, the non-vertical dip angle of the indicated fault plane for several earthquakes may be an artifact of incomplete focal sphere coverage or of focusing effects beneath the axis of the Gulf, and a possible bias in the slip vector azimuth may be introduced for these events. Inversion solutions for six of the 12 earthquakes listed in Table 3 have fault planes dipping to the southwest at angles departing by more than 10° from the vertical and striking more westerly than the indicated slip vector azimuth. For the three events having solutions with the shallowest dip angles, we conducted additional waveform inversions during which the fault planes were constrained to be vertical (Appendix B). Slip vector azimuths were reduced by 2-3° compared with the unconstrained inversions, resulting in an improved fit to plate motion model RM2' for two events and a somewhat worsened fit for one event. We conclude that the potential bias in slip vector azimuth due to dip angle error is small, probably 1° or less for most of the events in Table 3, and that the RM2' pole for Pacific-North American plate motion is robust with respect to this level of possible bias.

CENTROID DEPTHS AND FAULT WIDTHS

The centroid depths obtained in this study provide points of comparison with centroid depths determined with similar techniques for events on other oceanic transforms and continental strike-slip fault zones. *Engeln et al.* [1986] applied body waveform modelling techniques to estimate the centroid depths of 29 earthquakes on transform faults in the north and central Atlantic. They found no depths greater than 7 km beneath the seafloor, and they concluded that centroid depths of oceanic transform events are generally limited to depths above the nominal 400°C isotherm, in contrast to the situation in young oceanic lithosphere where centroid depths extend about to the depth of the nominal 800°C isotherm [*Wiens and Stein,* 1983, 1984; *Bergman and Solomon,* 1984]. They further inferred that transform zones must be either anomalously weak or hotter than simple averages of the temperature structure in the lithosphere on either side [*Forsyth and Wilson,* 1984; *Phipps Morgan and Forsyth,* 1987]. More recent body waveform inversion studies of Atlantic transform earthquakes, however, have called these conclusions into question [*Bergman et al.,* 1986].

The centroid depths of several large earthquakes along major strike-slip fault zones in California [*Ebel and Helmberger,* 1982] and China [*Cipar,* 1979; *Chung and Cipar,* 1983; *Zhou et al.,* 1983; *Nabelek et al.,* 1987] have been estimated using body waveform modelling techniques broadly similar to those employed in this paper. Centroid depths range from 6 to 18 km for these events. In general, seismic behavior along continental strike-slip fault zones extends to greater depth than in young oceanic lithosphere [*Chen and Molnar,* 1983].

The large ranges in possible centroid depths for most of the oceanic transform events in the Gulf of California preclude a definitive test of whether the centroids are anomalously shallow relative to intraplate events in young oceanic

lithosphere. The principal transforms between the San Pedro Martir Basin and the East Pacific Rise have offsets between 50 and 120 km (Figure 2). Adopting a simple cooling halfspace model [*Turcotte and Schubert,* 1982] for the thermal structure in young oceanic lithosphere and assuming that the temperature distribution along the transform may be approximated by the arithmetic mean of the expected temperature distribution in the adjacent lithosphere on either side, the nominal 800°C isotherm for an average full spreading rate of 56 mm/yr [*Minster and Jordan,* 1978] is reached at depths between 6 and 10 km along these transforms. Thus the 90% confidence limits on centroid depth for the 11 earthquakes along these transforms in all cases extend deeper than the nominal 800° isotherm.

The one transform event of this study clearly occurring in continental lithosphere is the August 7, 1966, El Golfo earthquake. The centroid depths of the two subevents are 12 and 15 km, but their uncertainties overlap those of oceanic transform events in the Gulf of California and in the north Atlantic [*Bergman et al.,* 1986]. The quite different centroid depths of the two subevents of the July 8, 1975, Canal de Ballenas earthquake (Figure 9), located near the northernmost limit of oceanic crust [*Phillips,* 1964], lead us to speculate that the first and more southerly subevent (5 km centroid depth) may have ruptured oceanic lithosphere but that the second and more northerly subevent at 10 km centroid depth (Figure 6) may have occurred in still-preserved but extended continental lithosphere.

The centroid depths of 6 ± 3 and 3 ± 2 km obtained for the two normal faulting events in the Wagner Basin swarm of March-April 1969 are within the range of centroid depths found in tectonically similar settings. In a study of earthquakes along the Arctic spreading center, *Jemsek et al.* [1986] reported centroid depths of 5-20 km for the portion of the plate boundary crossing the

continental margin of northeastern Asia. *Huang and Solomon* [1987] also obtained centroid depths of 6 km for two normal faulting earthquakes in the extending continental lithosphere of the northernmost Red Sea near the mouth of the Gulf of Suez.

An independent estimate of the depth extent of seismic faulting along transform faults in the Gulf of California is provided by the cumulative release of seismic moment [*Brune,* 1968]. *Reichle et al.* [1976] estimated a moment release in the southern two thirds of the Gulf of California of 3×10^{27} dyn cm for the period 1918-1975. Their estimate was derived from standard seismicity catalogs, a relation between m_b and surface wave magnitude M_s, the M_0-M_s relation of *Brune* [1968], and the assumption that all slip at shallow depths occurred during earthquakes. We have repeated their calculation for the region of the Gulf south of the Delfin Basin for the 80-year period 1904-1984, an interval that includes an M = 7.5 earthquake in 1907 [*Gutenberg and Richter,* 1954] as well as the events of this study. We compiled a list of all events with M_s (or M) greater than or equal to 5.7; sources included *Gutenberg and Richter* [1954] for the period 1904-1952, *Rothé* [1969] for the period 1953-1963, and Table 1 for more recent events. The frequency of events with $M_s < 5.7$ was inferred from the recurrence relation of *Reichle et al.* [1976]. For events prior to 1963, we estimated moments from the relation

$$\log_{10} M_0 = 1.16\, M_s + 18.4$$

obtained by least squares fit to the published moments and magnitudes for about 200 oceanic transform earthquakes in the period 1963-1985 [*S. C. Solomon and D. W. Forsyth*, manuscript in preparation, 1987]; this relation may yield an underestimate of the moment for the very largest ($M_s > 7$) events [*Kanamori and Anderson*, 1975]. The contribution to the cumulative moment from events with M_s

< 5.7 was determined using the method of *Molnar* [1979]. From this procedure we obtained a cumulative moment ΣM_0 of 7×10^{27} dyn cm.

The average fault width w along Gulf of California transforms may be estimated from the relation $w = \Sigma M_0/(\mu L v t)$, where μ is the rigidity, L is the total fault length, v is the average slip rate, and t is the time interval [*Brune*, 1968]. Adopting $\mu = 3.3 \times 10^{11}$ dyn/cm^2, L = 880 km [*Reichle et al.*, 1976], v = 56 mm/yr, and t = 80 yr gives w = 5 km. (For v = 50 mm/yr, w = 6 km.)

It is worth noting that the historical record of large earthquakes, the rate of seismic moment release, and the implied depth extent of seismic faulting differ between transforms in the central and southern Gulf regions. The transforms between the Delfin and Carmen basins (Figure 2) have been the site of 60 percent of the plate boundary earthquakes with $M_s \geq 6$ and all three of the earthquakes with $M_s \geq 7$, despite having a total fault length (470 km) only slightly greater than that of the transforms to the south between the Carmen Basin and the East Pacific Rise (410 km). The total seismic moment released during the period 1904-1984, estimated following the procedure used above, was 5×10^{27} and 2×10^{27} dyn cm for the central and southern Gulf transforms, respectively. The implied average fault widths are 7 and 3 km for v = 56 mm/yr (8 and 4 km for v = 50 mm/yr), respectively. A distinction between the central and southern Gulf has also been drawn by *Rusnak et al.* [1974] on the basis of differences in seafloor morphology and accumulated fault displacements. These differences in maximum earthquake size and average fault width may be related to the likelihood that transform faults in the central Gulf abut scattered blocks of continental to transitional crust and lithosphere [*Phillips*, 1964; *Kastens*, 1981], whereas only young oceanic lithosphere formed at the adjacent spreading centers borders the more evolved transforms of the southern Gulf.

These estimates of the depth extent of seismic faulting along transforms in the Gulf are uncertain by as much as a factor of 2. They are likely, however, to be less than the maximum depth of slip during large earthquakes because of contributions from aseismic slip and underestimates of the largest moments. Values of 3-8 km for the average seismic fault width support centroid depths in the upper half of the ranges cited in Table 1 and are broadly consistent with a maximum depth of seismic slip no greater than the depth of the nominal 800°C isotherm.

FAULT GEOMETRY IN THE NORTHERN GULF REGION

The transition from oceanic to continental transform domains in the northern Gulf of California is marked by several important changes in the nature of faulting. To the south of the Canal de Ballenas, the plate boundary may be traced along a series of well-defined en echelon transform fault zones, each trending approximately along the mean direction of plate motion. To the north, in contrast, plate motion appears to be taken up over a wide zone of deformation that includes faults in northern Baja California as well as the northernmost Gulf (Figure 10). Both the Agua Blanca and San Miguel faults are currently active, on the basis of recent seismicity [*Lomnitz et al.*, 1970; *Reyes et al.*, 1975; *Rebollar et al.*, 1982], large historic earthquakes [*Richter*, 1958; *Shor and Roberts*, 1958; *Allen et al.*, 1965], and Quaternary stream offsets [*Allen et al.*, 1960]. Further, seismic reflection profiles in the northern Gulf [*Henyey and Bischoff*, 1973] suggest a diffuse zone of extensional faulting rather than a traditional ridge-transform geometry. Earthquake swarms are common in the region [*Thatcher and Brune*, 1971; *Tatham and Savino*, 1974]. During the 22 year period of this study, the only large earthquakes in the Gulf to the north of the Delfin Basin have been those in the normal faulting swarm of March-April 1969.

It is also noteworthy that there is a change of approximately 10° in strike between the dominantly oceanic transform in the Canal de Ballenas and the principal continental transform, the Cerro Prieto Fault (Figure 10). In terms of rigid block tectonics, such a change in strike requires that the transition zone act at least instantaneously as a triple junction. We suggest that an FFF triple junction is appropriate (Figure 11). In such a kinematic model, there is compensating motion along a right-lateral, strike-slip fault trending more westerly than the Cerro Prieto Fault. Probably the Agua Blanca and San Miguel faults together accommodate

this motion, which may be transferred from the Gulf via the San Pedro Martir normal fault (Figure 10). The effect of these faults is to transfer a portion of the Pacific-North American plate motion to faults west of the southern San Andreas system [*Allen et al.*, 1960], possibly including offshore faults of the southern California Borderland. The partitioning of slip rate between the Cerro Prieto and Baja California faults can be estimated from the fault geometry if the slip rate along the Canal de Ballenas transform is known. For instance, for a slip rate across the Canal de Ballenas of 50 mm/yr [*DeMets et al.*, 1986], the Cerro Prieto Fault should accommodate 37 mm/yr of slip while 15 mm/yr of right lateral slip should be transferred along faults parallel to the Agua Blanca Fault. The former value is similar to the rate of slip observed along the San Andreas fault in central California [*Thatcher*, 1979]. The latter value is consistent with the occurrence of M_S = 6-7 earthquakes on the Agua Blanca and San Miguel faults [*Richter*, 1958; *Shor and Roberts*, 1958; *Allen et al.*, 1965].

An FFF triple junction is unstable with respect to finite motion [*McKenzie and Morgan*, 1969]. A further consequence of such a fault geometry would be the development of an approximately triangular pull-apart basin (Figure 11). The Delfin and Wagner basins, outlined by diffuse zones of extensional faulting [*Henyey and Bischoff*, 1973], may correspond to this basin predicted from simple kinematics. Neither the dimensions of these basins nor the amount of right-lateral slip documented between Isla Angel de la Guarda and the Baja California peninsula [*Gastil et al.*, 1975] support the presence of an FFF junction of the sort depicted in Figure 11 for the entire history of Gulf opening. We speculate that similar junctions may have been episodically present at more southerly locations earlier in the evolution of the Gulf.

CONCLUSIONS

We have investigated the recent tectonic history of the Gulf of California by means of detailed source studies of 19 large earthquakes that have occurred since 1963, using an inversion of teleseismic long-period P and SH body waveforms. The well constrained focal mechanisms of 12 events judged to represent Pacific-North American relative plate motion provide an improved set of slip vector data for global plate motion inversions. An update of plate motion model RM2 incorporating these new data results in a slight revision to the Pacific-North American rotation pole.

Centroid depths for most of the strike-slip earthquakes are poorly resolved because of trade-offs in the inversion between depth and source time function. For most of these earthquakes the centroid depth can lie anywhere from immediately beneath the seafloor to 10 km or more. The cumulative seismic moment for earthquakes in the Gulf beween 1904 and 1983 indicates a value of 5-6 km for the average seismogenic fault width, though this figure is likely to be less than the maximum depth of slip during large earthquakes. We suggest that most of the larger earthquakes probably have centroid depths of about 5 km. The maximum depth of rupture would then be consistent with the depth to the nominal 800°C isotherm, which appears to limit the depth of rupture for earthquakes in young oceanic lithosphere and on large-offset transforms in the north Atlantic.

Two normal faulting earthquakes in the March-April 1969 swarm in the Wagner Basin have centroid depths of 6 ± 3 and 3 ± 2 km, within the range of earthquake centroid depths observed in other settings (Arctic, northern Red Sea) where plate separation has carried continental rifting nearly to completion. A thrust faulting earthquake near the Tres Marias Escarpment has a centroid depth

of 11 ± 2 km and probably reflects relative motion between the Rivera and North American plates.

The transition from oceanic transform faulting to continental transform faulting in the northern Gulf is marked by a broadening of the zone of deformation and about a 10° change in the strike of the principal fault accommodating plate motion. Fault kinematics in the transition zone may be approximated by that of an unstable FFF triple junction, with the Agua Blanca and San Miguel faults acting to transfer a portion of the plate motion to faults west of the southern San Andreas system, possibly including offshore faults in the California Borderland. By this simple kinematic model, the Delfin and Wagner basins formed as a direct result of slip on the three fault systems meeting in the junction region.

APPENDIX A. Test of Significance of Improved Fit for Multiple-Source Models.

The fit between synthetic and observed waveforms may always be improved by adding parameters to the source model, including the decomposition of the source into several subevents. We wish to test the significance of the improvement in fit given an increase in the number of free parameters. To do this we conduct a test of significance for the differences in station residuals between the best fitting point-source model and the best fitting multiple-source model. By using the residuals at individual stations instead of the residuals at each discrete time sample, we are assured of independent data. This approach leads to a severe underestimate of the number of degrees of freedom, however, and will yield a very conservative result [*Huang et al.*, 1986].

We define the mean square residual for station j as

$$r_j^2 = \frac{1}{M_j} \sum_{i=1}^{M_j} (s_{ij} - o_{ij})^2 \qquad j = 1,2,..., N$$

where s_{ij} and o_{ij} are the amplitudes of the synthetic and observed seismograms at time sample i and station j, M_j is the number of samples in the time window used in the inversion, and N is the number of stations. We denote the mean square residuals for the best fitting point source by r^2_{js} and those for the best fitting multiple source by r^2_{jm}. The set of differences is then defined by

$$d_j = r^2_{js} - r^2_{jm} \qquad j = 1,2,..., N$$

We denote the mean and standard deviation of the set d_j by μ_d and σ_d, respectively. The set of d_j may be regarded as a sample of a normally distributed population of

station residual differences with mean μ_D and standard deviation σ_D [*Huang et al.*, 1986].

We wish to test the null hypothesis that $\mu_D = 0$, but we must take into account the increase in the number of free parameters used in the determination of the multiple-source model. We regard the quantity μ_D as a function of the difference k in the number of parameters used to specify the single and multiple-source models. The number of degrees of freedom of the set d_j is then N-k-1, and the standard deviation σ_d that provides an unbiased estimate of σ_D is given by

$$\sigma^2_d = \frac{1}{N-k-1} \sum_{i=1}^{N} (d_j - \mu_d)^2$$

We test the null hypothesis by forming the statistic

$$t = \frac{\mu_d}{\sigma_d / N^{0.5}}$$

which follows the t distribution with N-k-1 degrees of freedom. Since we are testing the hypothesis that the solution using two point sources is better than the solution using one point source, we use the one-tailed (or one-sided) test.

APPENDIX B. Source Mechanisms from Long-Period Body Waveform Inversion

We present here the details of the source mechanisms determined from the inversion of long-period teleseismic P and SH waveforms for each event.

November 18, 1963

This earthquake occurred to the immediate south of the Delfin Basin along the northern Canal de Ballenas (Figure 2). *Sykes* [1970] obtained a strike slip mechanism (135/109/180) from P wave first motions and S wave polarizations. The best fitting point source (Figure A1) has a predominantly strike slip mechanism on a fault plane that dips to the northeast (131/111/167). The nonvertical dip angle is most evident in the P waveforms at the South American stations, where the P and sP arrivals are of opposite polarity. Because of this polarity difference, the centroid depth is well resolved at 7 ± 2 km at 90% confidence. The seismic moment is 4.6×10^{25} dyn cm.

July 5, 1964

This event was part of a sequence of at least 13 earthquakes that occurred just south of the Carmen Basin (Figure 2) between June 29 and July 6, 1964 [*Thatcher and Brune*, 1971]. A strike-slip mechanism (131/90/180) was determined by *Sykes* [1970] from P wave first motions and S-wave polarizations.

Long period P and SH waveforms for this earthquake are shown in Figure A2. Waveform inversions conducted over a range of centroid depths indicate that there are two point-source solutions, differing principally in the centroid depth, with essentially indistinguishable residuals. The shallower solution (5 km) has a

strike-slip mechanism (128/58/175) and a seismic moment of 4.0×10^{25} dyn cm. The impulsive phase arriving approximately 15 s after the beginning of the first P motion at a number of stations (Figure A2) may indicate a second subevent. While the incorporation of a second subevent results in an improved fit to the waveforms compared with the single point-source model, the mechanism of the second subevent is not well constrained. The deeper solution (13 km) has a nearly identical fault geometry (128/62/171) and moment (4.1×10^{25} dyn cm).

The southwestward dip of the fault plane appears to depart significantly from vertical, a result controlled by the waveforms at stations BHP and ARE. To test whether the slip vector azimuth (131°) for the mechanism in Figure A2 is biased by an incorrect dip angle, we conducted a waveform inversion in which the fault plane was constrained to be vertical. The mechanism (128/90/175) and slip vector azimuth (128°) are very close to those obtained in the unconstrained inversion.

Overall, the resolution of centroid depth for this event is poor. For centroid depths between 0 and 19 km, the length of the source time function trades off with depth so that the fit of synthetic and observed waveforms is not significantly worse at the 85% confidence level than for the two best fitting depths. Solutions at centroid depths less than 3 km, however, display an unlikely mechanism (strike-slip motion on a nearly horizontal fault plane, or dip-slip motion on a nearly vertical plane) and can probably be rejected.

July 6, 1964

This earthquake was the largest event in the sequence of June - July 1964. A strike-slip fault plane solution (135/90/175) was obtained by *Molnar* [1973]. The resolution of the source parameters of this event is degraded somewhat by noise at several stations from earlier events (Figure A3), but in general the waveforms are

quite similar to those for the earthquake of July 5. The best fitting point source has a strike-slip mechanism (129/76/175), a moment of 7.8 x 10^{25} dyn cm, and a centroid depth of 3 km. The statistical test of goodness of fit, however, limits centroid depth only to the range 0-13 km. The focal mechanism solution is similar to that of *Molnar* [1973], but the probable fault plane appears to dip significantly to the southwest.

Febuary 27, 1965

This earthquake occurred on the plate boundary between the San Pedro Martir and Guaymas basins (Figure 2). *Molnar* [1973] determined a strike-slip mechanism (132/80/180) from P wave first motions and S wave polarizations. Station coverage is incomplete (Figure A4) because of the comparatively small moment (M_o = 1.1 x 10^{25} dyn cm). For this reason, the strike-slip mechanism (133/48/190), at 5 km centroid depth, is not particularly robust for this event. The uncertainty in fault strike is ± 5° at 70% confidence. The apparently large departure of the dip angle from vertical is suspect because of the lack of station coverage to the west. Because of these uncertainties, we have excluded this event from slip vector analysis. Because of the trade off with source time function duration, the centroid depth is constrained only to be less than 18 km beneath the seafloor.

August 7, 1966

The August 7, 1966, El Golfo earthquake ruptured a portion of the Cerro Prieto Fault at the northern tip of the Gulf of California (Figure 2). *Sykes* [1970] determined a focal mechanism of 129/70/200 from P wave first motions. *Ebel et al.* [1978] conducted forward modeling of both body waves and surface waves. They obtained a strike-slip mechanism (140/85/183), a centroid depth of 10 km, a body-wave moment of 5 x 10^{25} dyn cm, and a source duration of 4 sec.

Our solution (Figure A5) differs from that of *Ebel et al.* [1978] in several important ways. If a single point source is assumed, two distinct pulses in the source time function, with a total duration of 10 s, are needed to fit the waveforms adequately. In our preferred solution the two pulses are taken to be separate subevents. The improvement in fit of the two-source model over the point-source model is significant at the 99% confidence level. The mechanisms of the two subevents are very similar: 140/51/193 and 141/57/179. The relative timing and location of the second subevent are not well determined. The centroid of the second subevent was located 10-25 km from that of the first in a direction west to northwest. The two subevents may have occurred on the same fault or may have ruptured parallel faults.

The mechanisms of the two subevents differ from the *Ebel et al.* [1978] solution primarily in the dip angle. The dip angle is constrained by the relatively low amplitude of the SH waves and the relatively large P waves at South American stations. *Gastil and Krummenacher* [1977] have documented that all strata in the region older than about 10 m.y. have been tilted by basin-and-range style faulting. We suggest that at least a portion of the Cerro Prieto Fault may have originally been a normal fault which was later reactivated to accommodate transform motion.

In our inversion solution, the moments of the two subevents are 2.5 and 1.4 x 10^{25} dyn cm, respectively. The total moment of 3.9 x 10^{25} dyn cm is thus only slightly less than that reported by *Ebel et al.* [1978]. The centroid depth of the first subevent is 12 km; 90% confidence limits are 9-14 km. This depth is well constrained because of the short duration of the source time function and the clear expression of depth phases on most of the P waveforms. The best-fitting centroid depth for the second subevent is 15 km, but a solution as shallow as 3 km or as deep as 20 km cannot be ruled out.

March 20, 1969

This event was the largest of a swarm of more than 200 earthquakes that occurred between March 20 and April 3, 1969, in the Wagner Basin (Figure 2); 14 of the events were of $m_b \geq 5$ [*Thatcher and Brune*, 1971]. *Thatcher and Brune* [1971] used P wave first motions and S wave polarizations to infer a fault plane solution displaying a combination of strike-slip and normal faulting (50/60/225) and non-orthogonal nodal planes. From the surface wave trace at one station, *Thatcher* [1972] estimated the seismic moment to be 1.3×10^{25} dyn cm. From P_g- P_n times, *Thatcher and Brune* [1971] determined the best average focal depth for the swarm events to be 7 km.

The P wave signal-to-noise ratio and station coverage (Figure A6) are good for a Gulf earthquake of this size. The waveforms are best matched by a nearly pure normal faulting mechanism (23/43/273). The orientation of the nodal planes is well constrained by changes in SH wave polarity between COL and WES and between SJG and NNA, but the SH waveforms are of poor quality. The seismic moment is 4.8×10^{24} dyn cm, less than half the value estimated by *Thatcher* [1972]. The centroid depth is 6 ± 3 km, consistent with the average focal depth for swarm events inferred by *Thatcher and Brune* [1971].

March 21, 1969

This earthquake was one of the larger events in the Wagner Basin swarm. Surface wave arrivals from earlier events severely limited the number of usable SH waveforms (Figure A7) to three stations located at nearly the same azimuth. Station coverage for P waves is also poor, with only about 120° of azimuthal coverage, and the waveforms are severely contaminated by long-period noise. The waveform data

are well-matched with a nearly pure normal faulting mechanism (35/43/274). Despite the poor station coverage, the fault strike, approximately parallel to the trend of spreading center segments in the Gulf, is constrained by the change in SH first motion between CAR and ARE. The centroid depth is 3 ± 2 km at 95% confidence, and the seismic moment is 3.3×10^{24} dyn cm.

April 4, 1969

This earthquake probably occurred beneath the continental shelf of Baja California (Figure 2). From P wave first motions, *Molnar* [1973] determined a normal faulting mechanism (171/45/270). Waveform inversion indicates two possible solutions, both with mechansms similar to that of *Molnar* [1973]. The shallower solution (153/51/264) has a seismic moment of 7.9×10^{24} dyn cm and a centroid depth of 5 km (Figure A8). The deeper (9 km) solution (152/53/163) has a moment (8.3×10^{24} dyn cm) similar to that of the shallower solution. At 90% confidence, the range in possible centroid depths is 2-12 km.

August 17, 1969 (2013 UT)

This was the first event in a sequence of at least 20 earthquakes that occurred in the northern Pescadero Basin complex during August 17 - 19, 1969 [*Thatcher and Brune*, 1971]. *Molnar* [1973] determined a strike-slip mechanism (135/82/176) from P wave first motions and S wave polarizations.

Our best-fitting point source solution (Figure A9) has a strike-slip mechanism (129/76/175), a moment of 6.5×10^{25} dyn cm, a centroid depth of 10 km, and a two-peaked source time function. The range in acceptable centroid depths, however, is 0-17 km at 85% confidence. As mentioned in the text, we regard the prominent water column reverberations in the later portion of the P waveforms as

evidence for a dip-slip secondary event following initial strike-slip motion. The predominant period of these reverberations constrains the water depth in the epicentral region of the second subevent to be 2.3 ± 0.3 km, appropriate to the bathymetry of the northern Pescadero Basin complex (Figure 2). The improvement in fit of the best two-source solution over the point-source solution is significant at the 95% confidence level, but the source parameters of the secondary event are poorly resolved. Both thrust faulting (68/61/120, M_0 = 7.5 x 10^{24} dyn cm, 10 s after the first subevent) and normal faulting (150/65/255, M_0 = 1.2 x 10^{25} dyn cm, 6 s after the first subevent) mechanisms provide equally good fits to the waveforms.

August 17, 1969 (2015 UT)

This earthquake occurred less than two minutes after the one above, but because it was about twice as large, the signal-to-noise ratio is still adequate for waveform inversion (Figure A10). The best-fitting point source has a strike-slip mechanism (126/92/186), a seismic moment of 1.2 x 10^{26} dyn cm, and a centroid depth of 6 km. Similar complexities in the P waveforms from the events of 2013 and 2015 UT (Figures A9 and A10) may be the result of structural effects. A trade off between centroid depth and length of source time function constrains centroid depths only to lie in the range 0-16 km. The ISC locations, if correct, indicate that the two large earthquakes of August 17 ruptured parallel faults separated by approximately 20 km (Figure 2).

We also examined the long period body waves from the third largest earthquake in the sequence, an event on August 18 (0321 UT, m_b = 5.4, M_s = 5.5). Because of interference by surface waves from previous events, the P arrivals are not suitable for inversion. The relative amplitudes of the P and SH waves, however, and the polarity of several clear SH waves and short-period P waves suggest a

evidence for a dip-slip secondary event following initial strike-slip motion. The predominant period of these reverberations constrains the water depth in the epicentral region of the second subevent to be 2.3 ± 0.3 km, appropriate to the bathymetry of the northern Pescadero Basin complex (Figure 2). The improvement in fit of the best two-source solution over the point-source solution is significant at the 95% confidence level, but the source parameters of the secondary event are poorly resolved. Both thrust faulting (68/61/120, $M_0 = 7.5 \times 10^{24}$ dyn cm, 10 s after the first subevent) and normal faulting (150/65/255, $M_0 = 1.2 \times 10^{25}$ dyn cm, 6 s after the first subevent) mechanisms provide equally good fits to the waveforms.

August 17, 1969 (2015 UT)

This earthquake occurred less than two minutes after the one above, but because it was about twice as large, the signal-to-noise ratio is still adequate for waveform inversion (Figure A10). The best-fitting point source has a strike-slip mechanism (126/92/186), a seismic moment of 1.2×10^{26} dyn cm, and a centroid depth of 6 km. Similar complexities in the P waveforms from the events of 2013 and 2015 UT (Figures A9 and A10) may be the result of structural effects. A trade off between centroid depth and length of source time function constrains centroid depths only to lie in the range 0-16 km. The ISC locations, if correct, indicate that the two large earthquakes of August 17 ruptured parallel faults separated by approximately 20 km (Figure 2).

We also examined the long period body waves from the third largest earthquake in the sequence, an event on August 18 (0321 UT, $m_b = 5.4$, $M_s = 5.5$). Because of interference by surface waves from previous events, the P arrivals are not suitable for inversion. The relative amplitudes of the P and SH waves, however, and the polarity of several clear SH waves and short-period P waves suggest a

normal faulting mechanism, with nodal planes striking approximately north-south, and a shallow centroid depth.

The complexities indicated by the faulting during this swarm mirror the complexities shown in the mapped traces of faults in the Pescadero Basin complex. *Niemitz and Bischoff* [1981] show a series of faults in this region which vary considerably in trend; they propose further that the Pescadero Basin complex has not yet developed into a stable spreading center.

November 1, 1969

This large and complex earthquake occurred at the mouth of the Gulf on the Tamayo Fracture Zone (Figure 2). *Molnar* [1973] obtained a strike-slip mechanism (135/96/172) for this event from P wave first motions. *Sharman et al.* [1976] reevaluated the first motion data and obtained a slightly different mechanism (127/90/180).

We model this earthquake as a horizontally propagating point source, which is an improvement over a fixed point source at the 90% level of significance. Because of the extremely emergent character of the P waves (Figure A11), evident on both long and short period records, it is quite difficult to establish the correct alignment between synthetic and observed waveforms. Energetic arrivals approximately 25 s into the P waveforms are notable at most stations. We were unable to model these arrivals, however, even with a multiple-source model. The best-fitting propagating point source has a strike-slip mechanism (122/77/175) and a moment of 1.1×10^{26} dyn cm. Rupture occurred in a northwesterly direction; at an assumed rupture velocity of 3.2 km/s, the fault length is about 20 km. The best fitting centroid depth is 6 km, but no depth shallower than 13 km can be excluded at 90% confidence.

January 19, 1971

This earthquake occurred on the transform portion of the plate boundary between the Pescadero Basin complex and the Mazatlan Ridge (Figure 2). The main features of the long period waveforms for this event (Figure A12) are well matched by a strike-slip mechanism (127/84/176), a moment of 1.2×10^{25} dyn cm, and a centroid depth of 4 km. A simple trapezoidal source time function suggests a fault length of about 15 km. A second, nearly indistinguishable, minimum in the residual-versus-depth curve occurs at 7 km; the mechanism (127/83/177) and moment (1.3×10^{25} dyn cm) are nearly identical to those of the shallower solution. The full range in possible centroid depths at 90% confidence is 0-10 km. The fit between synthetic and observed SH waveforms for the solution in Figure A12 is good. Additional energy arriving approximately 10 s after the onset of the P waves is suggestive of a complex source. Inversions with two point sources indicate that the second subevent may be characterized by high-angle normal faulting, but the improvement in fit is not significant at greater than 70% confidence because of the low signal-to-noise ratio of the P waveforms. We have not included a second subevent in our source model of this earthquake because of the uncertainty in its source parameters.

September 30, 1971

This earthquake occurred between the Guaymas and Carmen basins (Figure 2). Station coverage for P and SH waveforms is excellent, and the signal-to-noise ratio is very good at most stations. This event displays complex P waveforms and probably involved multiple subevents. We are unable to resolve the mechanisms of any but the primary subevent, however. The best-fitting point source (Figure A13)

has a strike-slip mechanism (128/85/179), a seismic moment of 6.7 x 10^{25} dyn cm, and a centroid depth of 7 km. At 90% confidence the centroid depth lies in the range 0-11 km.

March 25, 1973

This earthquake occurred between the Carmen and Farallon basins (Figure 2). *Reichle et al.* [1976] employed P wave first motions and surface wave radiation patterns to obtain a strike-slip mechanism (147/90/180). They estimated a moment of 4.6 x 10^{24} dyn cm and a centroid depth of 1-3 km from surface wave amplitude spectra. They also noted the anomalous strike of the probable fault plane for this earthquake, which deviates by approximately 20° from the trend of the main bathymetric escarpments in the Gulf. *Reichle et al.* [1976] also reported aftershock locations obtained from a small network of drifting sonobuoys. On the basis of these locations they inferred that this event occurred along a 10-15 km length of fault near, but distinct from, the principal transform, and they argued that the anomalous trend represents a recent development in the pattern of local faulting, subsidiary to the main trend of transform faulting in the Gulf. Waveform inversion (Figure A14) yields a source mechanism (153/94/190) and moment (4.6 x 10^{24} dyn cm) similar to those obtained by *Reichle et al.* [1976] and a centroid depth of 9 km. The range in possible centroid depths at 90% confidence is 0-13 km. The short duration and simple trapezoidal shape of the source time function (Figure A14) are consistent with the fault length of 10-15 km inferred from aftershock locations [*Reichle et al.*, 1976].

May 31, 1974

This earthquake occurred on the transform fault just south of the Guaymas Basin (Figure 2). *Reichle et al.* [1976] deployed sonobuoys in the epicentral area within 36 hours of the main shock; they inferred a 20-30 km length for the aftershock zone and suggested that aftershock focal depths were approximately 3-5 km. The station coverage and signal-to-noise ratio of the P and SH waveform data for this earthquake are excellent. The best fitting point source solution (Figure A15) has a predominantly strike-slip mechanism (123/65/169) and a moment of 3.8×10^{25} dyn cm. The slip vector azimuth (128°) is reduced by 2° in an inversion solution obtained with the fault plane constrained to be vertical. The centroid depth for the solution in Figure A15 is 5 km, but the centroid depth trades off with the duration of the source time function, and any value in the range 0-10 km is permitted by the waveform data. The source time function is consistent with a fault length of about 25 km, a value comparable to the length of the aftershock zone.

July 8, 1975

This event is described fully in the text.

September 24, 1975

This earthquake occurred at the northern end of the Pescadero Basin complex (Figure 2). The best fitting point source (Figure A16) has a strike-slip mechanism (129/72/173), a seismic moment of 1.6×10^{25} dyn cm, and a centroid depth of 9 km. The residuals are not significantly worse, however, for any centroid depth in the range 0-14 km. An inversion conducted with the fault plane constrained to be vertical yielded a mechanism with a slip vector azimuth 2° less than that for the solution in Figure A16. A two source model improves the fit to the waveforms; while

the mechanism of the secondary subevent appears to involve dip-slip motion, it is poorly resolved.

Febuary 9, 1976

This event occurred near the Tres Marias Escarpment (Figure 2) and probably represents motion between the North American and Rivera plates. On the basis of P wave first motions, *Eissler and McNally* [1984] inferred a strike-slip fault plane solution, a mechanism which supports the prediction of *Minster and Jordan* [1979] for the direction of North American - Rivera relative motion in that region. Such a mechanism is not compatible with the body waveform data, however (Figure A17). A thrust faulting mechanism (92/52/86), a moment of 7.1 x 10^{24} dyn cm, and a centroid depth of 11 ± 2 km provide a good fit to the observed data. A second minimum in the residual-versus-depth curve is present at the base of the crust (6 km), but this solution is not robust with respect to changes in the source velocity model (see text). H.K. Eissler (personal communication, 1985) acknowledged that for P waves near nodal directions some of the first motions reported by *Eissler and McNally* [1984] may be in error due to reading pP rather than P as the dominant phase.

February 10, 1984

This earthquake occurred on the transform just north of the Guaymas Basin (Figure 2). Using a semi-automated centroid moment tensor inversion scheme, *Dziewonski et al.* [1984] obtained a strike-slip mechanism (121/101/190) and a seismic moment of 1.3 × 10^{25} dyn cm. Body waveform inversion yields a best fitting point source (Figure A18) with similar mechanism (127/96/182) and moment (1.2 ×

10^{25} dyn cm). The best fitting centroid depth is 6 km, but at 90% confidence the centroid depth is constrained only to lie in the range 0 -12 km. The two distinct peaks in the source time function (Figure A18) are not well constrained; such a source time function is consistent with the P-waveforms at most South American stations, but at the three stations at the most northerly azimuths the inital P motion appears to be opposite in polarity to that in the synthetic waveforms.

Acknowledgements. We appreciate constructive discussions with Charles DeMets, Holly Eissler, Paul Huang, Tom Jordan, Kim Kastens, Bernard Minster, Jeanne Sauber, and Joann Stock, and we thank John Nabelek and Jason Phipps Morgan for copies of papers in advance of publication. Bernard Minster and Tom Jordan kindly calculated the RM2' angular velocity vector for Pacific-North American motion using the new slip vector azimuths obtained in this study. We also thank Mark Carlson and Laura Doughty for their assistance with manuscript preparation and Joe Engeln and a second reviewer for helpful comments on an earlier draft. This research was supported by the National Science Foundation under grants EAR-8416192 and EAR-8617967 and by the National Aeronautics and Space Administration under contract NAS 5-27339 and grant NAG 5-814.

REFERENCES

Aki, K., and P. G. Richards, *Quantitative Seismology: Theory and Methods*, vol. 1, 557 pp., W. H. Freeman, San Francisco, Calif., 1980.

Allen, C. R., L. T. Silver, and F. G. Stehli, Agua Blanca Fault - A major transverse structure of northern Baja California, Mexico, *Geol. Soc. Am. Bull., 71*, 457-482, 1960.

Allen, C. R., P. St. Amand, C. F. Richter, and J. M. Nordquist, Relationship between seismicity and geologic structure in the southern California region, *Bull Seismol. Soc. Amer., 55,* 753-797, 1965.

Atwater, T., Implications of plate tectonics for the Cenozoic tectonic evolution of western North America, *Geol. Soc. Am. Bull., 81,* 3513-3536, 1970.

Ben-Menahem, A., Radiation of seismic body waves from a finite moving source in the Earth, *J. Geophys. Res., 67,* 345-350, 1962.

Bergman, E. A., and S. C. Solomon, Source mechanisms of earthquakes near mid-ocean ridges from body waveform inversion: Implications for the early evolution of oceanic lithosphere, *J. Geophys. Res., 89*, 11415-11441, 1984.

Bergman, E. A., and S. C. Solomon, Earthquake source mechanisms from body-waveform inversion and intraplate tectonics in the northern Indian Ocean, *Phys. Earth Planet. Inter., 40,* 1-23, 1985.

Bergman, E. A., J. L. Nabelek, and S. C. Solomon, An extensive region of off-ridge normal faulting earthquakes in the southern Indian Ocean, *J. Geophys. Res., 89,* 2425-2443, 1984.

Bergman, E. A., S. C. Solomon, and J. A. Goff, Source processes of large earthquakes on north Atlantic transform faults (abstract), *Eos Trans. AGU, 67,* 1230, 1986.

Bischoff, J. L., and T. L. Henyey, Tectonic elements of the central part of the Gulf of California, *Geol. Soc. Am. Bull., 85,* 1893-1904, 1974.

Bischoff, J. L., and J. W. Niemitz, Bathymetric maps of the Gulf of California, map I-1244, U.S. Geological Survey, Reston, Va., 1980.

Brune, J. N., Seismic moment, seismicity, and rate of slip along major fault zones, *J. Geophys. Res., 73,* 777-784, 1968.

Burr, N. C., and S. C. Solomon, The relationship of source parameters of oceanic transform earthquakes to plate velocity and transform length, *J. Geophys. Res., 83,* 1193-1205, 1978.

Chase, C. G., Plate kinematics: The Americas, East Africa, and the rest of the world, *Earth Planet. Sci. Lett., 37,* 355-368, 1978.

Chen, W.-P., and P. Molnar, Focal depths of intracontinental and intraplate earthquakes and their implications for the thermal and mechanical properties of the lithosphere, *J. Geophys. Res., 88,* 4183-4214, 1983.

Chung, W.-Y., and J. J. Cipar, Source modeling of the Hsingtai, China earthquakes of March 1966, *Phys. Earth Planet. Inter., 33,* 111-125, 1983.

Cipar, J., Source processes of the Haicheng, China earthquake from observations of P and S waves, *Bull. Seismol. Soc. Am., 69,* 1903-1916, 1979.

DeMets, C., R. G. Gordon, S. Stein, D. Argus, and D. Woods, Pacific - North America spreading rate in the Gulf of California (abstract), *Eos Trans. AGU, 67,* 905, 1986.

Dziewonski, A. M., J. E. Franzen, and J. H. Woodhouse, Centroid-moment tensor solutions for January-March, 1984, *Phys. Earth Planet. Inter., 34,* 209-219, 1984.

Ebel, J. E., and D. V. Helmberger, P-wave complexity and fault asperities: The Borrego Mountain, California, earthquake of 1968, *Bull. Seismol. Soc. Am., 72,* 413-437, 1982.

Ebel, J. E., L. J. Burdick, and G. S. Stewart, The source mechanism of the August 7,

1966 El Golfo earthquake, *Bull. Seismol. Soc. Am.*, *68*, 1281-1292, 1978.

Eissler H. K., and K. C. McNally, Seismicity and tectonics of the Rivera plate and implications for the 1932 Jalisco, Mexico, earthquake, *J. Geophys. Res.*, *89*, 4520-4530, 1984.

Engeln, J. F., D. A. Wiens, and S. Stein, Mechanisms and depths of Atlantic transform earthquakes, *J. Geophys. Res.*, *91*, 548-577, 1986.

Forsyth, D. W., and B. Wilson, Three-dimensional temperature structure of a ridge-transform-ridge system, *Earth Planet. Sci. Lett., 70,* 355-362, 1984.

Gastil, R. G., and D. Krummenacher, Reconnaissance geology of coastal Sonora between Puerto Lobos and Bahia Kino, *Geol. Soc. Am. Bull.*, *88*, 187-198, 1977.

Gastil, R. G., R. P. Phillips, and E. C. Allison, *Reconnaissance Geology of the State of Baja California, Mem. 140,* 170 pp., Geol. Soc. Am., Boulder, Colo., 1975.

Gutenberg, B., and C. F. Richter, *Seismicity of the Earth and Associated Phenomena,* 2nd ed., Princeton Univ. Press, Princeton, N.J., 310 pp., 1954.

Harrison, J. C., and S. P. Mathur, Gravity anomalies in Gulf of California, in *Marine Geology of the Gulf of California, Mem 3*, edited by Tj. van Andel and G. G. Shor, Jr., pp. 76-89, Am. Assoc. Petrol. Geol., Tulsa, Okla., 1964.

Henyey, T. L., and J. L. Bischoff, Tectonic elements of the northern part of the Gulf of California, *Geol. Soc. Am. Bull.*, *84*, 315-330, 1973.

Huang, P. Y., and S. C. Solomon, Centroid depths and mechanisms of mid-ocean ridge earthquakes in the Indian Ocean, Gulf of Aden, and Red Sea, *J. Geophys. Res.*, *92*, 1361-1382, 1987.

Huang, P. Y., S. C. Solomon, E. A. Bergman, and J. L. Nabelek, Focal depths and mechanisms of Mid-Atlantic Ridge earthquakes from body waveform inversion, *J. Geophys. Res.*, *91*, 579-598, 1986.

Jemsek, J. P., E. A. Bergman, J. L. Nabelek, and S. C. Solomon, Focal depths and

mechanisms of large earthquakes on the Arctic mid-ocean ridge system, *J. Geophys. Res., 91,* 13993-14005, 1986.

Kanamori, H., and D. L. Anderson, Theoretical basis of some empirical relations in seismology, *Bull. Seismol. Soc. Amer., 65,* 1073-1095, 1975.

Kasser, M., J.-C. Ruegg, Ph. Lesage, L. Ortlieb, J. Pagarete, N. Duch, J. Guerrero, and J. Roldan, Geodetic measurements of plate motions across the central Gulf of California, 1982-1986, *Geophys. Res. Lett., 14,* 5-8, 1987.

Kastens, K. A., Deep tow survey of a transform fault between oceanic and continental crust, Guaymas Basin, Gulf of California (abstract), in *Abstracts with Program, 13,* p. 63, Geol. Soc. Am., Boulder, Colo., 1981.

Larson, P. A., J. D. Mudie, and R. L. Larson, Magnetic anomalies and fracture-zone trends in the Gulf of California, *Geol. Soc. Am. Bull., 83,* 3361-3368, 1972.

Larson, R. L., Bathymetry, magnetic anomalies, and plate tectonic history of the mouth of the Gulf of California, *Geol. Soc. Am. Bull., 83,* 3345-3360, 1972.

Larson, R. L., H. W. Menard, and S. M. Smith, Gulf of California: A result of ocean floor spreading and transform faulting, *Science, 161,* 781-784, 1968.

Lawver, L. A. and D. L. Williams, Heat flow in the central Gulf of California, *J. Geophys. Res., 84,* 3465-3478, 1979.

Lomnitz, C., F. Mooser, C. R. Allen, J. N. Brune, and W. Thatcher, Seismicity and tectonics of the northern Gulf of California, Mexico. Preliminary results, *Geofis. Internat., 10,* 37-48, 1970.

Lonsdale, P., A transform continental margin rich in hydrocarbons, Gulf of California, *Amer. Ass. Petrol. Geol. Bull., 69,* 1160-1180, 1985.

Lonsdale, P., and K. Becker, Hydrothermal plumes, hot springs, and conductive heat flow in the southern trough of Guaymas Basin, *Earth Plan. Sci. Lett., 73,* 211-225, 1985.

McKenzie, D. P., and W. J. Morgan, Evolution of triple junctions, *Nature, 224,* 125-133, 1969.

Minster, J. B., and T. H. Jordan, Present-day plate motions, *J. Geophys. Res., 83,* 5331-5354, 1978.

Minster, J. B., and T. H. Jordan, Rotation vectors for the Philippine and Rivera plates (abstract), *Eos Trans. AGU, 60,* 958, 1979.

Minster, J. B., and T. H. Jordan, Vector constraints on Quartenary deformation of the western United States east and west of the San Andreas Fault, in *Tectonics and Sedimentation Along the California Margin,* edited by J. K. Crouch and S. B. Bachman, Soc. Econ. Paleontol. Mineral., Pacific Section, *38,* 1-16, 1984.

Minster, J. B., and T. H. Jordan, Self-consistent modeling of western U. S. deformation (abstract), *Eos Trans. AGU, 66,* 849, 1985.

Minster, J. B., T. H. Jordan, P. Molnar, and E. Haines, Numerical modeling of instantaneous plate tectonics, *Geophys. J. Roy. Astron. Soc., 36,* 541-576, 1974.

Molnar, P., Fault plane solutions of earthquakes and direction of motion in the Gulf of California and on the Rivera Fracture Zone, *Geol. Soc. Am. Bull., 84,* 1651-1658, 1973.

Molnar, P., Earthquake recurrence intervals and plate tectonics, *Bull. Seismol. Soc. Amer., 69,* 115-133, 1979.

Moore, D. G., Plate-edge deformation and crustal growth, Gulf of California structural province, *Geol. Soc. Am. Bull., 84,* 1883-1905, 1973.

Moore, D. G., and J. R. Curray, Geologic and tectonic history of the Gulf of California, *Init. Repts. Deep Sea Drilling Proj., 64,* 1279-1294, U. S. Govt. Printing Office, Washington, D. C., 1982.

Munguia, L., M. Reichle, A. Reyes, R. Simons, and J. Brune, Aftershocks of the 8 July, 1975 Canal de las Ballenas, Gulf of California, earthquake, *Geophys. Res. Lett., 4,*

507-509, 1977.

Nabelek, J. L., Determination of earthquake source parameters from inversion of body waves, Ph. D. thesis, 346 pp., Mass. Inst. of Technol., Cambridge, 1984.

Nabelek, J., Geometry and mechanism of faulting of the 1980 El Asnam, Algeria, earthquake from inversion of teleseismic body waves and comparison with field observations, *J. Geophys. Res., 90,* 12713-12728, 1985.

Nabelek, J. L., W.-P. Chen, and H. Ye, The Tangshan earthquake sequence and its implications for the evolution of the North China Basin, *J. Geophys. Res.*, in press, 1987.

Nicolas, A., Novel type of crust produced during continental rifting, *Nature, 315,* 112-115, 1985.

Niemitz, J. W., and J. L. Bischoff, Tectonic elements of the southern part of the Gulf of California, *Geol. Soc. Am. Bull., part II, 92,* 360-407, 1981.

North American Geologic Map Committee, *Geologic Map of North America,* 1:5,000,000, U. S. Geological Survey, Reston, Va., 1965.

Phillips, R. P., Seismic refraction studies in Gulf of California, in *Marine Geology of the Gulf of California, Mem. 3,* edited by Tj. van Andel and G. G. Shor Jr., pp. 90-121, Am. Assoc. Petrol. Geol., Tulsa, Okla., 1964.

Phipps Morgan, J., and D. W. Forsyth, 3-D flow and temperature perturbations due to a transform offset: Effects on oceanic crustal and upper mantle structure, *J. Geophys. Res.,* in press, 1987.

Poppe, B. B., D. A. Naab, and J. S. Perry, Seismograph station codes and characteristics, U. S. Geol. Survey Circular 791, 171 pp., 1978.

Rebollar, C. J., A. Reyes, and M. Reichle, Estudia del enjambre de San Quintin, Baja California, Mexico, ocurrido durante 1975, *Geofis. Internat., 21,* 331-358, 1982.

Reichle, M. S., and I. Reid, Detailed study of earthquake swarms from the Gulf of

California, *Bull. Seismol. Soc. Amer., 67,* 159-171, 1977.

Reichle, M. S., G. F. Sharman, and J. N. Brune, Sonobouy and teleseismic study of Gulf of California transform fault earthquake sequences, *Bull. Seismol. Soc. Am., 66,* 1623-1641, 1976.

Reid, I., M. Reichle, J. Brune, and H. Bradner, Microearthquake studies using sonobuoys, preliminary results from the Gulf of California, *Geophys. J. Roy. Astron. Soc., 34,* 365-379, 1973.

Reyes, A., J. Brune, T. Barker, L. Canales, J. Madrid, J. Rebollar, and L. Mungia, A microearthquake survey of the San Miguel fault zone, Baja California, Mexico, *Geophys. Res. Lett., 2,* 56-59, 1975.

Richter, C. F., *Elementary Seismology,* pp. 531-533, W. H. Freeman, San Francisco, 1958.

Rothé, J. P., *The Seismicity of the Earth,* UNESCO, Paris, 336 pp., 1969.

Rusnak, G. A, R. L. Fisher, and F. P. Shepard, Bathymetry and faults of Gulf of California, in *Marine Geology of the Gulf of California, Mem. 3,* edited by Tj. H. van Andel and G. G. Shor, Jr., pp. 59-75, Am. Assoc. Petrol. Geol., Tulsa, Okla., 1964.

Sharman, G., M. S. Reichle, and J. N. Brune, Detailed study of relative plate motion in the Gulf of California, *Geology, 4,* 206-210, 1976.

Shor, G. G., Jr., and E. Roberts, San Miguel, Baja California Norte, earthquakes of February, 1956, *Bull. Seismol. Soc. Amer., 48,* 101-116, 1958.

Spencer, J. E., and W. R. Normark, Tosco-Abreojos fault zone: A Neogene transform plate boundary within the Pacific margin of southern Baja California, Mexico, *Geology, 7,* 554-557, 1979.

Sykes, L. R., Focal mechanism solutions for earthquakes along the world rift system, *Bull. Seismol. Soc. Am., 60,* 1749-1752, 1970.

Tatham, R. H., and J. M. Savino, Faulting mechanisms for two oceanic earthquake

swarms, *J. Geophys. Res., 79,* 2643-2652, 1974.

Thatcher, W., Regional variations of seismic source parameters in the northern Baja California area, *J. Geophys., Res., 77,* 1549-1565, 1972.

Thatcher, W., Systematic inversion of geodetic data in central California, *J. Geophys. Res., 84,* 2283-2295, 1979.

Thatcher, W., and J. Brune, Seismic study of an oceanic ridge earthquake swarm in the Gulf of California, *Geophys. J. R. Astron. Soc., 22,* 473-489, 1971.

Tralli, D. M., T. H. Dixon, L. L. Skrumeda, S. A. Stephens, C. Vegos, J. M. Davidson, P. Dauphin, and F. Suarez-Vidal, GPS baselines across the Gulf of California (abstract), *Eos Trans. AGU, 68,* 283, 1987.

Turcotte, D. L., and G. Schubert, *Geodynamics,* John Wiley and Sons, New York, 450 pp., 1982.

Walck, M. C., The P-wave upper mantle structure beneath an active spreading centre: The Gulf of California, *Geophys. J. R. Astron. Soc., 76,* 697-723, 1984.

White, A., A geomagnetic variation anomaly across the northern Gulf of California, *Geophys. J. R. Astron. Soc., 33,* 1-25, 1973a.

White, A., Anomalies in geomagnetic variations across the central Gulf of California, *Geophys. J. R. Astron. Soc., 33,* 27-46, 1973b.

Wiens, D. A., Effects of bathymetry on teleseismic P waveforms (abstract), *Eos Trans. AGU, 67,* 1105, 1986.

Wiens, D. A., and S. Stein, Age dependence of oceanic intraplate seismicity and implications for lithospheric evolution, *J. Geophys. Res., 88,* 6455-6968, 1983.

Wiens, D. A., and S. Stein, Intraplate seismicity and stresses in young oceanic lithosphere, *J. Geophys. Res., 89,* 11442-11464, 1984.

Williams, D. L., K. Becker, L. A. Lawver, and R. P. Von Herzen, Heat flow at the spreading centers of the Guaymas Basin, Gulf of California, *J. Geophys. Res., 84,*

6757-6769, 1979.

Zhou, H., H.-L. Liu, and H. Kanamori, Source processes of large earthquakes along the Xianshuihe fault in southwestern China, *Bull. Seismol. Soc. Am.*, *73*, 537-551, 1983.

E. A. Bergman, J. A. Goff, and S. C. Solomon, Department of Earth, Atmospheric, and Planetary Sciences, Building 54-526, Massachusetts Institute of Technology, Cambridge, MA 02139

FIGURE CAPTIONS

Figure 1. Principal active faults in the Gulf of California region, simplified from *North American Geologic Map Committee* [1965]. Spreading centers are denoted by double lines (dashed where inferred), strike-slip faults by single lines, and thrust faults by barbed lines (dashed where inferred).

Figure 2. Epicenters and source mechanisms obtained by body waveform inversion for large earthquakes in the Gulf of California. Epicentral positions include an approximate correction to account for the systematic northeastward mislocation by ISC for earthquakes in this region (see text). Events modeled with more than one point source are indicated by overlapping mechanisms, reading left-to-right in order of occurrence; the relative location of subevent epicenters is shown. Fault plane solutions are equal area projections of the lower focal hemisphere; compressional quadrants are shaded. Important bathymetric features, including ridges (shaded), basins (interior tics), and transforms (dashed), are simplified from *Bischoff and Niemitz* [1980] and *Niemitz and Bischoff* [1981].

Figure 3. Residual variance versus centroid depth for the earthquake of May 31, 1974. Individual points on this curve were obtained by fixing the centroid depth and inverting for the combination of the remaining parameters (mechanism, moment, source time function) that best fit the body waveforms. The residual variance equals the mean squared misfit of synthetic to observed waveforms normalized by the mean squared observed waveforms. Arrows delimit the 90% confidence limits on centroid depth according to the paired *t*-test of *Huang et al.* [1986].

Figure 4. Observed P waveforms (solid lines) at selected stations for the

earthquake of May 31, 1974, together with synthetic waveforms (dashed lines) for the best-fitting point source solution at each of several fixed centroid depths. The mechanism, moment, and source time function (S.T.F.) indicated by the inversion of the full set of P and SH waveforms at each fixed centroid depth are also shown.

Figure 5. Residual variance versus centroid depth for the earthquake of February 9, 1976. See Figure 3 for explanation.

Figure 6. Mainshock and aftershock locations for the earthquake of July 8, 1975, from *Munguia et al.* [1978]. Also shown are the ISC epicenter and the source mechanisms of the two subevents as obtained from waveform inversion. The second subevent occurred 8 s later than and 23 km northwest of the first. Bathymetric contours, in meters, are from *Bischoff and Niemetz* [1980].

Figure 7. Comparison of observed (solid lines) and synthetic (dashed lines) P waves at selected stations for the earthquake of July 8, 1975. Synthetic waveforms for four different source models are shown: (1) the best fitting point source with a source time function (S.T.F.) constrained to a single pulse; (2) the best fitting point source with a source time function unconstrained except for total duration; (3) a propagating point source (southeast to northwest) with a source time function unconstrained except for total duration; and (4) the best fitting model with two distinct point sources; the source time function for the second subevent is indicated by the dashed line.

Figure 8. Comparison of observed P and SH waves (solid lines) from the July 8, 1975, earthquake with synthetic waveforms (dashed lines) generated using a model consisting of two point sources, the parameters of which

were found from body-waveform inversion. Full names and locations of all stations are given by *Poppe et al.* [1978]. P and SH radiation patterns are shown on the lower focal hemisphere (equal area projection). The source-time functions of the two subevents obtained from the inversion are also shown. The dashed lines in the source time function and focal mechanism represent the second subevent. The delay between the centroid times of the subevents is shown; the apparent delay at any station depends on the angle between the line joining the subevents and the ray path to the station. All amplitudes are normalized to a WWSSN instrument magnification of 3000 and an epicentral distance of 40°; the amplitude scales correspond to the waveforms that would be observed on an original seismogram from such an instrument. The two vertical lines delimit the portion of each time series used in the inversion. Symbols for both types of waves are open circles, dilatation; closed circle, compression; cross, emergent arrival. For SH waves, compression corresponds to positive motion as defined by *Aki and Richards* [1980].

Figure 9. Residual variance versus centroid depth for the best two-source solution to the inversion of P and SH waveforms for the Gulf of California earthquake of July 8, 1975. In these inversions, the centroid depth is held fixed for either the first (squares) or second (circles) subevent at the indicated value. The arrows denote the 90% confidence intervals for the centroid depths of the two subevents.

Figure 10. Major faults and bathymetry in the northern Gulf of California region, from *Rusnak et al.* [1964]. Bathymetric contours are in fathoms.

Figure 11. Kinematic model of the effect of a difference in strike (a) between the transforms in adjacent oceanic and continental lithosphere in the northern

Gulf. The model predicts (b) motion on a compensating right-lateral transform fault, creating an FFF triple junction, and the formation of a triangular basin (hatched region). The three faults of the model may be schematically associated with the Canal de Ballenas transform fault and the Cerro Prieto and Agua Blanca/San Miguel faults; one possible configuration of slip rate vectors is shown in the inset.

Figure A1. Comparison of observed P and SH waves from the earthquake of November 18, 1963, with synthetic waveforms for the best-fitting point source. See Figure 8 for further explanation.

Figure A2. Comparison of observed P and SH waves from the earthquake of July 5, 1964, with synthetic waveforms for the best-fitting point source. See Figure 8 for further explanation.

Figure A3. Comparison of observed P and SH waves from the earthquake of July 6, 1964, with synthetic waveforms for the best-fitting point source. See Figure 8 for further explanation.

Figure A4. Comparison of observed P and SH waves from the earthquake of Febuary 27, 1965, with synthetic waveforms for the best-fitting point source. See Figure 8 for further explanation.

Figure A5. Comparison of observed P and SH waves from the earthquake of August 7, 1966, with synthetic waveforms for a model with two point sources, the parameters of which were found from body-waveform inversion. See Figure 8 for further explanation.

Figure A6. Comparison of observed P and SH waves from the earthquake of March 20, 1969, with synthetic waveforms for the best-fitting point source. See Figure 8 for further explanation.

Figure A7. Comparison of observed P and SH waves from the earthquake of March

21, 1969, with synthetic waveforms for the best-fitting point source. See Figure 8 for further explanation.

Figure A8. Comparison of observed P and SH waves from the earthquake of April 4, 1969, with synthetic waveforms for the best-fitting point source. See Figure 8 for further explanation.

Figure A9. Comparison of observed P and SH waves from the earthquake of August 17, 1969 (2013 UT), with synthetic waveforms for the best-fitting point source. See Figure 8 for further explanation.

Figure A10. Comparison of observed P and SH waves from the earthquake of August 17, 1969 (2015 UT), with synthetic waveforms for the best-fitting point source. See Figure 8 for further explanation.

Figure A11. Comparison of observed P and SH waves from the earthquake of November 1, 1969, with synthetic waveforms for the best-fitting point source. See Figure 8 for further explanation.

Figure A12. Comparison of observed P and SH waves from the earthquake of January 19, 1971, with synthetic waveforms for the best-fitting point source. See Figure 8 for further explanation.

Figure A13. Comparison of observed P and SH waves from the earthquake of September 30, 1971, with synthetic waveforms for the best-fitting point source. See Figure 8 for further explanation.

Figure A14. Comparison of observed P and SH waves from the earthquake of March 25, 1973, with synthetic waveforms generated for the best-fitting point source. See Figure 8 for further explanation.

Figure A15. Comparison of observed P and SH waves from the earthquake of May 31, 1974, with synthetic waveforms generated for the best-fitting point source. See Figure 8 for further explanation.

Figure A16. Comparison of observed P and SH waves from the earthquake of September 24, 1975, with synthetic waveforms for the best-fitting point source. See Figure 8 for further explanation.

Figure A17. Comparison of observed P and SH waves from the earthquake of Febuary 9, 1976, with synthetic waveforms for the best-fitting point source. See Figure 8 for further explanation.

Figure A18. Comparison of observed P and SH waves from the earthquake of February 10, 1984, with synthetic waveforms for the best-fitting point source. See Figure 8 for further explanation.

Table 1. Epicentral Data and Source Parameters for Earthquakes in the Gulf of California.

Date	Origin Time, UT	Latitude, °N	Longitude, °W	m_b	M_S	M_o[a]	Mechanism[b]	Range in Possible Centroid Depth,[c] km
Nov. 18, 1963[d]	1438:26.2	29.68	113.74	5.7	6.6[e]	4.6	131/111/167	7 ± 2
July 5, 1964	1908:00.1	26.34	110.21	5.7	6.3[e]	4.0[f]	128/58/175[f]	0 - 19
July 6, 1964	0214:36.7	26.32	110.28	5.6	6.6[e]	7.8	129/76/175	0 - 13
Feb. 27, 1965	0746:28.6	28.38	112.27	5.4	6.0[e]	1.1	133/48/190	0 - 18
Aug. 7, 1966[g]	1736:28.5	31.74	114.31	5.7	6.3[h]	2.5 1.4	140/51/193 141/57/179	12 ± 3 3 - 20
Mar. 20, 1969	0817:45.1	31.32	114.18	5.3	5.7	0.48	23/43/273	6 ± 3
Mar. 21, 1969	0634:26	31.25	114.31	5.6	5.4	0.33	35/43/274	3 ± 2
Apr. 4, 1969	1616:19.6	24.44	109.80	5.5		0.79[f]	153/51/264[f]	2 - 12
Aug. 17, 1969	2013:09.3	25.25	109.24	5.6		6.5	129/76/175	0 - 17
Aug. 17, 1969	2015:00.8	25.12	109.55	5.8	6.6	12.	126/92/186	0 - 16
Nov. 1, 1969[i]	1108:24.3	23.19	107.99	5.5	6.6	11.	122/77/175	0 - 13
Jan. 19, 1971	0316:54.2	23.80	108.73	5.5	5.9	1.2[f]	127/84/176[f]	0 - 10
Sept. 30, 1971	0817:59.8	26.88	110.80	5.7	6.6	6.7	128/85/179	0 - 11
Mar. 25, 1973	2242:01	25.84	109.93	5.4	5.5	0.46	153/94/190	0 - 13
May 31, 1974	1405:01.9	27.36	111.13	5.4	6.3	3.8	123/65/169	0 - 10
July 8, 1975[g]	0937:28.9	29.49	113.40	5.6	6.5	5.9 4.2	132/93/170 130/92/175	1 - 7 10 ± 2
Sept. 24, 1975	1719:37.8	25.20	109.26	5.5	5.7	1.6	129/72/173	0 - 14
Feb. 9, 1976	2129:57.0	21.63	106.59	5.6	5.4	0.71	92/52/086	11 ± 2
Feb. 10, 1984	1651:21	28.29	112.14	5.5	6.2	1.2	127/96/182	0 - 12

Epicentral and magnitude data are taken from the ISC, except where noted.

a Seismic moments in units of 10^{25} dyn cm (10^{18} N m).
b Focal mechanism (strike/dip/slip, all in degrees) specified with convention of *Aki and Richards* [1980].
c Relative to the seafloor.
d Epicenter from *Sykes* [1970].

e Magnitude M from *Rothé* [1969].
f Source parameters are for the shallower of two possible solutions (see text).
g This event modeled with more than one point source.
h From *Ebel et al.* [1978].
i This event modeled as a point source propagating to the northwest at 3.2 km/s.

Table 2. Seismic Velocity Models Assumed for the Source Regions of Specified Earthquakes.

Thinned Continental Crust (August 7, 1966, and March 20-21, 1969)

Layer	Thickness, km	V_p, km/sec	V_s, km/sec	ρ, g/cm^3
1	1.2	1.8	0.5	1.0
2	2.3	4.0	2.4	1.8
3	4.3	5.4	3.2	2.4
4	16.2	6.7	3.9	3.0
5	Halfspace	7.8	4.6	3.4

Transitional Crust (November 18, 1963, and July 8, 1975)

1	1.1	1.5	0	1.0
2	0.9	2.0	0.6	1.1
3	10.0	5.5	3.2	2.4
4	Halfspace	7.6	4.5	3.3

Normal Oceanic Crust (all other events)

1	Variable	1.5	0	1.0
2	6.0	6.4	3.7	2.6
3	Halfspace	8.1	4.6	3.4

Table 3. Comparison of Earthquake Slip Vectors with Bathymetric Trends and Plate Motion Models

Earthquake	Azimuth of Slip Vector	Azimuth of Bathymetric Trend[a]	Predictions of Plate Motion Models			
			RM2 Azimuth[b]	RM2 Residual	RM2' Azimuth[c]	RM2' Residual
Nov. 18, 1963	125°	—	136°	11°	133°	8°
July 8, 1975[d]	132°	—	136°	4°	133°	1°
Feb. 10, 1984	127°	125°	134°	7°	131°	4°
May 31, 1974	128°	127°	133°	5°	130°	2°
Sept. 30, 1971	128°	127°	133°	5°	130°	2°
July 5, 1964	131°	128°	132°	1°	129°	-2°
July 6, 1964	130°	128°	132°	2°	129°	-1°
Aug. 17, 1969 (2013 UT)	131°	130°	130°	-1°	127°	-4°
Sept. 24, 1975	132°	130°	130°	-2°	127°	-5°
Aug. 17, 1969 (2015 UT)	126°	130°	130°	4°	127°	1°
Jan. 19, 1971	127°	127°	129°	2°	126°	-1°
Nov. 1, 1969	123°	119°	128°	5°	125°	2°

[a]From *Bischoff and Henyey* [1974], *Bischoff and Niemitz* [1980], *Niemitz and Bischoff* [1981], and *Kastens* [1981].

[b]From Pacific-North American plate motion pole, model RM2 [*Minster and Jordan,* 1978].

[c]From Pacific-North American plate motion pole, model RM2' [J. B. Minster, personal communication, 1986].

[d]Slip vector is for first subevent.

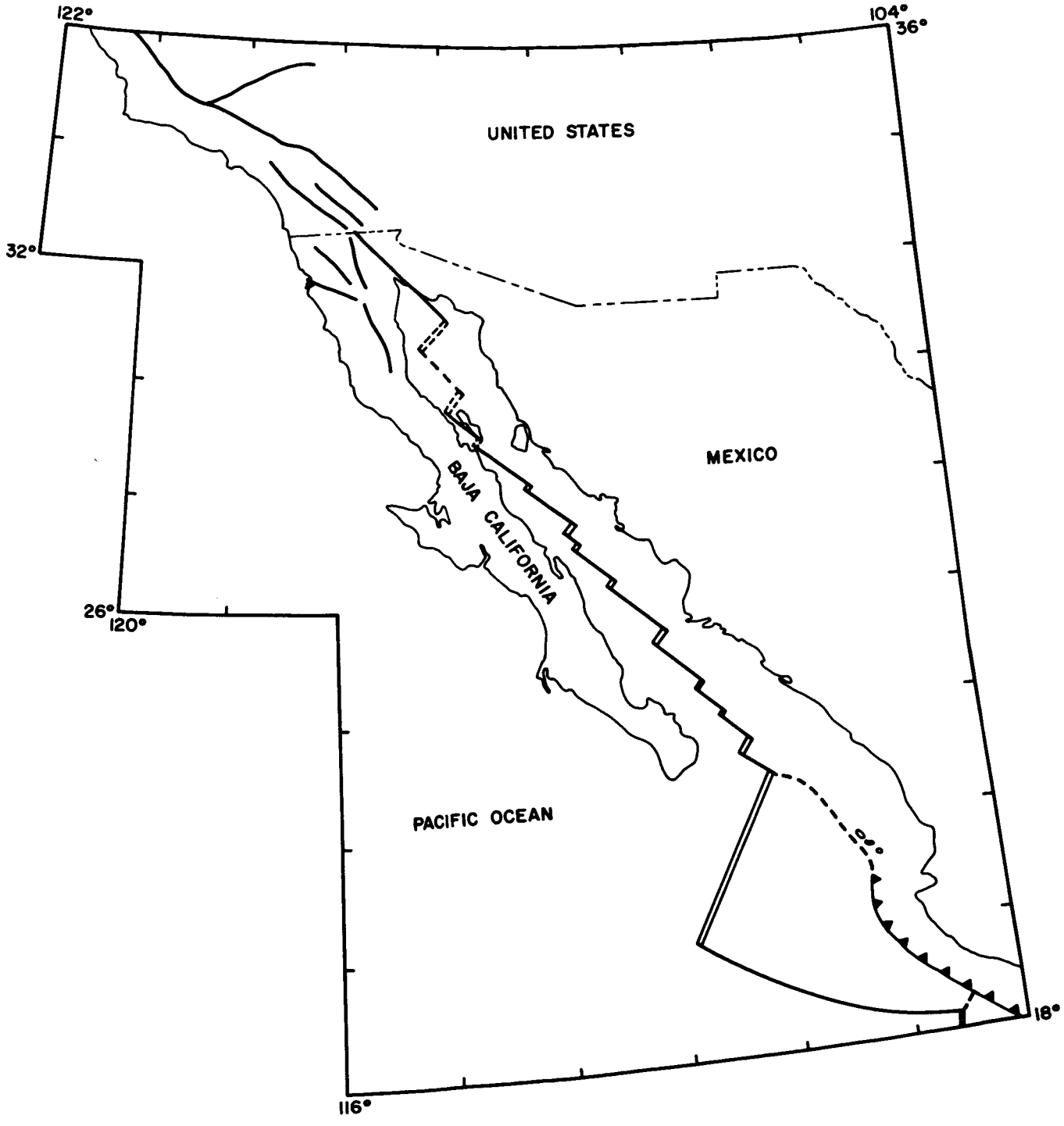
122°
104°
36°
UNITED STATES
32°
MEXICO
BAJA CALIFORNIA
26°
120°
PACIFIC OCEAN
18°
116°

Figure 1

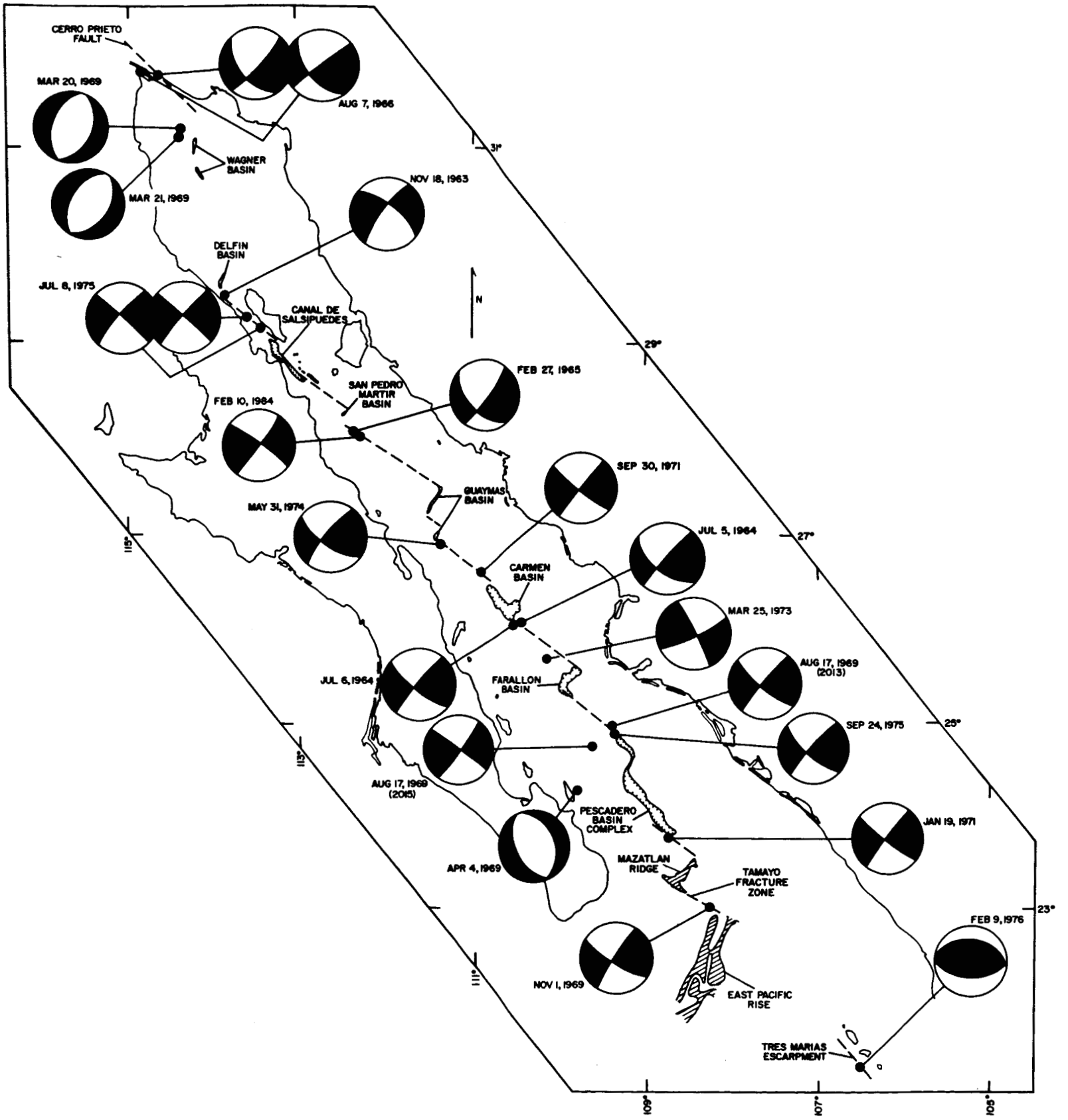
CERRO PRIETO FAULT
MAR 20, 1969
AUG 7, 1966
WAGNER BASIN
MAR 21, 1969
NOV 18, 1963
DELFIN BASIN
JUL 8, 1975
CANAL DE SALSIPUEDES
N
FEB 27, 1965
SAN PEDRO MARTIR BASIN
FEB 10, 1964
SEP 30, 1971
GUAYMAS BASIN
MAY 31, 1974
JUL 5, 1964
CARMEN BASIN
MAR 25, 1973
AUG 17, 1969 (2013)
JUL 6, 1964
FARALLON BASIN
SEP 24, 1975
AUG 17, 1969 (2015)
PESCADERO BASIN COMPLEX
JAN 19, 1971
APR 4, 1969
MAZATLAN RIDGE
TAMAYO FRACTURE ZONE
FEB 9, 1976
NOV 1, 1969
EAST PACIFIC RISE
TRES MARIAS ESCARPMENT
31°
29°
27°
25°
23°
115°
113°
111°
109°
107°
105°

Figure 2

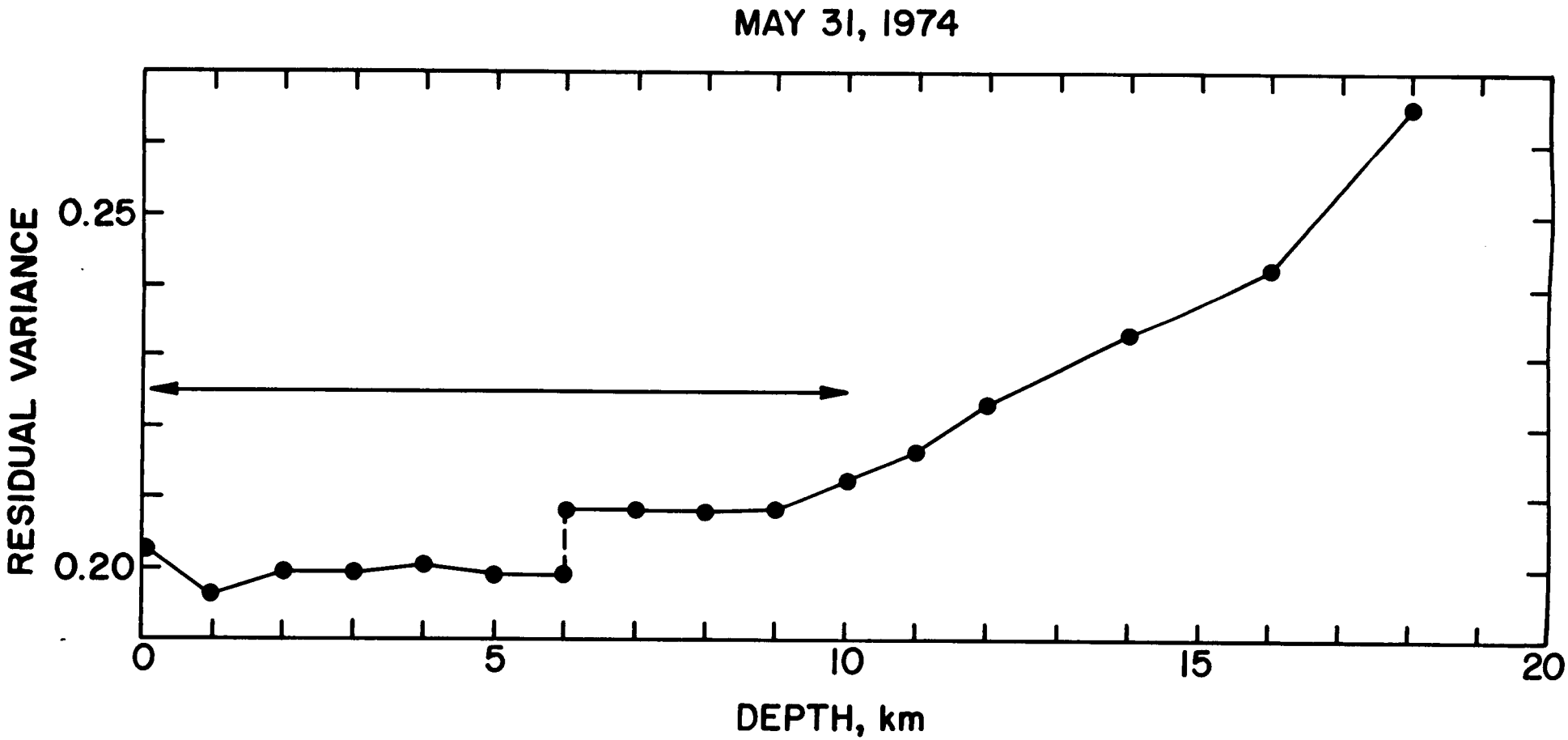

Figure 3

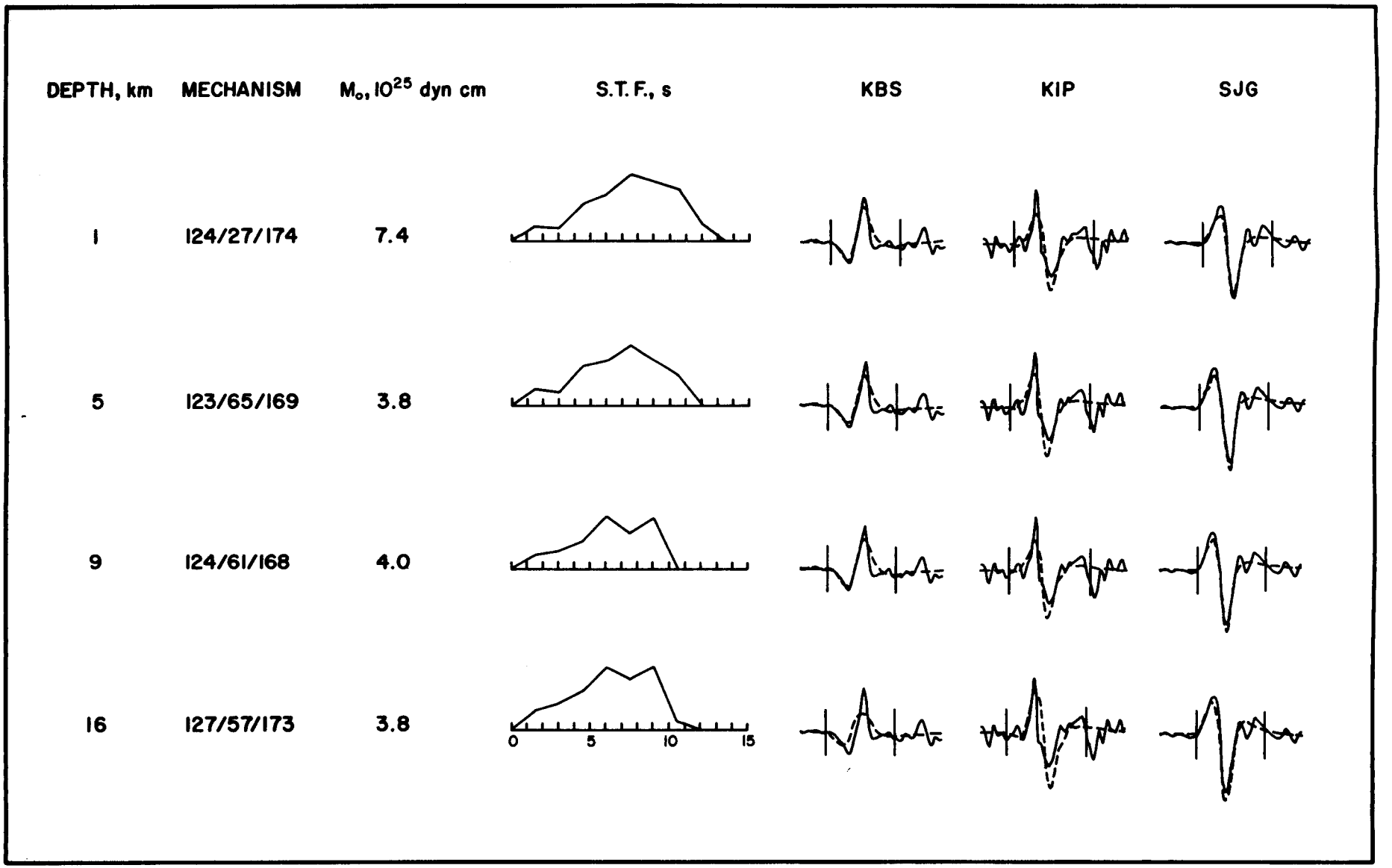
DEPTH, km
MECHANISM
M_o, 10^{25} dyn cm
S.T.F., s
KBS
KIP
SJG
1
124/27/174
7.4
5
123/65/169
3.8
9
124/61/168
4.0
16
127/57/173
3.8
0
5
10
15

Figure 4

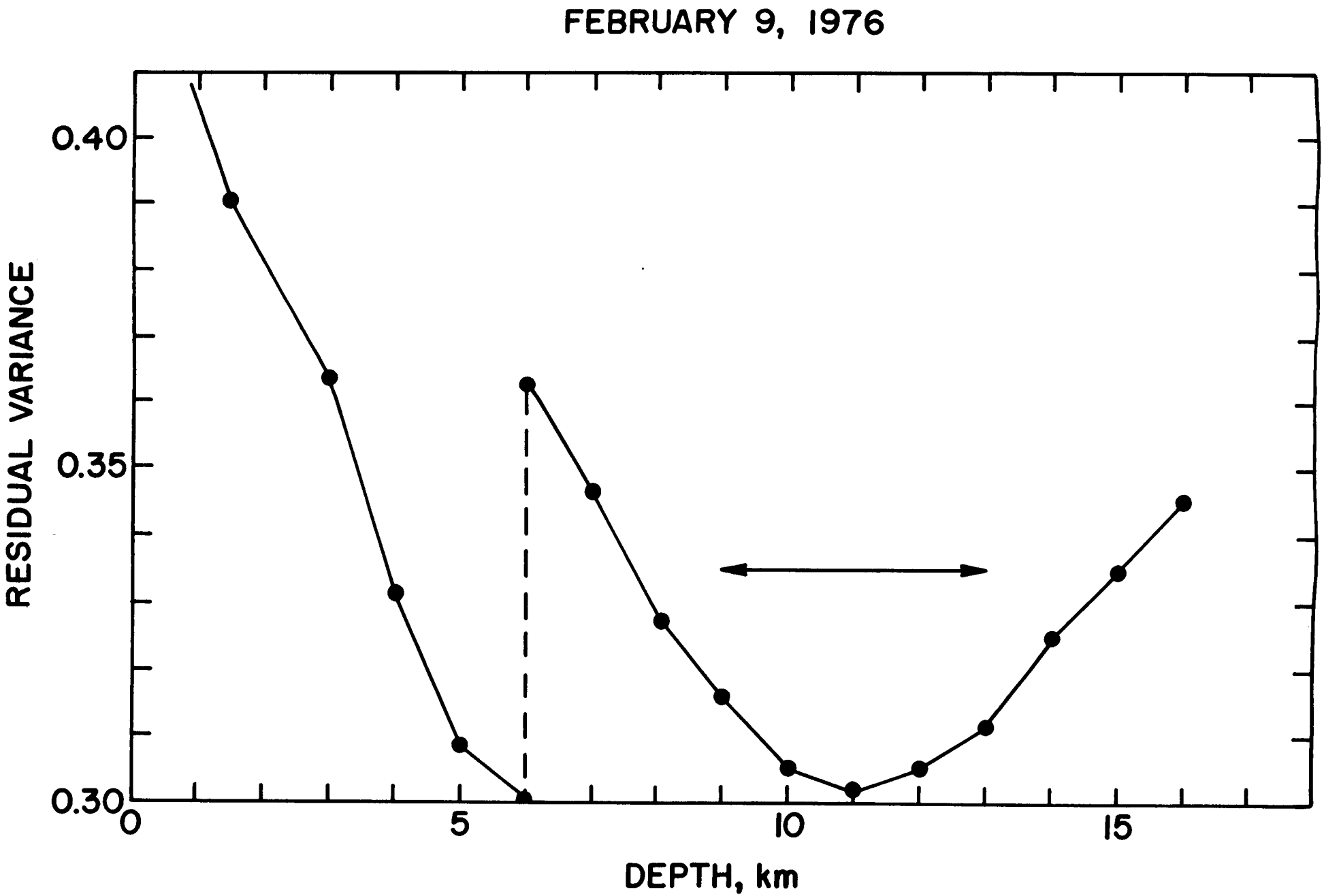
FEBRUARY 9, 1976
RESIDUAL VARIANCE
0.40
0.35
0.30
0
5
10
15
DEPTH, km

Figure 5

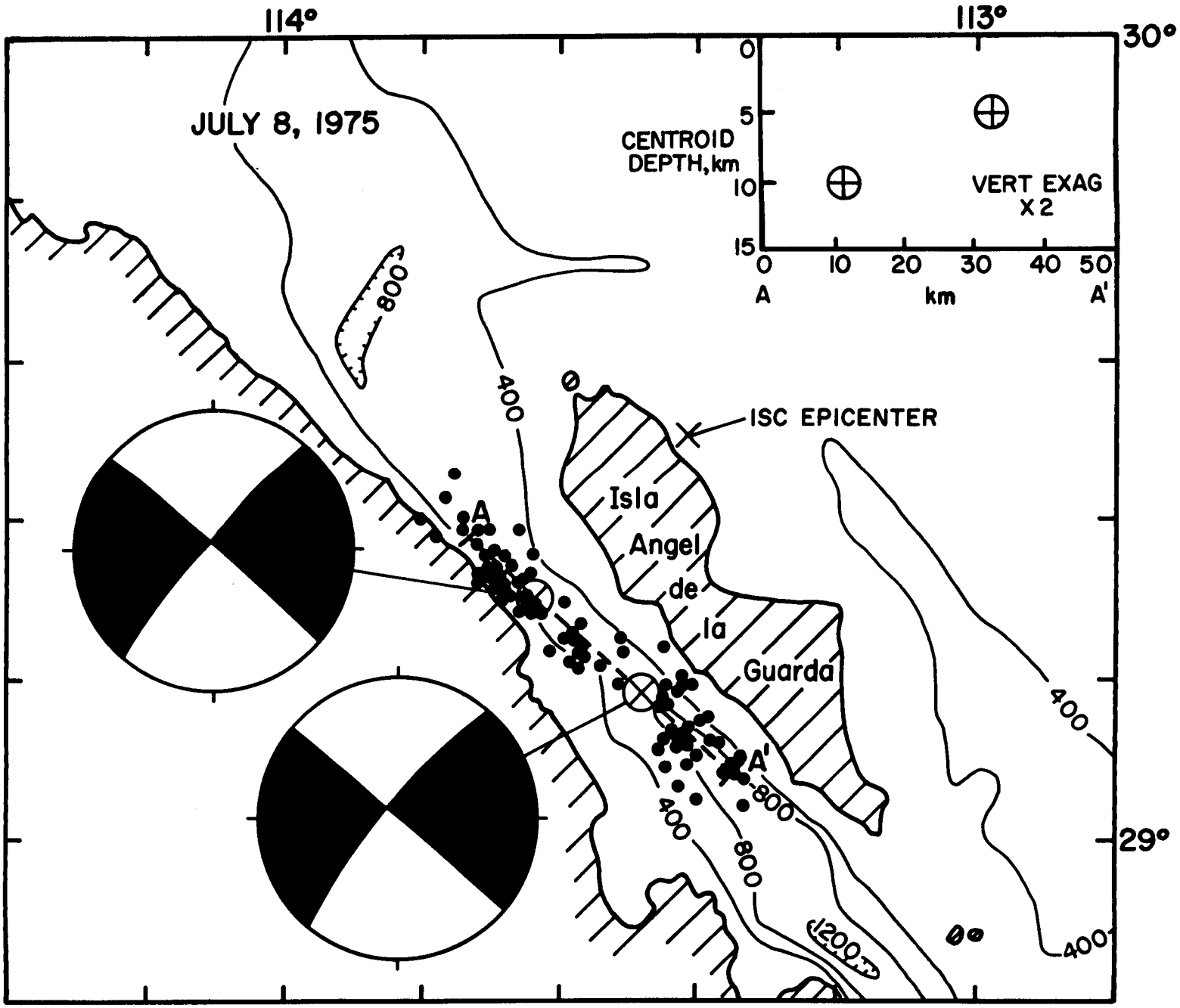
114°
113°
30°
29°
JULY 8, 1975
CENTROID DEPTH, km
0
5
10
15
VERT EXAG X2
0
10
20
30
40
50
A
km
A'
800
400
0
ISC EPICENTER
Isla Angel de la Guarda
A
A'
400
800
400
800
1200
0
400

Figure 6

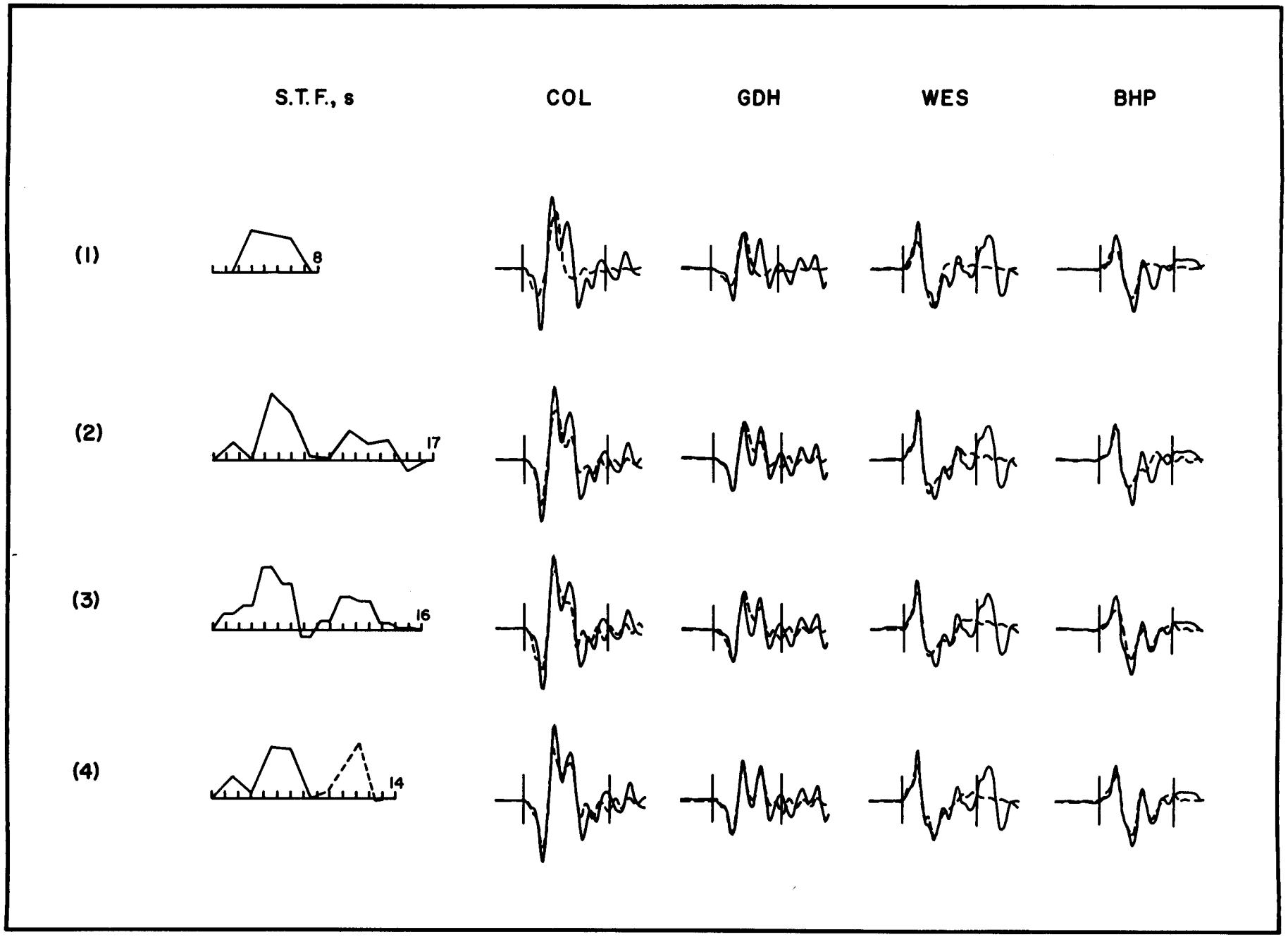

Figure 7

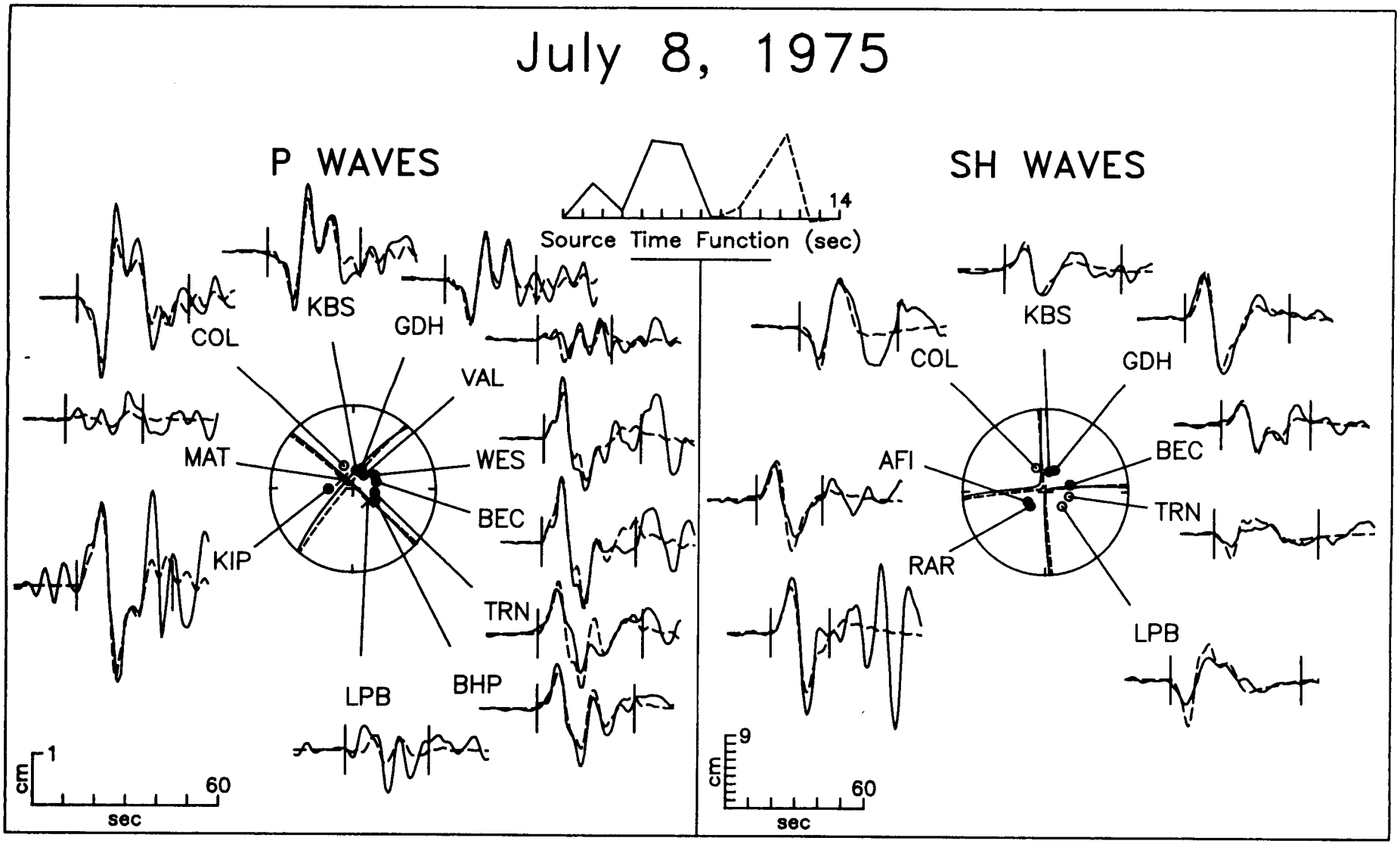
July 8, 1975
P WAVES
SH WAVES
Source Time Function (sec)
14
COL
KBS
GDH
VAL
MAT
WES
BEC
KIP
TRN
LPB
BHP
AFI
RAR
cm
1
60
sec
9

Figure 8

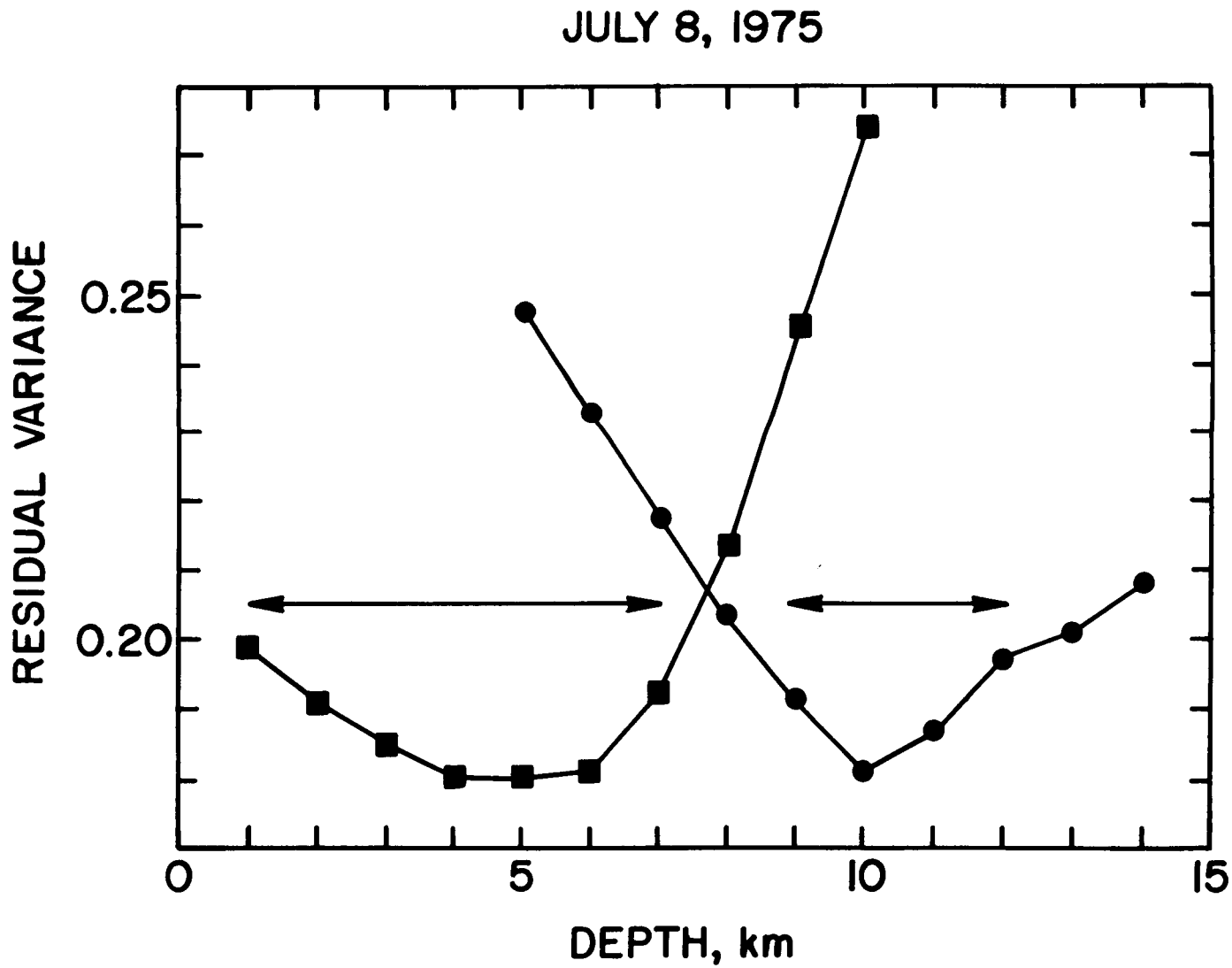

Figure 9

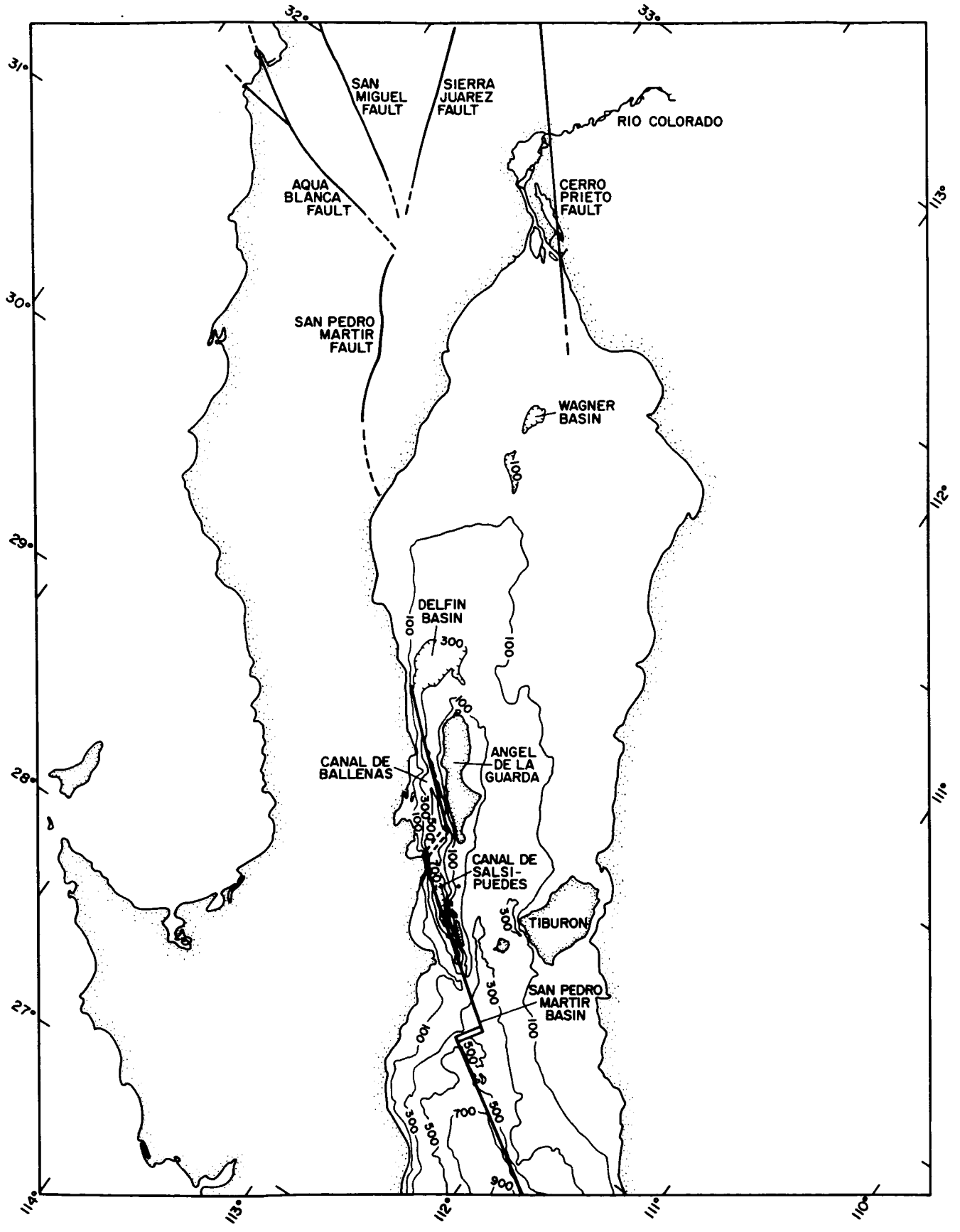
SAN MIGUEL FAULT
SIERRA JUAREZ FAULT
RIO COLORADO
AQUA BLANCA FAULT
CERRO PRIETO FAULT
SAN PEDRO MARTIR FAULT
WAGNER BASIN
DELFIN BASIN
CANAL DE BALLENAS
ANGEL DE LA GUARDA
CANAL DE SALSI-PUEDES
TIBURON
SAN PEDRO MARTIR BASIN
32°
33°
31°
30°
29°
28°
27°
114°
113°
112°
111°
110°

Figure 10

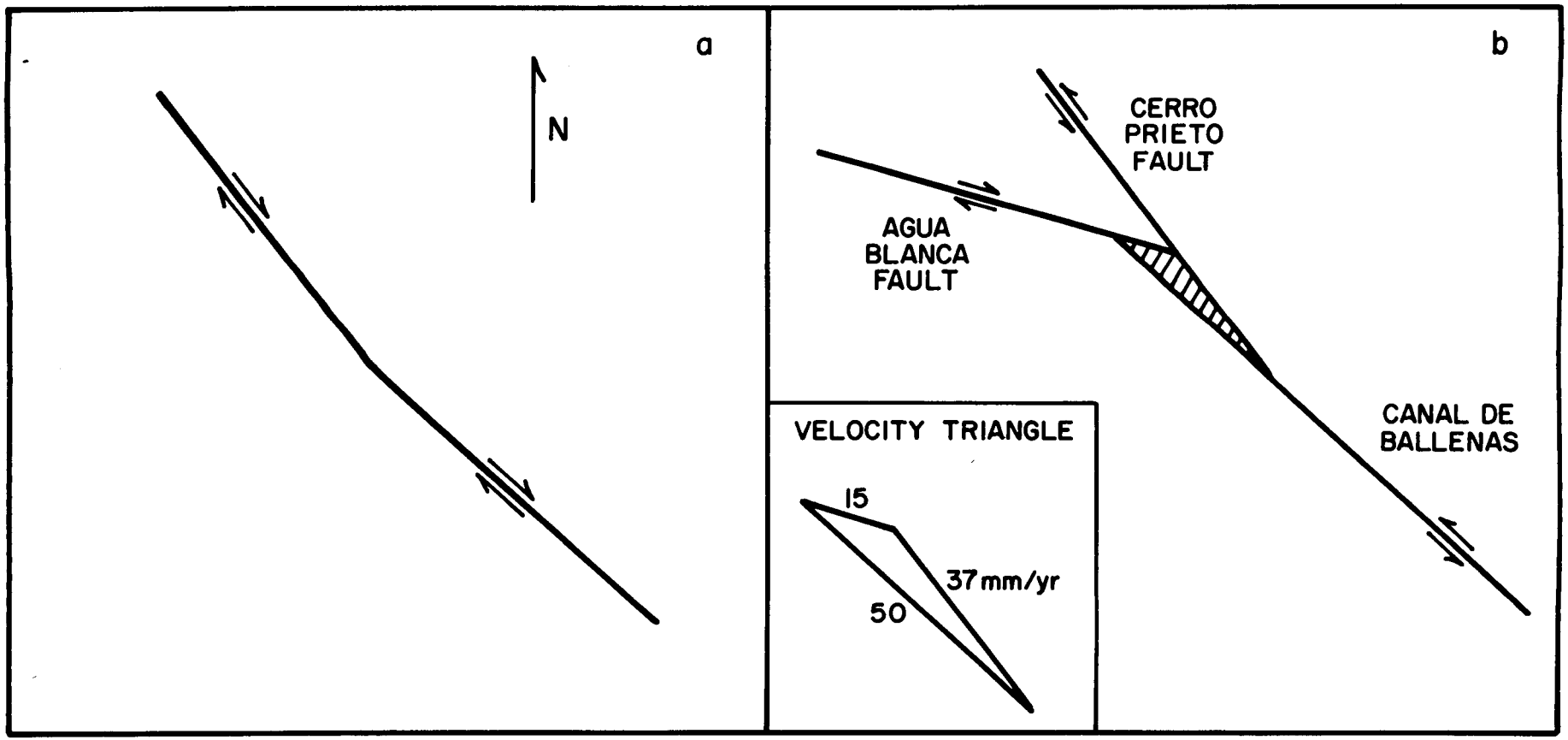
a
N
b
CERRO
PRIETO
FAULT
AGUA
BLANCA
FAULT
CANAL DE
BALLENAS
VELOCITY TRIANGLE
15
37 mm/yr
50

Figure 11

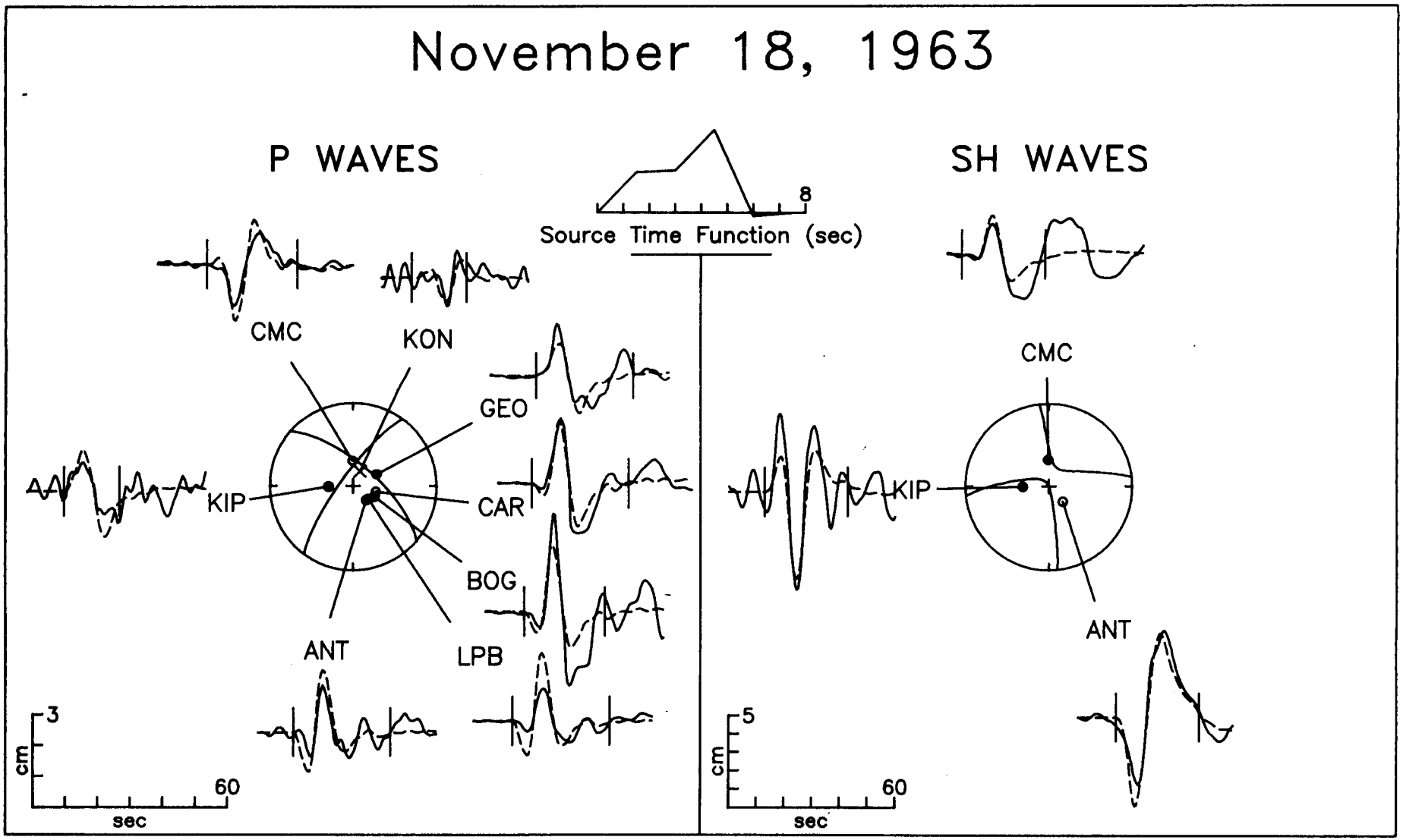
November 18, 1963
P WAVES
SH WAVES
8
Source Time Function (sec)
CMC
KON
GEO
KIP
CAR
BOG
ANT
LPB
3
cm
60
sec
CMC
KIP
ANT
5
cm
60
sec

Figure A1

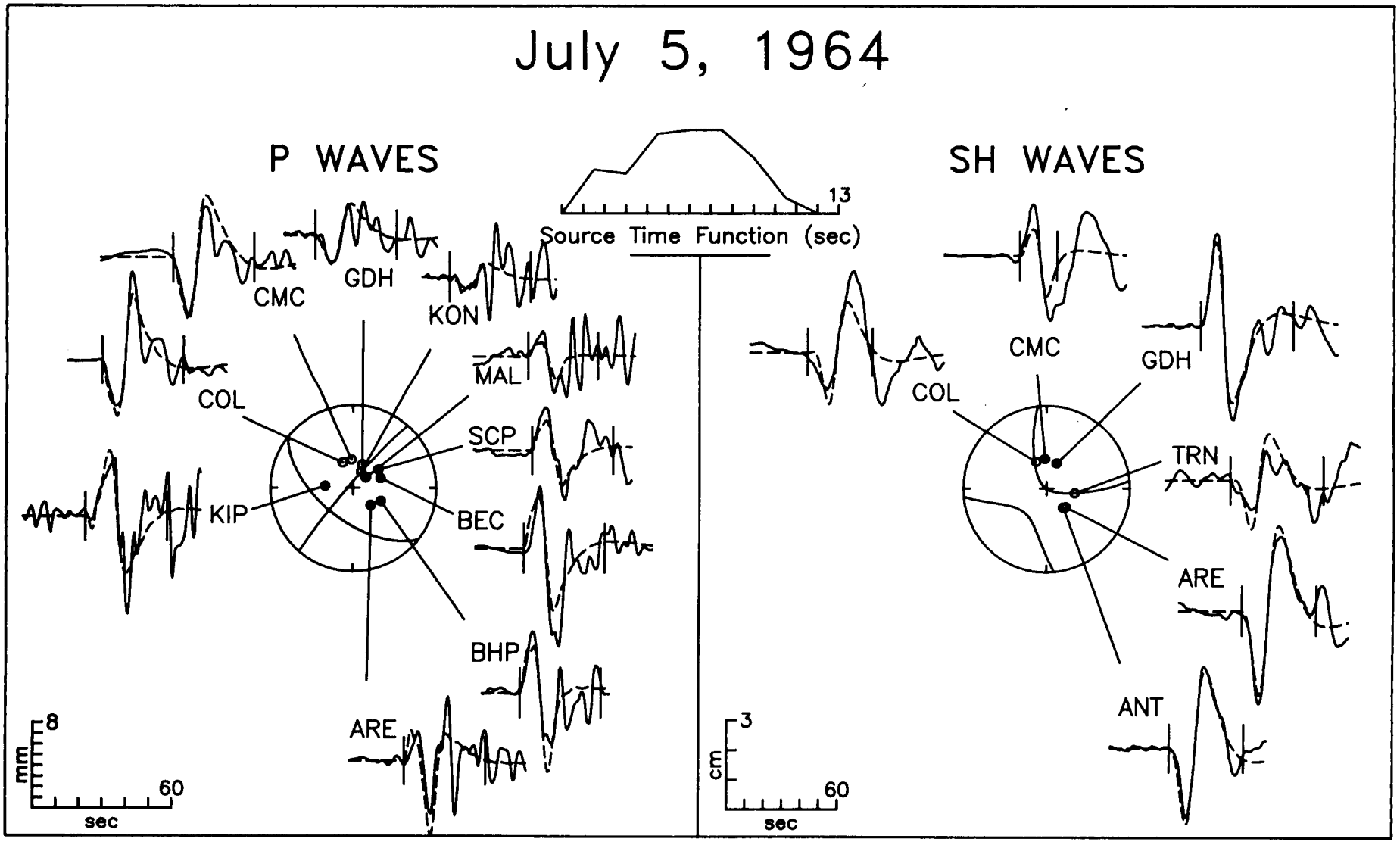
July 5, 1964
P WAVES
SH WAVES
13
Source Time Function (sec)
CMC
GDH
KON
MAL
COL
SCP
KIP
BEC
BHP
ARE
8
mm
60
sec
CMC
GDH
COL
TRN
ARE
ANT
3
cm
60
sec

Figure A2

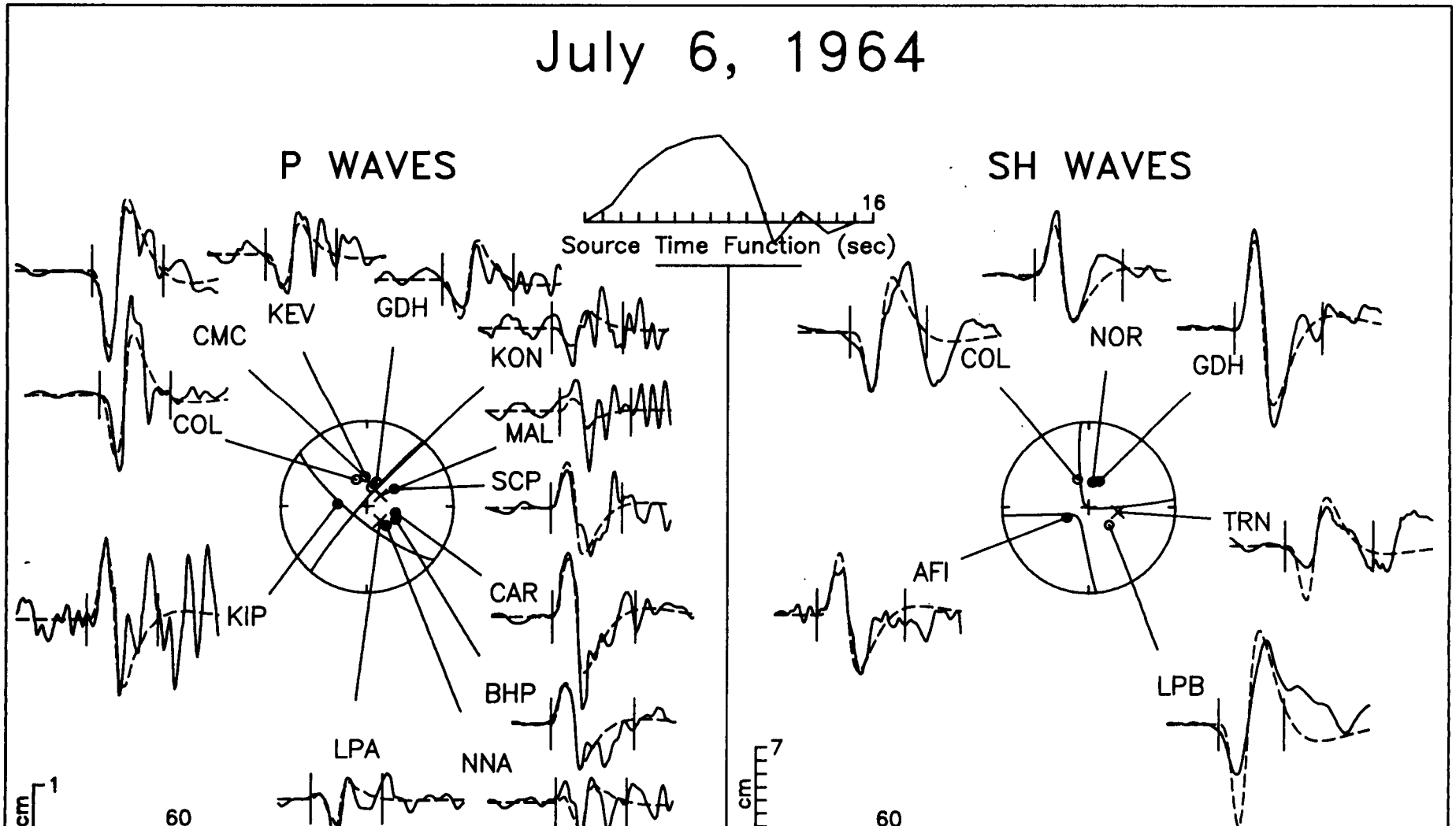
July 6, 1964
P WAVES
SH WAVES
Source Time Function (sec)
16
KEV
GDH
CMC
KON
COL
MAL
SCP
KIP
CAR
BHP
LPA
NNA
cm
1
60
sec
NOR
COL
GDH
TRN
AFI
LPB
7
60
sec

Figure A3

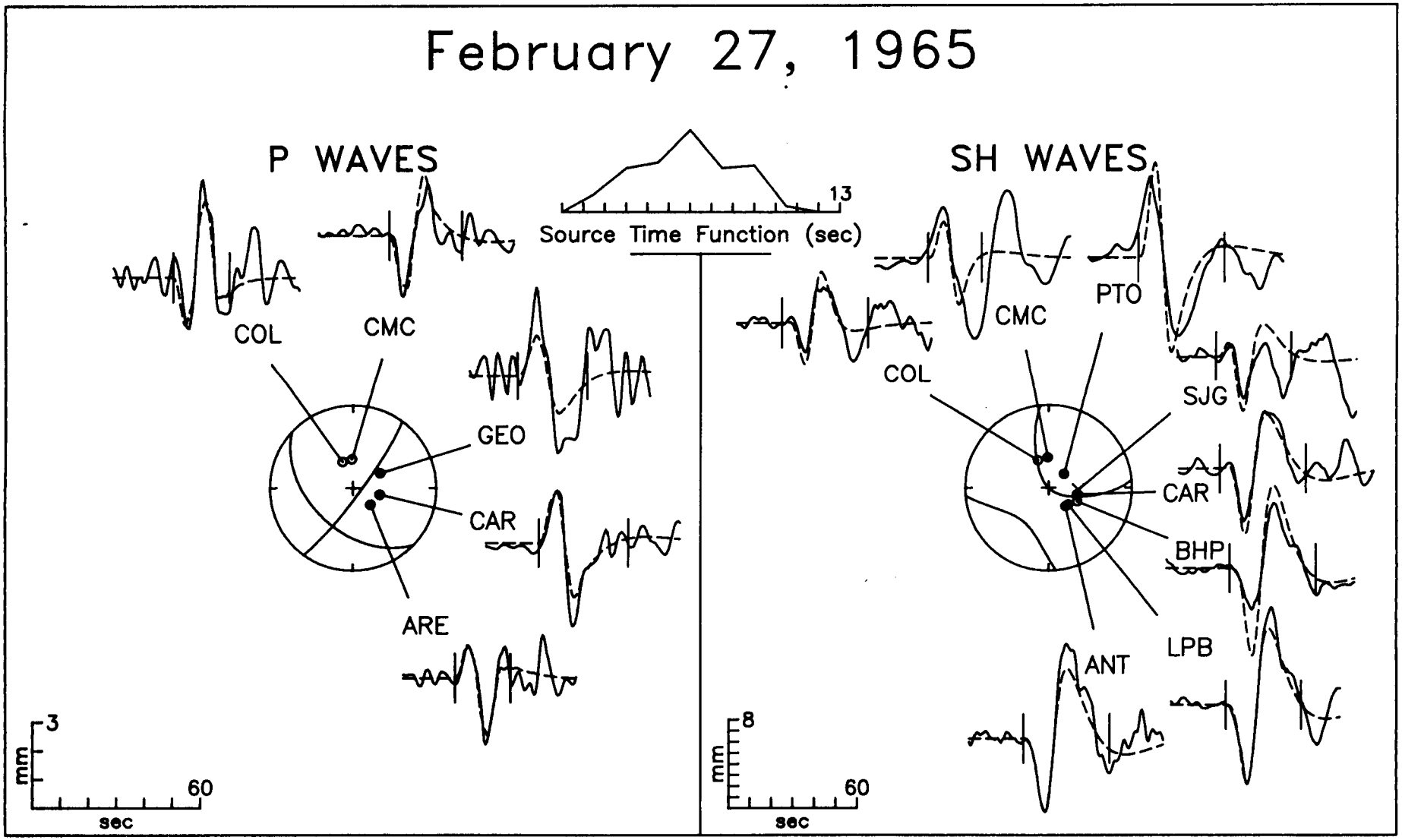
February 27, 1965
P WAVES
SH WAVES
13
Source Time Function (sec)
COL
CMC
GEO
CAR
ARE
PTO
SJG
BHP
LPB
ANT
3
mm
60
sec
8
mm
60
sec

Figure A4

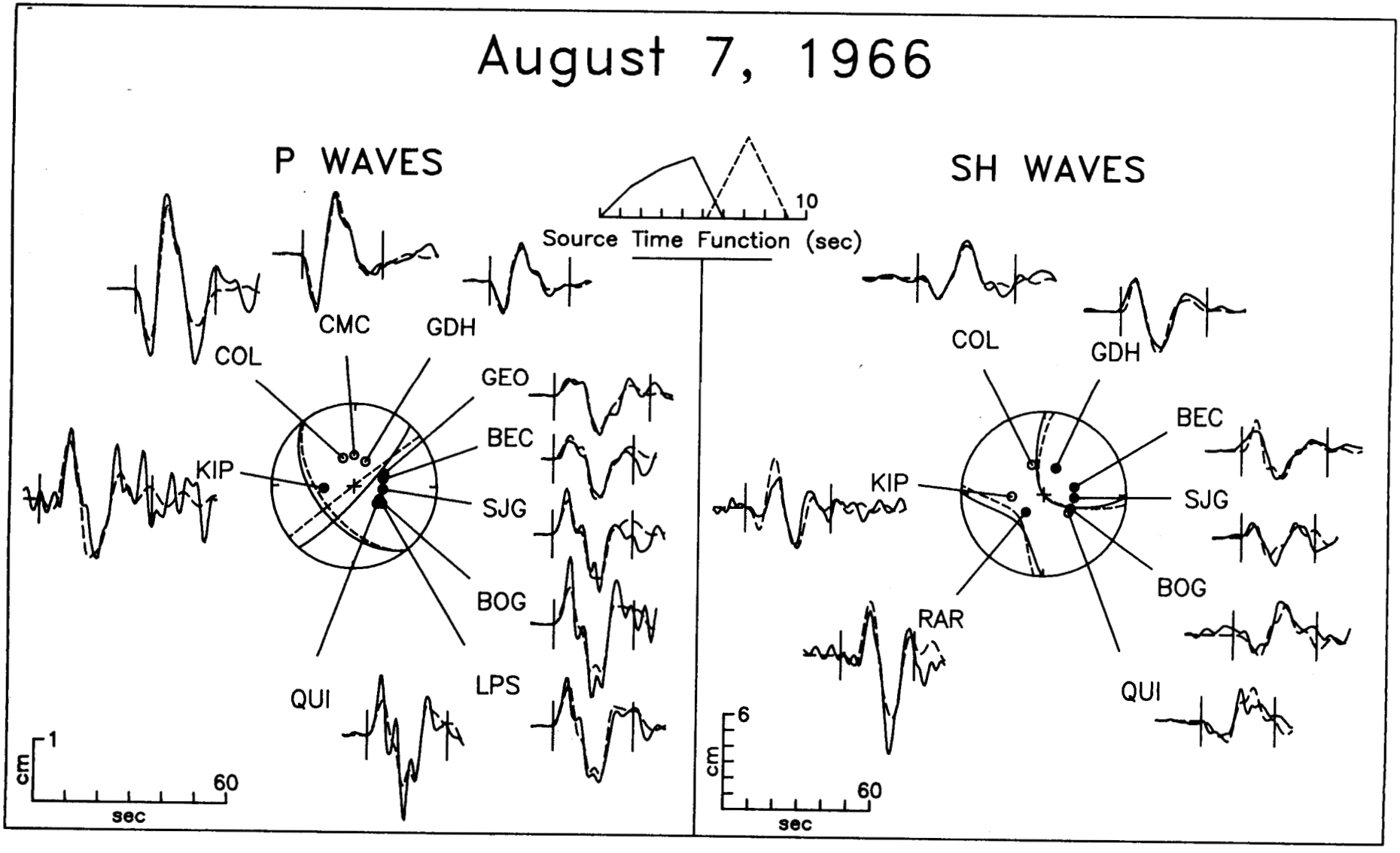
August 7, 1966
P WAVES
SH WAVES
Source Time Function (sec)
10
CMC
GDH
COL
GEO
BEC
KIP
SJG
BOG
LPS
QUI
RAR
1
60
sec
cm
6

Figure A5

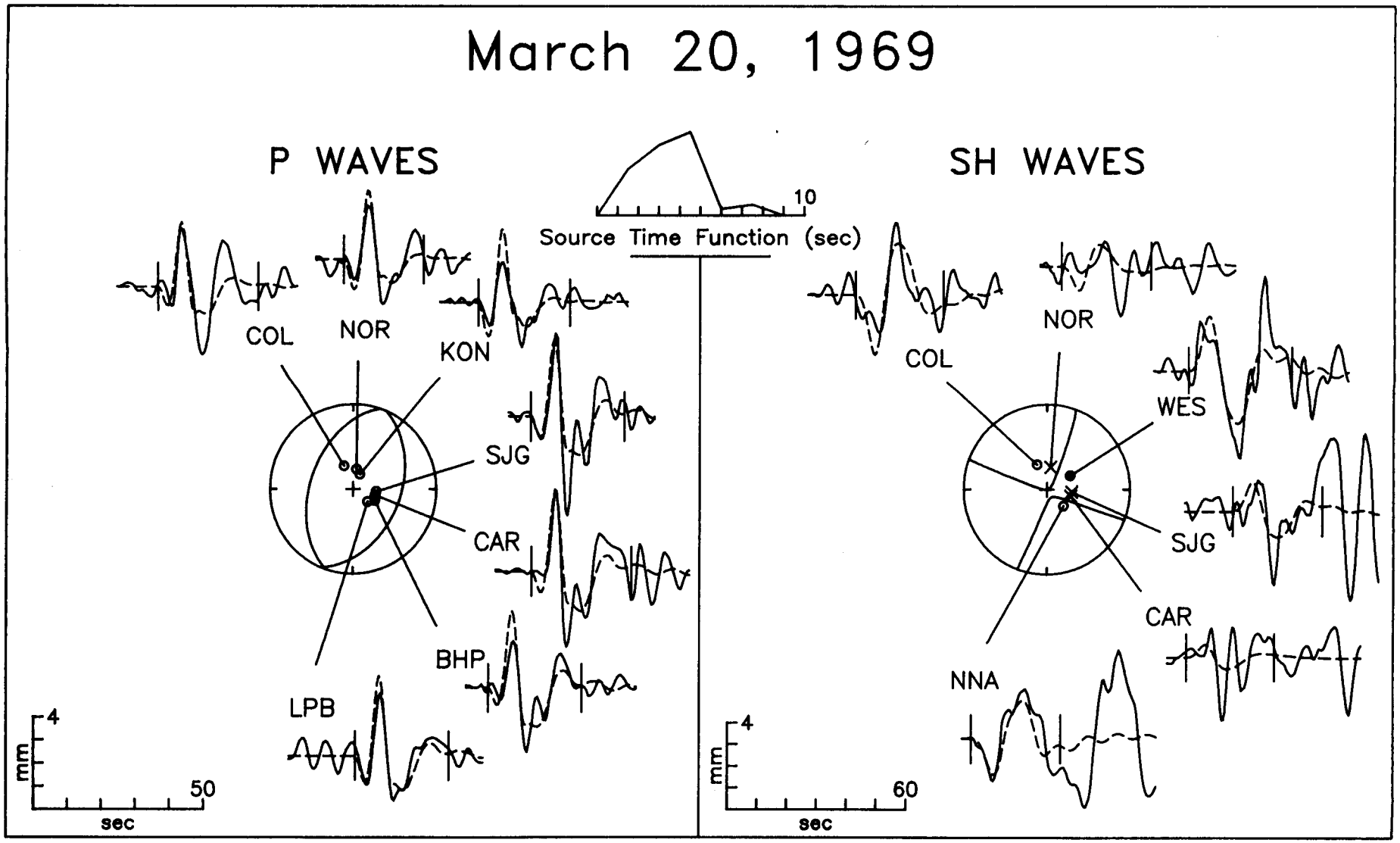
March 20, 1969
P WAVES
SH WAVES
10
Source Time Function (sec)
COL
NOR
KON
SJG
CAR
BHP
LPB
WES
NNA
4
mm
50
60
sec

Figure A6

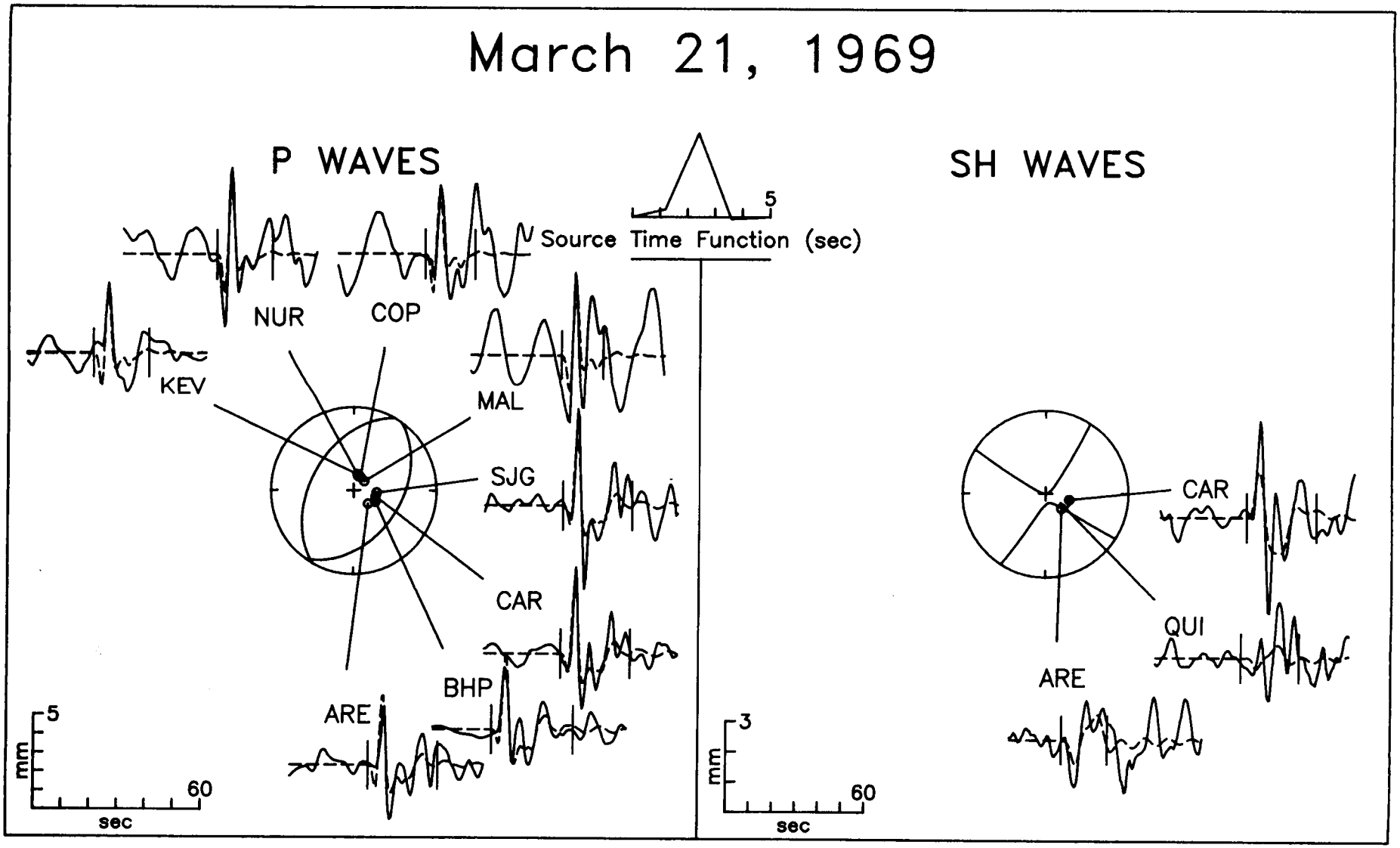
March 21, 1969
P WAVES
SH WAVES
5
Source Time Function (sec)
NUR
COP
KEV
MAL
SJG
CAR
BHP
ARE
5
mm
60
sec
3
mm
60
sec
CAR
QUI
ARE

Figure A7

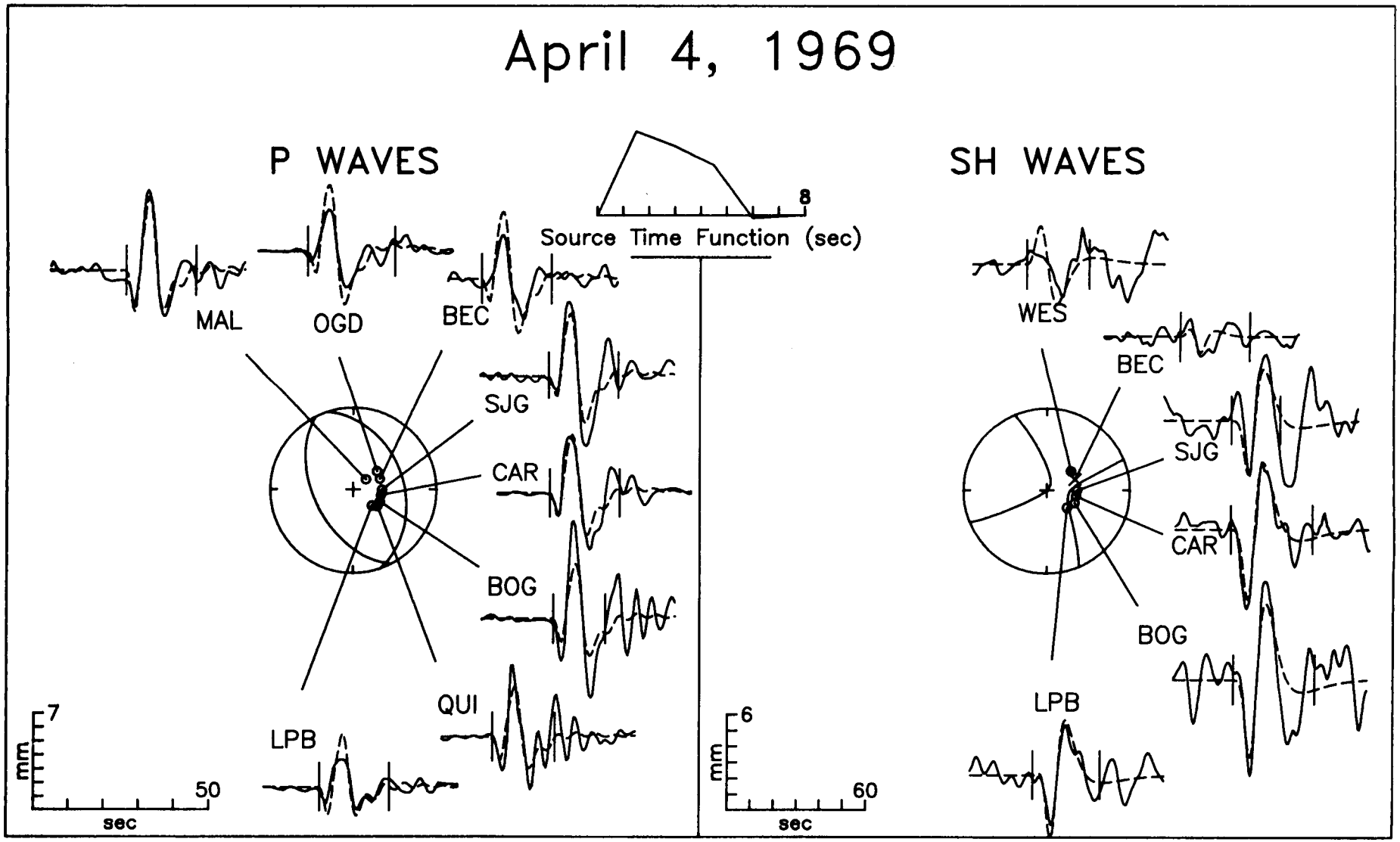
April 4, 1969
P WAVES
SH WAVES
Source Time Function (sec)
8
MAL
OGD
BEC
SJG
CAR
BOG
QUI
LPB
WES
7
mm
50
sec
6
60

Figure A8

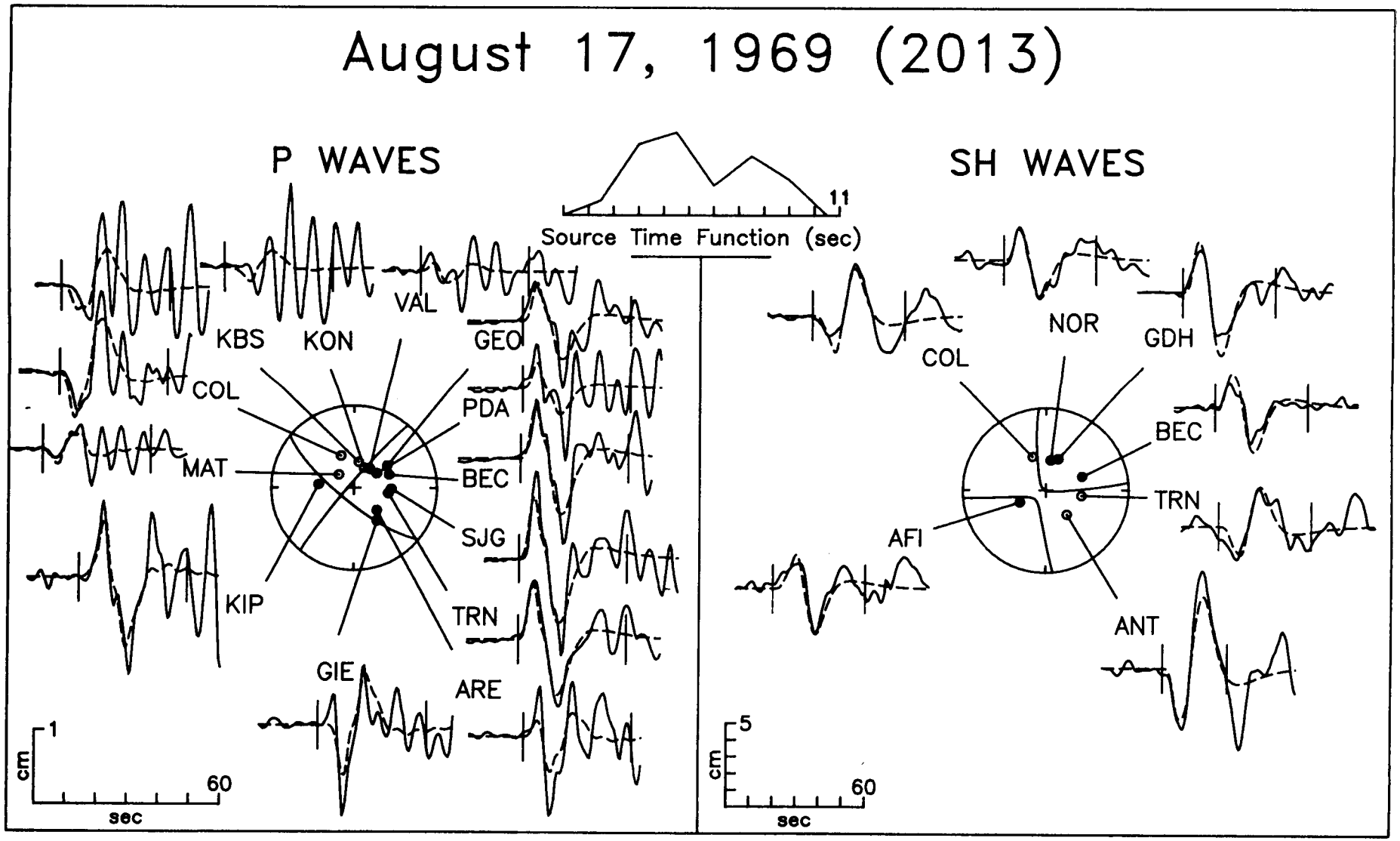
August 17, 1969 (2013)
P WAVES
SH WAVES
Source Time Function (sec)
11
KBS
KON
VAL
GEO
COL
PDA
MAT
BEC
SJG
KIP
TRN
GIE
ARE
NOR
GDH
COL
BEC
TRN
AFI
ANT
1
60
cm
sec
5
60
cm
sec

Figure A9

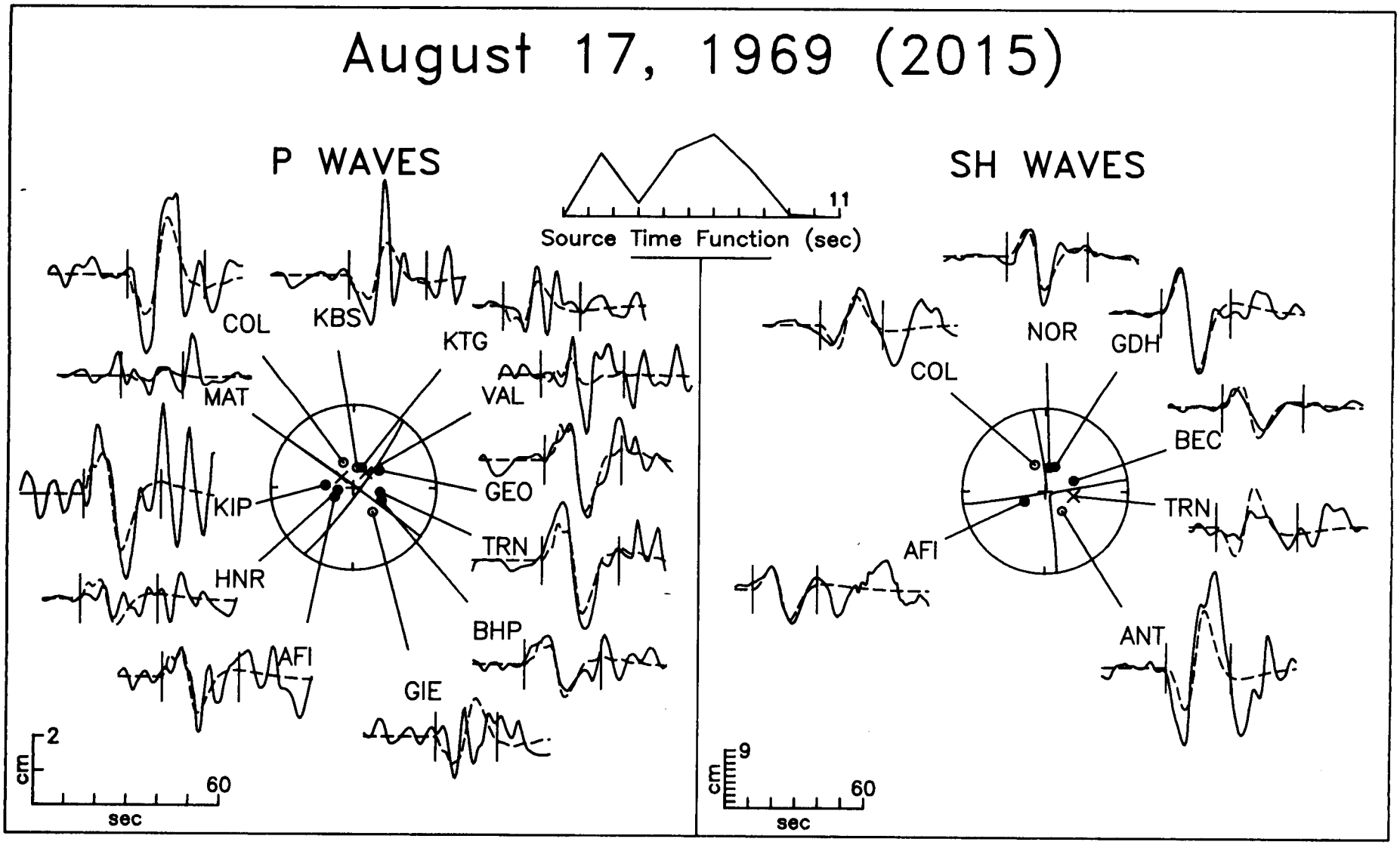
August 17, 1969 (2015)
P WAVES
SH WAVES
Source Time Function (sec)
11
COL
KBS
KTG
MAT
VAL
KIP
GEO
TRN
HNR
BHP
AFI
GIE
2
cm
60
sec
NOR
GDH
COL
BEC
TRN
AFI
ANT
9
cm
60
sec

Figure A10

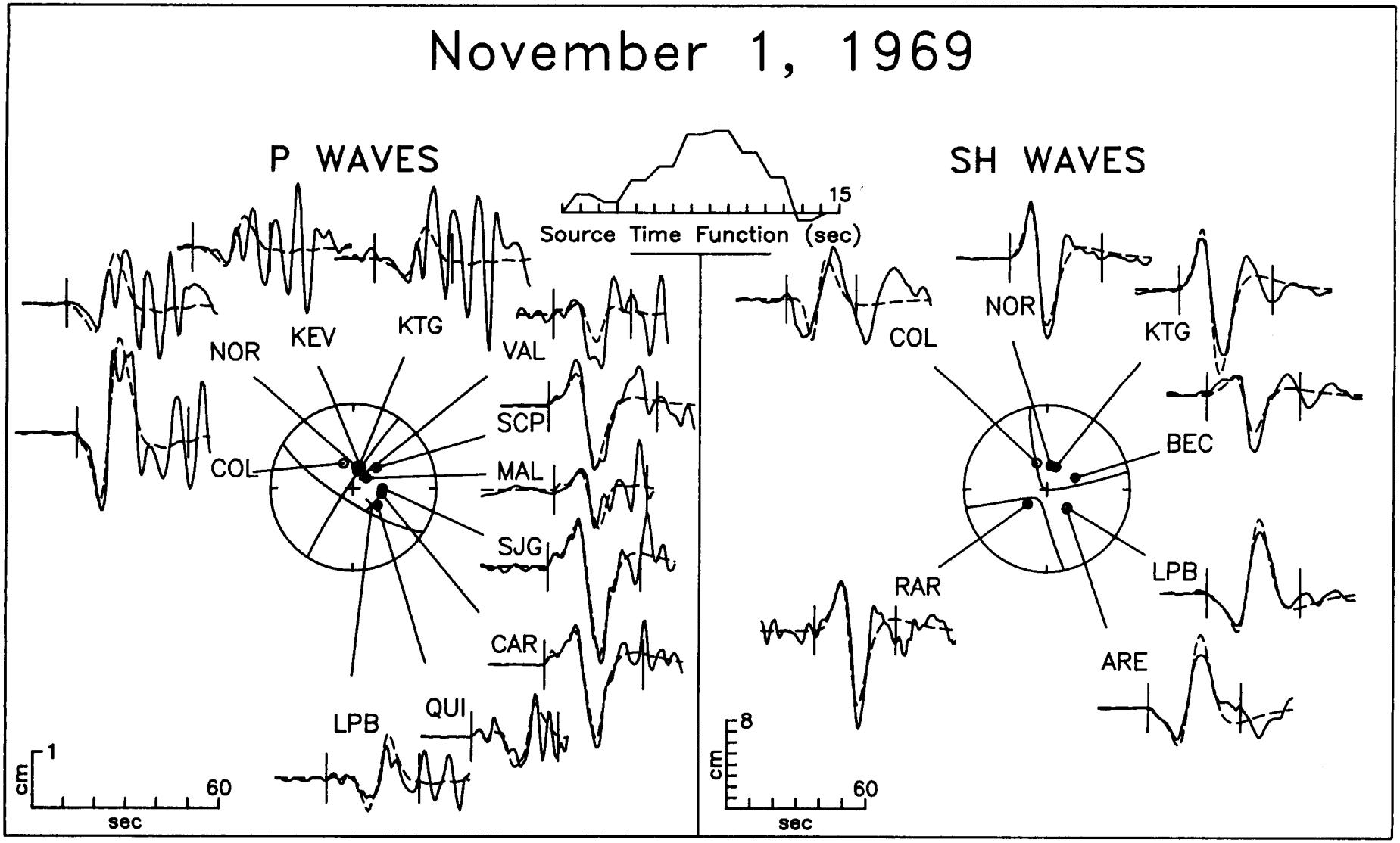
November 1, 1969
P WAVES
SH WAVES
Source Time Function (sec)
15
NOR
KEV
KTG
VAL
COL
SCP
MAL
SJG
CAR
LPB
QUI
1
60
sec
cm
NOR
KTG
COL
BEC
RAR
LPB
ARE
8
60
sec
cm

Figure A11

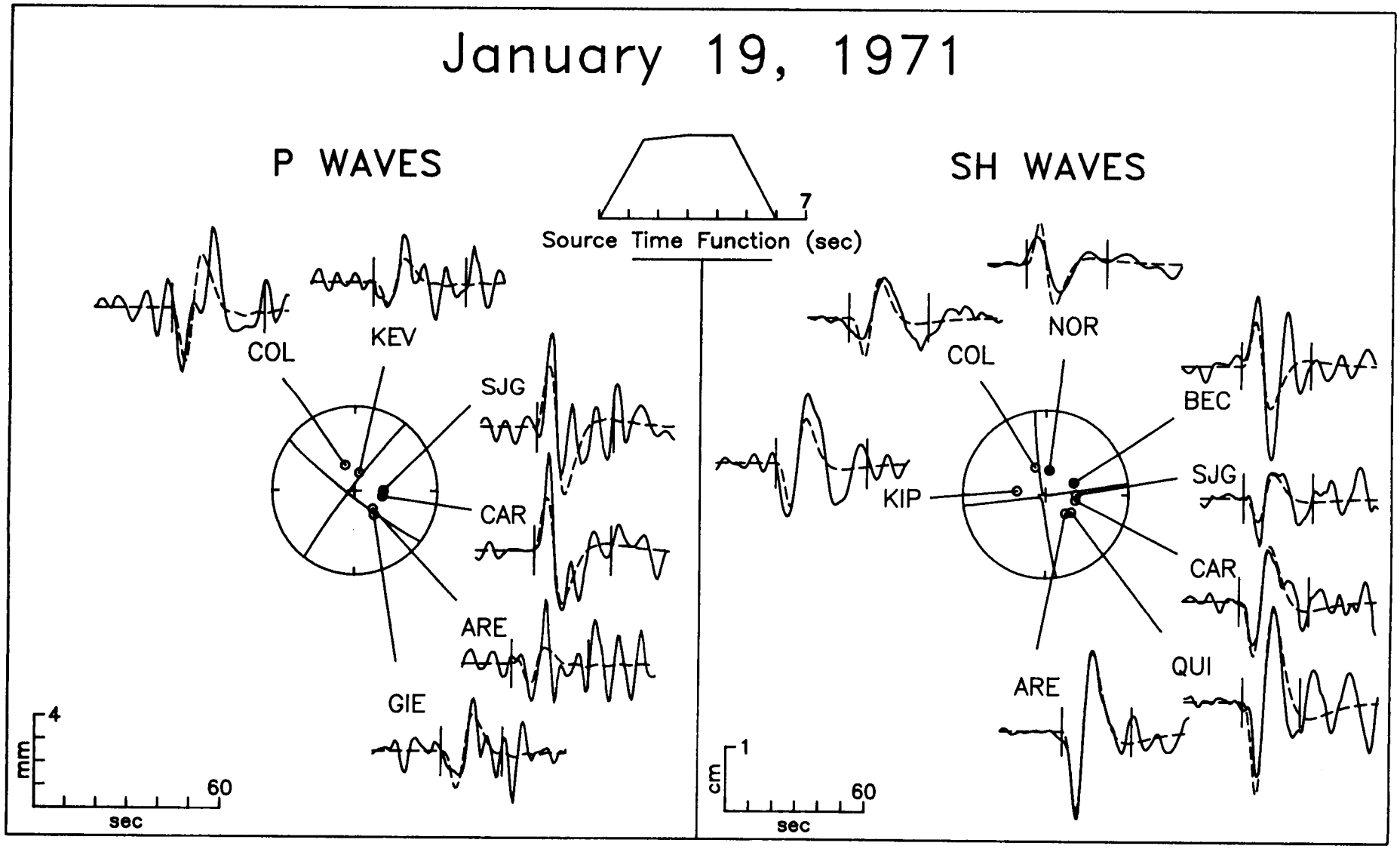
January 19, 1971
P WAVES
SH WAVES
Source Time Function (sec)
7
COL
KEV
SJG
CAR
ARE
GIE
NOR
KIP
BEC
QUI
4
mm
60
sec
1
cm
60
sec

Figure A12

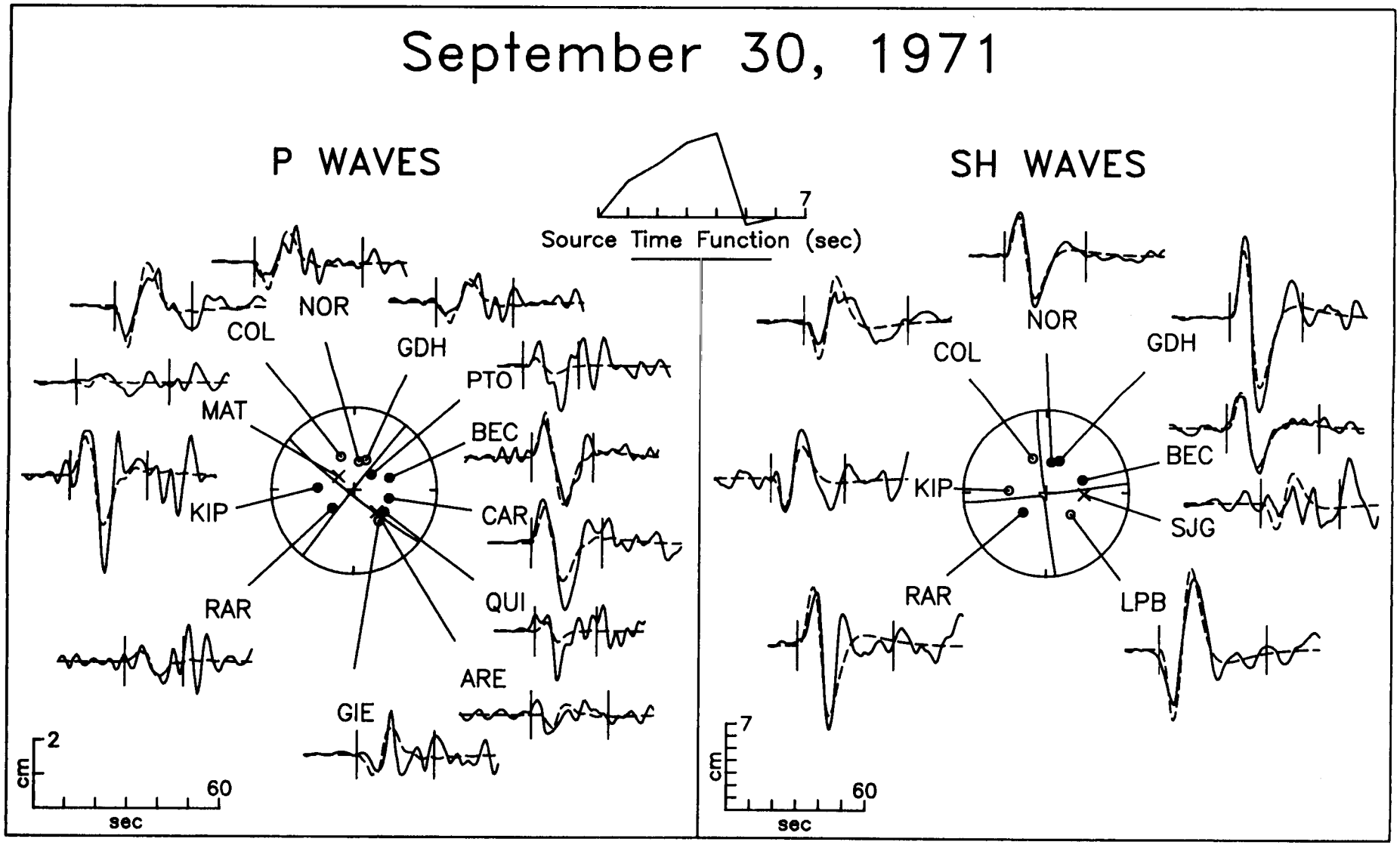
September 30, 1971
P WAVES
SH WAVES
Source Time Function (sec)
7
COL
NOR
GDH
PTO
MAT
BEC
KIP
CAR
RAR
QUI
ARE
GIE
LPB
SJG
2
cm
60
sec
7
cm
60
sec

Figure A13

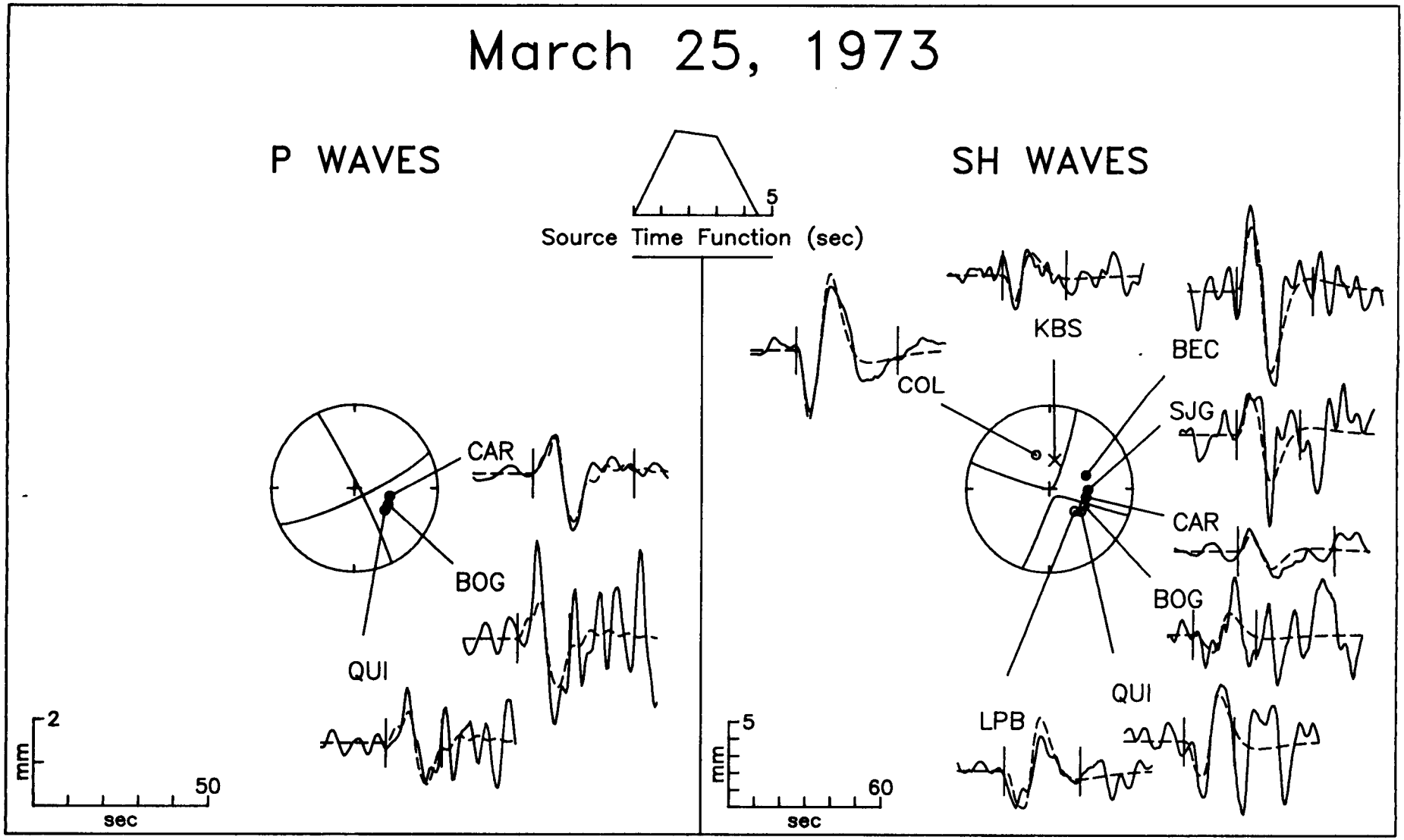
March 25, 1973
P WAVES
SH WAVES
5
Source Time Function (sec)
CAR
BOG
QUI
2
mm
50
sec
KBS
COL
BEC
SJG
CAR
BOG
QUI
LPB
5
mm
60
sec

Figure A14

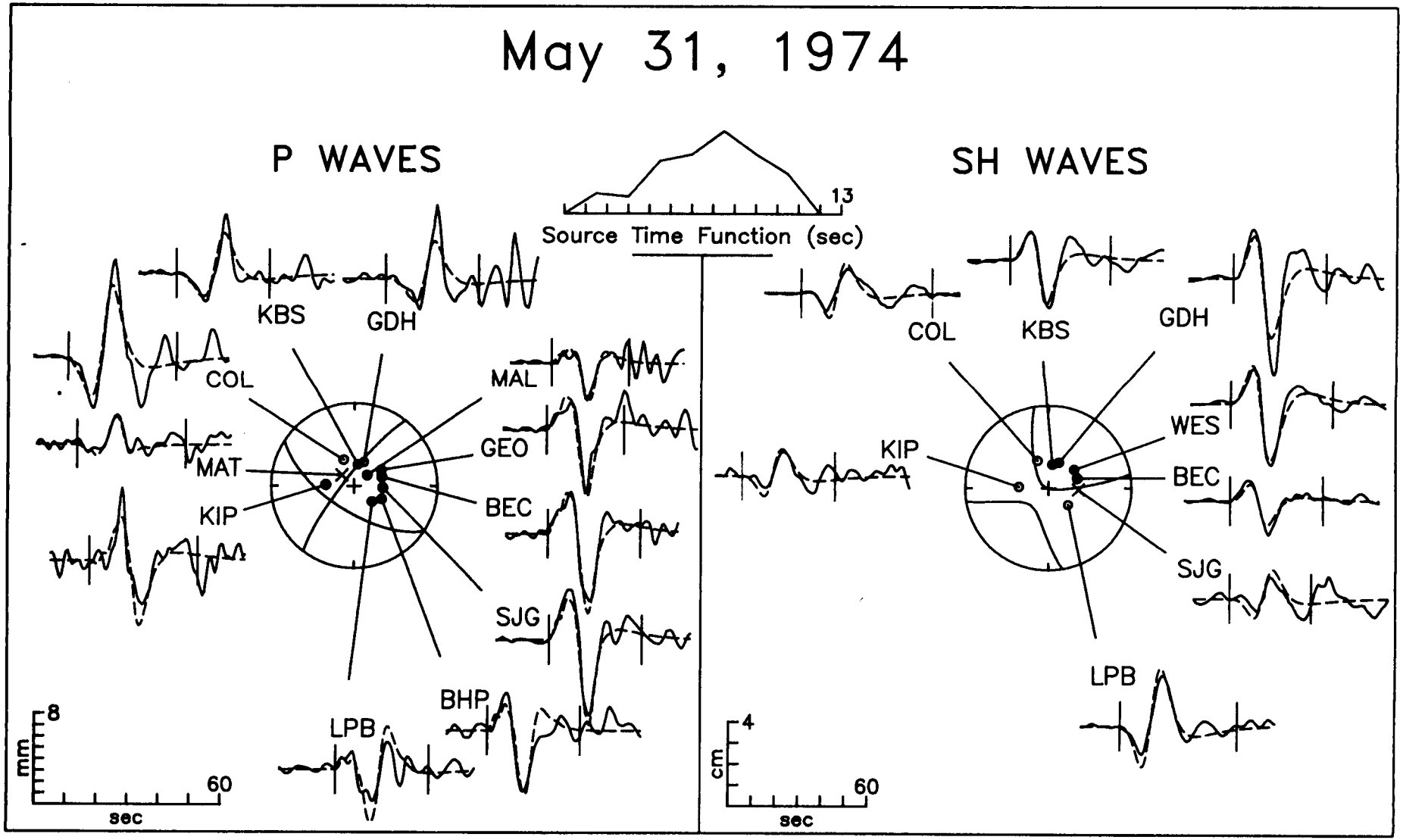
May 31, 1974
P WAVES
SH WAVES
13
Source Time Function (sec)
KBS
GDH
COL
MAL
MAT
GEO
KIP
BEC
SJG
BHP
LPB
8
mm
60
sec
COL
KBS
GDH
KIP
WES
BEC
SJG
LPB
4
cm
60
sec

Figure A15

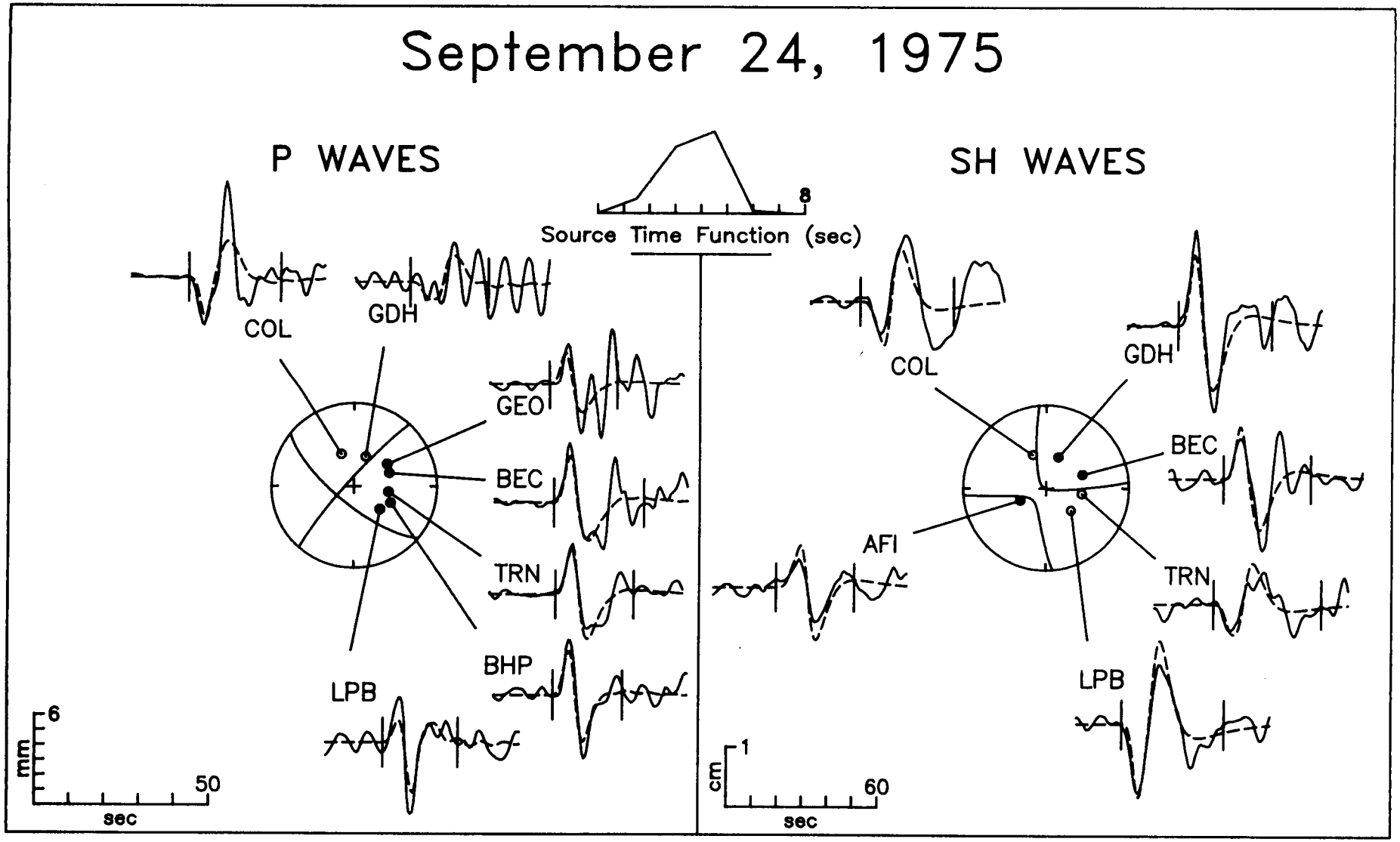
September 24, 1975
P WAVES
SH WAVES
Source Time Function (sec)
8
COL
GDH
GEO
BEC
TRN
BHP
LPB
AFI
6
mm
50
sec
1
cm
60
sec

Figure A16

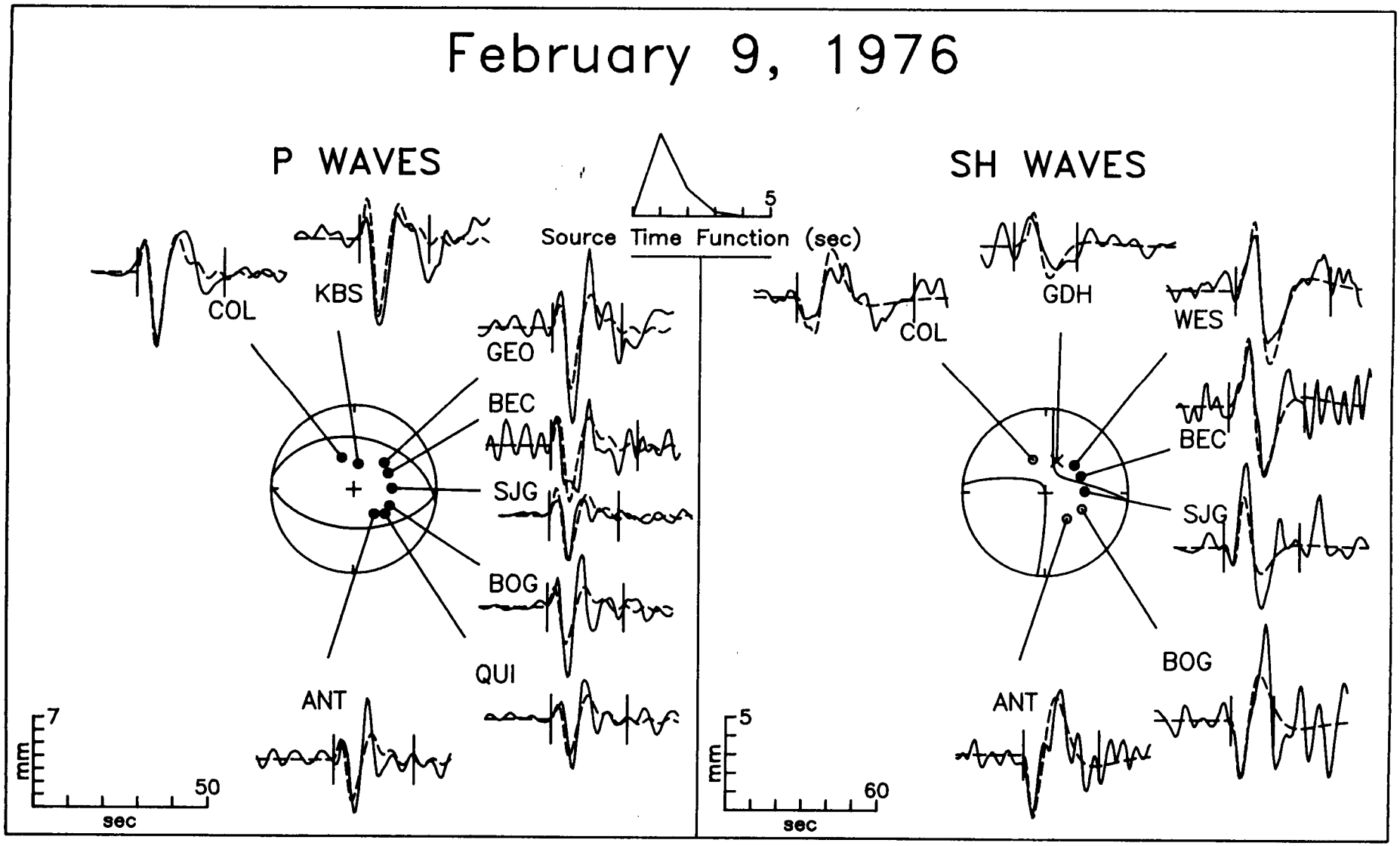
February 9, 1976
P WAVES
SH WAVES
Source Time Function (sec)
5
COL
KBS
GEO
BEC
SJG
BOG
QUI
ANT
7
mm
50
sec
COL
GDH
WES
BEC
SJG
BOG
ANT
5
mm
60
sec

Figure A17

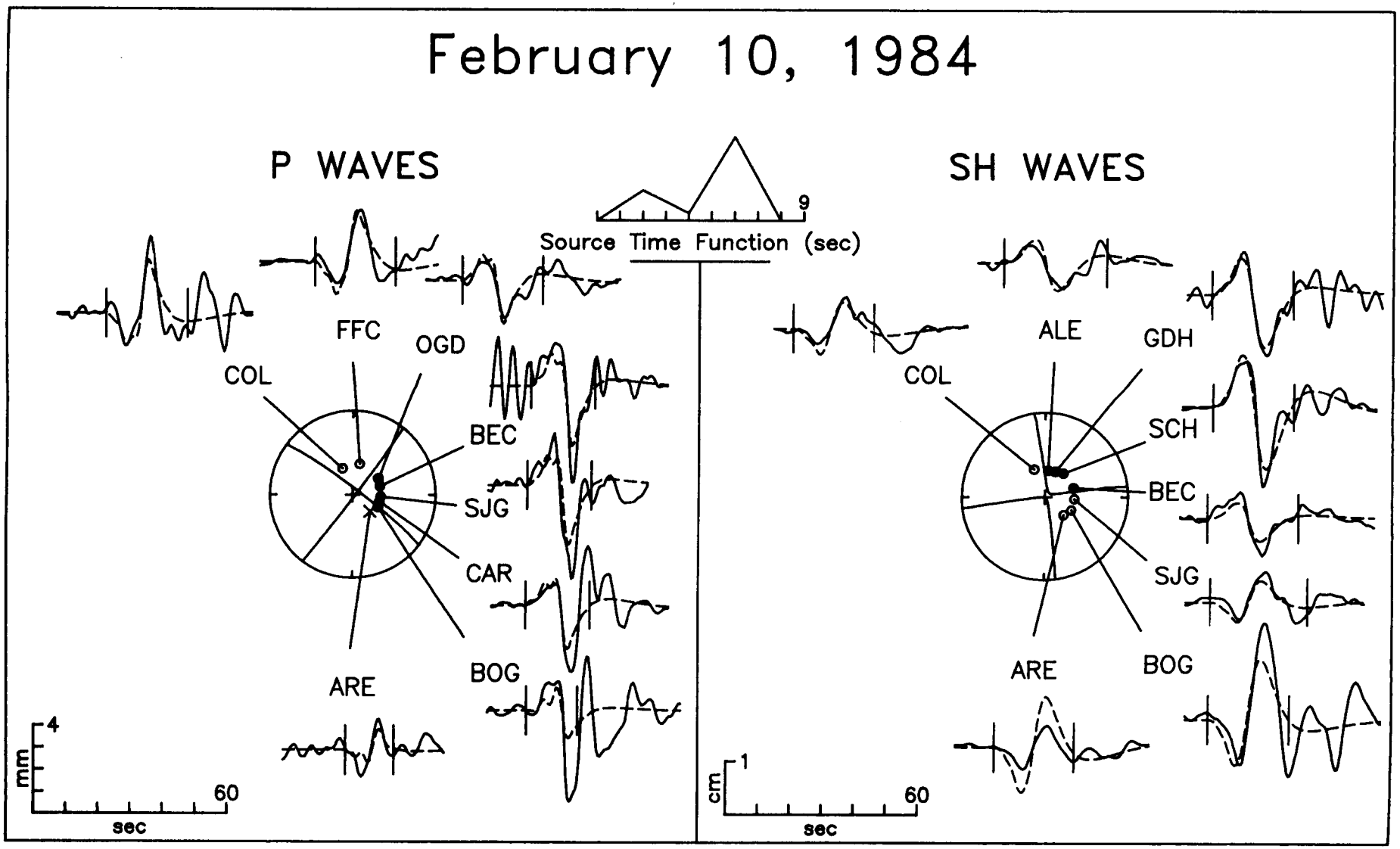
February 10, 1984
P WAVES
SH WAVES
9
Source Time Function (sec)
FFC
OGD
COL
BEC
SJG
CAR
ARE
BOG
ALE
GDH
SCH
4
mm
60
sec
1
cm
60
sec